SPICAM: Spectroscopy for the Investigation of the Characteristics of the Atmosphere of Mars

J.-L. Bertaux[1], O. Korablev[2], D. Fonteyn[3], S. Perrier[1], A. Fedorova[2], F. Montmessin[1], F. Leblanc[1], S. Lebonnois[4], F. Lefèvre[1], E. Quémerais[1], P. Rannou[1], J.Y. Chaufray[1], F. Forget[4], B. Sandel[5], A. Stern[6], C. Muller[3], E. Dimarellis[1], J.P. Dubois[1], S. Guibert[1], G. Souchon[1], M. Leclère[1], F. Semelin[1], A. Reberac[1], M. Barthelemy[1], J.C. Lebrun[1], C. Taulemesse[1], E. Van Ransbeeck[1], B. Gondet[8], A. Kiselev[2], A. Rodin[12], A. Stepanov[2], Yu. Kalinnikov[2], A. Grigoriev[2], A. Hauchecorne[1], M. Cabane[1], E. Chassefière[1], G. Cernogora[1], A.C. Levasseur-Regourd[1], M. De Maziere[3], E. Neefs[3], P.C. Simon[3], D. Fussen[3], D. Nevejans[3], E. Arijs[3], F. Hourdin[4], O. Talagrand[4], O. Witasse[7], E. Kyrölä[9] & J. Tamminen[9]

[1] *Service d'Aéronomie du CNRS/IPSL, BP3, F-91371 Verrières-le-Buisson, France*
Email: jean-loup.bertaux@aerov.jussieu.fr
[2] *Space Research Institute (IKI), 84/32 Profsoyuznaya, 117810 Moscow, Russia*
[3] *Belgian Institute for Space Aeronomy, 3 av. Circulaire, B-1180 Brussels, Belgium*
[4] *Laboratoire de Météorologie Dynamique, 4 place Jussieu, F-75252 Paris Cedex 05, Paris, France*
[5] *Lunar & Planetary Laboratory, 901 Gould Simpson Building, Univ. of Arizona, Tucson, AZ 85721, USA*
[6] *SouthWest Research Institute, 1050 Walnut Avenue, Suite 400, Boulder, CO 80302-5143, USA*
[7] *Research & Scientific Support Department, ESTEC, Postbus 299, 2200 AG Noordwijk, the Netherlands*
[8] *Institut d'Astrophysique Spatiale, Orsay Campus, F-91405 Orsay Cedex, France*
[9] *Finnish Meteorological Institute, PO Box 503 FIN-00101 Helsinki, Finland*

The SPICAM (Spectroscopy for the Investigation of the Characteristics of the Atmosphere of Mars) UV–IR dual spectrometer is dedicated to the study of the atmosphere of Mars. It is the first instrument to perform stellar occultations at Mars; its UV imaging spectrometer was designed primarily for atmospheric vertical profiling by stellar occultation. The IR spectrometer is dedicated to nadir measurements of H_2O abundances simultaneously with UV ozone measurements, for a better understanding of the chemical coupling H_2O–O_3.

The principal SPICAM achievements are: the first vertical profile of density/temperature of CO_2 obtained from a planetary orbiter; numerous vertical profiles of ozone and cloud layers; the systematic measurement of total vertical ozone along-track on the dayside provides the first climatic map of ozone on Mars; the first simultaneous measurements of ozone and water vapour from an orbiter; the discovery of nightglow NO bands in UV; the discovery of auroral activity near the crustal remnant magnetic field; a thorough study of the ionosphere–upper atmosphere through high-altitude aeronomical observations of O, H, CO, CO^+, and CO_2^+; and the first measurement of H_2O and CO_2 ice albedo spectra (simultaneously with OMEGA and PFS). Other products of IR nadir observations are: surface albedo at various wavelengths; the intensity of $O_2(^1\Delta_g)$ emission due to photo-dissociation of ozone; the equivalent widths of carbon dioxide and water ice (on the surface and in aerosol layers); and water vapour total column amount.

All of these successes are the result of a highly versatile instrument, a highly capable spacecraft, and engineers and scientists dedicated to the design, building and testing of the instrument, integration on the spacecraft, and complex operations managed at ESTEC and ESOC.

1. Introduction

Mars Express is recovering most of the science lost with the launch failure in November 1996 of the Russian Mars-96 mission. SPICAM was dedicated to studying the atmosphere of Mars from top to bottom (Bertaux et al., 2000), in a variety of observing modes, including stellar occultations. It consisted of two packages: one for solar occultations, and one for stellar occultations and limb viewing. With the common electronic package, the total mass was 46 kg. Within the much more limited payload mass available on Mars Express, the design had to be radically modified. The strenuous efforts of the team produced a new instrument, called SPICAM Light, a 4.7 kg UV–IR instrument able to deliver most of the science of the Mars-96 version. The considerable mass saving was achieved by sacrificing all the visible part of the spectrum in the solar and stellar occultation sensors, and by removing all redundancy between the two sensors. Also, the pointing ability of Mars Express avoided the need for the instrument platforms of Mars-96. SPICAM Light was originally proposed to include the separate solar occultation IR sensor (SOIR) inherited from the solar package of SPICAM/Mars-96. This 3.8 kg sensor consisted of a grating spectrometer (1.2–4.8 μm, resolution 0.4–1 nm) for vertical profiling during solar occultations of H_2O, CO_2, CO, aerosols and exploration of carbon compounds such as methane (Bertaux et al., 2000). The severe mass constraints precluded its inclusion; instead, an extremely lightweight near-IR spectrometer based on acousto-optical tuneable filter (AOTF) technology, dedicated to water vapour measurements at 1.38 μm, and designed in Russia, was accepted by ESA.

This chapter presents an overview of the instruments, the modes of observations, some statistics on the number of observations, and a summary of the main scientific results. These results are discussed in much greater detail in several dedicated papers: the retrieval of occultation data (Quémerais et al., 2006), total ozone mapping (Perrier et al., 2006), ozone vertical profiling (Lebonnois et al., 2006), dust and aerosol vertical profiles (Montmessin et al., 2006), dayglow and nightglow (Leblanc et al., 2006), limb dust measurements (Rannou et al., 2006), and water vapour measurements (Fedorova et al., 2006). This chapter is based on material presented in Bertaux et al. (2006) and Korablev et al. (2006).

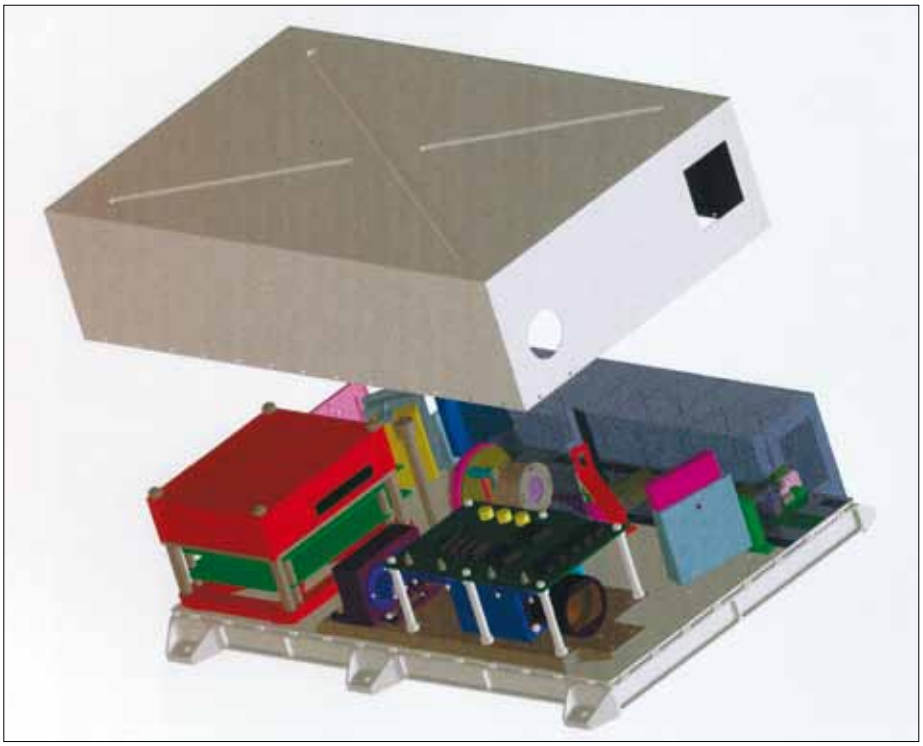

Fig. 1. Mechanical layout of the SUV and SIR channels. The IR AOTF spectrometer is at the front; the UV spectrometer is at the rear. The common optical axis points to the right (the +*Z* axis of the spacecraft).

Table 1. SPICAM mass, power and telemetry budgets.

Mass	Electronics block (DPU)	0.9 kg
	Sensor unit (SU)	3.8 kg
	Total	4.7 kg
Power	DPU + SUV	13 W
	DPU + SUV + SIR	18 W
Data volume		
per measurement	SUV	3.1 kB
	SIR	1.05 kB
per orbit		~5 MB

Table 2. Characteristics of the SPICAM UV channel (SUV).

Primary mirror	Off-axis parabola 40 x 40 mm, coated MgF_2, f = 120 mm
Slit	50 μm × 4.6 mm; 500 μm × 2.2 mm
FOV	of a pixel 0.7 × 0.7′
	2 × 3.16° no slit (stellar occultation); 0.24 × 0.95° with double slit
Spectral range	118–320 nm
Grating	holographic, concave, toroidal coated MgF_2, 290 lines/mm, blazed 170 nm
Spectral resolution per pixel	0.51 nm
Resolving power (occultations)	120–300 stellar; small slit
Resolving power (extended source)	120–300 small slit, ~20 large slit
Pointing accuracy	<0.2°
Detector	CCD Thomson TH7863 TE cooled at 270K, useful 288 x 384 pixels, 23 × 23 μm
Intensifier	Hamamatsu 200M, solar blind CsTe photocathode, input window MgF_2 + sapphire
Vertical resolution	<1 km (occultations), ~10 km (limb)

2. Instrument Overview

SPICAM consists of two blocks: a 3.8 kg sensor unit (SU) with the UV (SUV) and near-IR (SIR) spectrometers, and a simple data processing unit (DPU, 0.9 kg) providing the interface for these two channels with the spacecraft. After the loss of SOIR at selection, both channels acquired a solar occultation sounding capability in partial compensation (with a shorter wavelength range). The instrument's mechanical layout is presented in Fig. 1; the mass, power and telemetry budgets are summarised in Table 1.

3. UV Spectrometer

3.1 UV Spectrometer Description

The SUV's characteristics are summarised in Table 2. For better efficiency in the UV, the spectrometer has only two reflective surfaces (Fig. 2). An off-axis parabolic mirror reflects the light towards the spectrometer entrance. At its focal plane, a mechanical slit system provides two configurations: no slit at all for

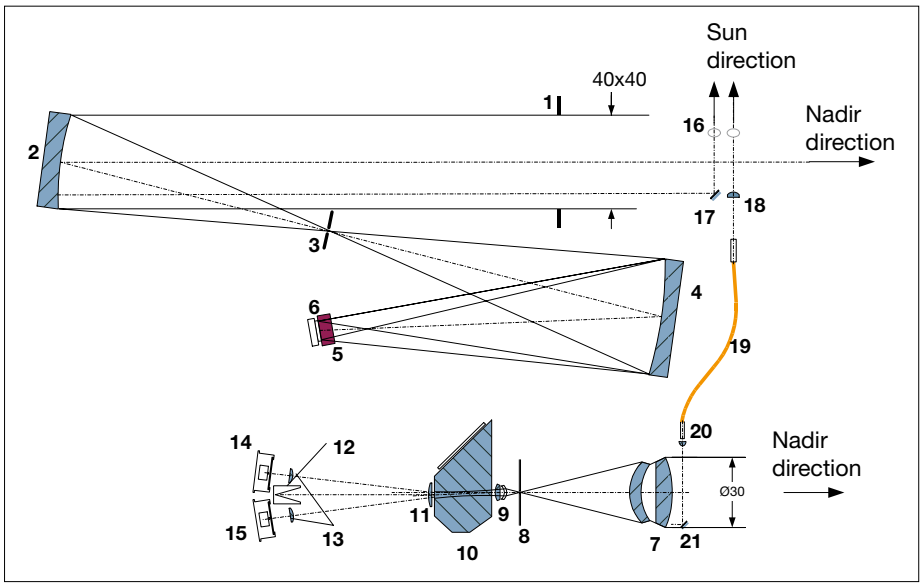

Fig. 2. Optical scheme of SPICAM's UV and IR channels. 1: aperture blend of the UV channel; 2: off-axis parabolic mirror; 3: slit (can be changed from wide to narrow, by a mechanical actuator; see text); 4: concave UV grating; 5: intensifier; 6: CCD; 7: IR channel objective; 8: IR FOV diaphragm; 9/11: collimating lens; 10: AOTF crystal; 12: light trap for undiffracted light; 13: detector proximity lenses; 14: 'extraordinary' beam detector; 15: 'ordinary' beam detector; 16: solar opening (closed by shutter when not looking at Sun); 17/21: flat mirror; 18: IR solar entry; 19: optical fibre; 20: fibre collimator.

stellar occultations, and a slit for extended sources. The slit is divided into two, with different widths providing two spectral resolutions when observing extended sources. The 50 µm-wide slit provides good resolution at lower fluxes; the 500 µm slit offers more sensitivity at the expense of a coarser spectral resolution. The slit can be completely retracted, leaving a hole corresponding to the total useful field of view (FOV; $2 \times 3.16°$). This configuration is used in the stellar occultation mode with a dark limb when the spectrum of the star is recorded on a few lines of the CCD. The required pointing accuracy is 0.2°, but the achieved spacecraft pointing accuracy is often much better on Mars Express, after accounting for a small mechanical misalignment of SPICAM with the craft's axis, which was measured in flight using star observations. It has been possible on some occasions to perform stellar occultations within the narrow part of the slit (0.02° wide), allowing some vertical profiling even on the dayside.

A holographic concave toroidal grating from Jobin–Yvon, ion-etched for efficiency, feeds the detection block. The image ratio is ~1, which means that a monochromatic image in the entrance of the spectrometer is conserved in the detector plane (Fig. 3). The spectral resolution for a point source determined by aberrations is about 1 nm. The CCD detector is a Thomson TH7863 with 288×384 useful pixels, and a masked zone of equivalent size. Pixel size is 23×23 µm. The detector is electrically cooled to ~0°C; at this temperature the dark current equals 800 electrons per pixel per second, or a few analogue to digital units (ADUs) only. By means of custom fibre optics, the CCD is coupled with the output window of the image intensifier (Hamamatsu type 200M). A solar-blind CsTe photocathode has zero quantum efficiency beyond 320 nm. The input window is made of MgF_2 to reach down to Lyman-α wavelengths – an important target for SPICAM. A sapphire filter partially covers the window, preventing overlapping of diffraction orders and Lyman-α stray light.

For solar occultations, there is a 0.2 cm^2 mirror at 90° to the main optical axis at the entrance pupil. During solar occultation measurements, the detector operates at the lowest gain and an integration time of 20 ms. The focal length of the telescope is such that one CCD pixel covers a FOV of $0.01 \times 0.01°$. The narrow part (0.02° wide by 1.9° long) of the spectrometer slit has a spectral resolution of 1.5 nm (about 3 CCD pixels), while the wide part (0.2° wide by 0.98° long) has a higher photometric sensitivity for extended sources (factor ~8), at the expense of a reduced spectral resolution (6 nm). In principle, SPICAM can record 288 spatially resolved spectra along its 2.88°-long

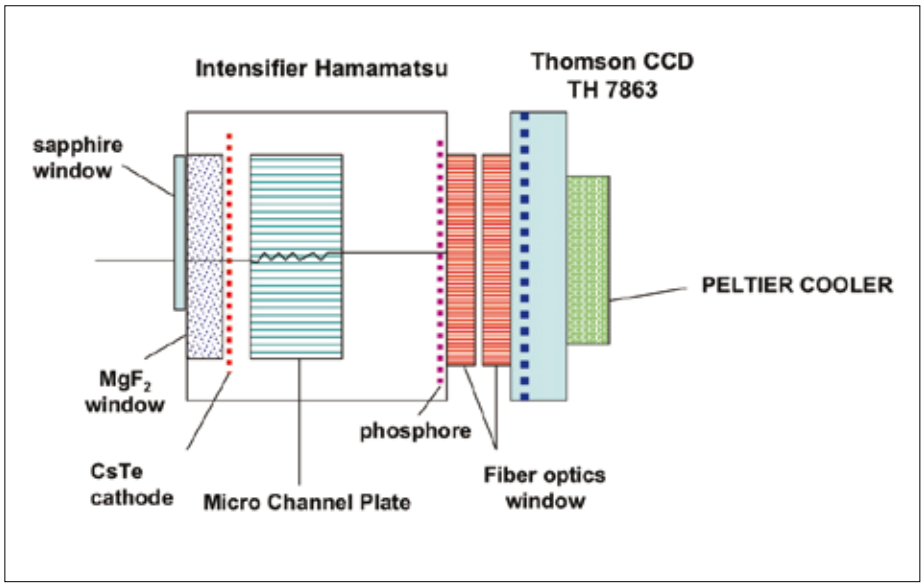

Fig. 3. The SPICAM UV detector combines an image intensifier from Hamamatsu, transforming each UV photon at the entrance into a pulse of green light generated by the phosphor. The image is then conveyed through two blocks of fibre optics, one in the Hamamatsu detector, the other attached to the Thomson CCD. (W. Sandel, Lunar & Planetary Laboratory)

slit (i.e. each spatial element subtends 0.02 × 0.01° on the sky). However, in practice, only five spectra are transmitted for each 1 s measurement in order to save on data transmission. These spectra are formed differently for various modes of CCD readout (see Fig. 6). The most-used mode is such that each of the five spectra is a sum of N individual CCD line spectra (binned on chip in the readout line, before reading), with $N = 2$, 4, 8, 16 or 32, forming five adjacent spatial bins of variable extent (from 0.02° to 0.32°). Two other modes may be used for special purposes: a full imaging mode, when the whole CCD is read, five consecutive lines at each reading, with the first displaced by four lines; and a 'progressive binning' mode that provides a higher dynamic, since 2, 4, 8, 16 and 32 lines are binned together in the five spectra transmitted via telemetry (with the risk of saturation and overspilling of the register). This mode was useful at the beginning to optimise the gain level and integration time for nadir observations.

The gain of the Micro Channel Plate (MCP) of the image intensifier may be adjusted by telecommand with a high-voltage level of 500–900 V, commanded by a digital-level HT of 0–255. When a photoelectron is created in the photocathode (a photo-event), it results in a pulse of light from the phosphor, distributed over a few pixels of the CCD. It is detected by the CCD reading electronics by a number of ADUs. At $HT = 20$ (a typical low gain necessary to avoid saturation for dayside nadir observations), there are about 1.5 ADU created per photo-event; for $HT = 200$, there are ~40 ADU per photo-event. The absolute calibration of the instrument is well characterised by numerous observations of hot UV stars and comparison with previous International Ultraviolet Explorer (IUE) measurements.

There is a potential danger to activating the intensifier at a large gain with an intense source of light. This high gain has to be used cautiously on the dayside at high altitude, and on the nightside. A constraint of SPICAM operations is that the instrument parameters may not be changed during an observing period (ON–OFF). In particular, when a fixed inertial attitude of the spacecraft is chosen, it must be certain that the signal will not damage the detector if a high gain is used on a bright target.

3.2 Instrument Characteristics Measured on the Ground

Figure 4 is an overall view of SPICAM. Figure 5 shows the detector illuminated through the optics by monochromatic light (Hg line emission at 253.7 nm). Some

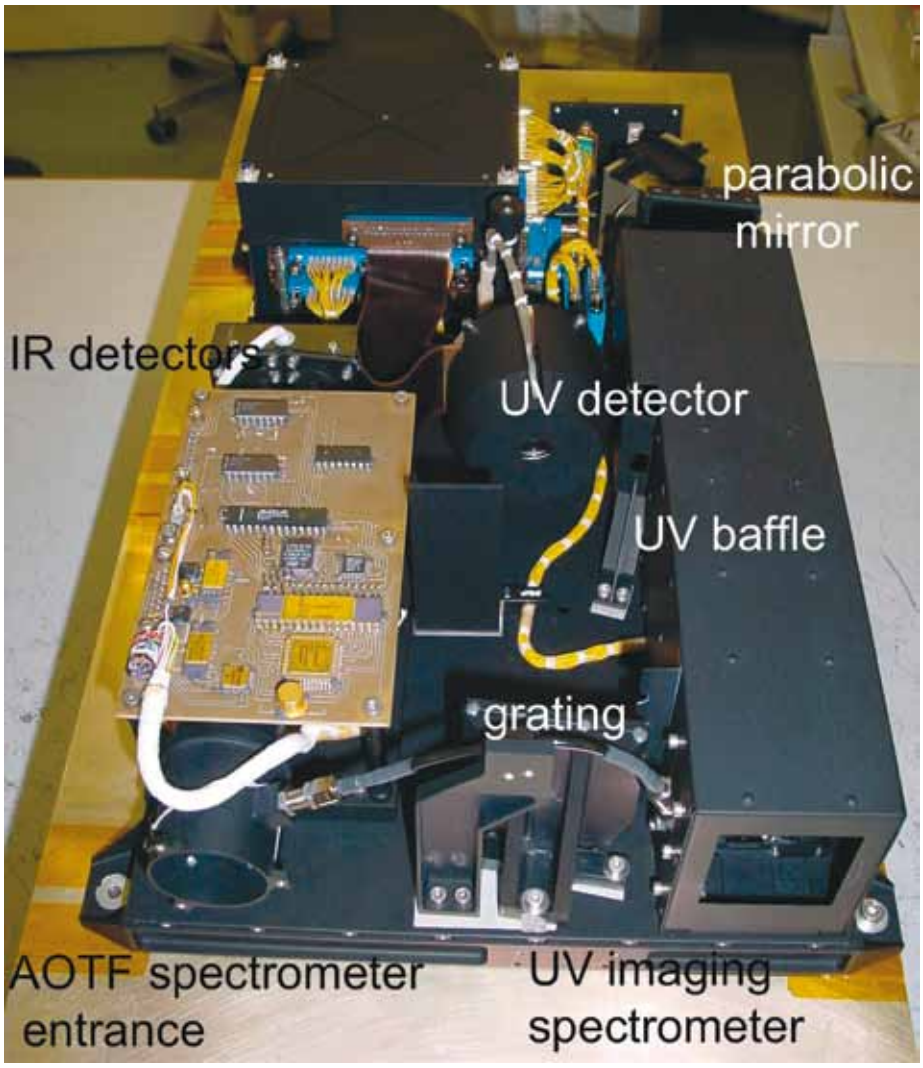

Fig. 4. The SPICAM sensor unit. The entrance of the UV spectrometer baffle (right) is 5×5 cm, while the entrance of the IR spectrometer is to the left, with the entrance lens visible.

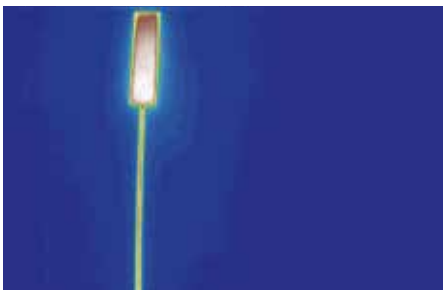

Fig. 5. The detector illuminated by monochromatic Hg line emission at 253.7 nm. The two parts of the slit are evident, one larger than the other. Curvature of the slit is apparent, owing to image deformation by the optics, indicating a slight change in the wavelength calibration for each line of the CCD.

curvature of the slit is apparent, owing to image deformation by the optics. Each line of the CCD must therefore be calibrated in wavelength. The wavelength reflectivity of each component was tested under vacuum before integration in the Flight Model. The detector was calibrated by using the photon-transfer method, which yields the number of ADUs generated in the CCD by a single photoelectron event as a function of the high voltage applied to the MCP.

3.3 SPICAM Observation Modes

3.3.1 Pointing capabilities of Mars Express

Mars Express, a reduced version of the Rosetta spacecraft, was designed with two basic modes of orientation. The antenna can be directed towards Earth for communications, while rotating the solar panels around the *Y*-axis to be perpendicular to the Sun to maximise power. The attitude is therefore constant in inertial space. In the nadir observation mode, the +*Z*-axis (boresighted along the viewing axes of the optical instruments) is maintained towards the centre of Mars. There is no horizon sensor; rather, the orbital position is known in the software and command laws are fed to the inertial wheels. The orbit is eccentric: at insertion it was with a pericentre of 250 km, apocentre 11 559 km and period 7.57 h. It was modified to the G3-b configuration on 3 March 2005: 298 × 10 107 km, 6.72 h.

Table 3. Statistics on SPICAM usage in the various modes of observation.

Mode	*Jan–Dec 2004*	*Jan–Mar 2005*	*Jan 2004 – 4 Apr 2005*
Nadir	318	129	447
Star occultation	421	114	535
Limb observation	43	51	94
Solar occultation	129	156	285
Others	1	10	11
Number of observing orbits	911	450	1361
Number of days of operation	256	92	348
Data volume (gigabit)	24.2	11.5	35.7

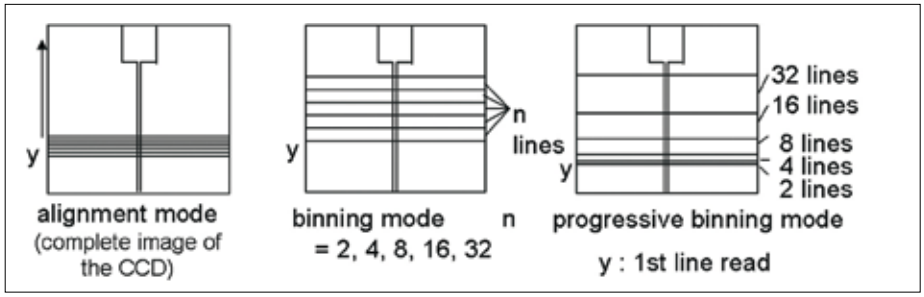

Fig. 6. The various modes of reading the UV CCD.

SPICAM takes advantage of the capabilities of the spacecraft's Attitude and Orientation Control System (AOCS) for its various modes of observation. They are described briefly below; Table 3 highlights statistics about their use during the mission's first 18 months at Mars.

The slew manoeuvre from one orientation to another is typically made at 0.1– 0.5°/s, which requires 20–30 min. In the stellar occultation mode, the +*Z*-axis is oriented towards a star selected from a list of 50 bright in the UV. The orbital motion makes the star disappear behind the limb. In the solar occultation mode, the side port for Sun observations (Fig. 2), which lies in the *XY* plane of the spacecraft, is oriented towards the Sun. The solar occultation occurs when entering eclipse. In the limb mode, the +*Z*-axis has a precalculated orientation so that it scans across the limb. Two variants of this mode were typically used: tangential limb (see below), and limb crossing in the orbital plane. In this latter case, the slit of SPICAM, the CCD scan line of the High Resolution Stereo Camera (HRSC) and the mirror scan of OMEGA may be positioned parallel to the limb. In such an orientation, the whole illuminated planet may be scanned in 30–40 min, a useful mode when the pericentre is not on the Sun side.

The spacecraft's slewing capabilities were also used during observations of Phobos in order to maximise the duration, and during a small number of emission-phase function manoeuvres, when particular geographical areas were observed from various emission angles, to discriminate between ground emission and airborne dust scattering. The geometry of some of these modes is sketched in Fig. 7.

Orientation is a spacecraft resource that has to be shared between all the instruments. Additional spacecraft constraints add to the complexity of establishing a plan of observation: the solar panels are delivering only 70% of their nominal power,

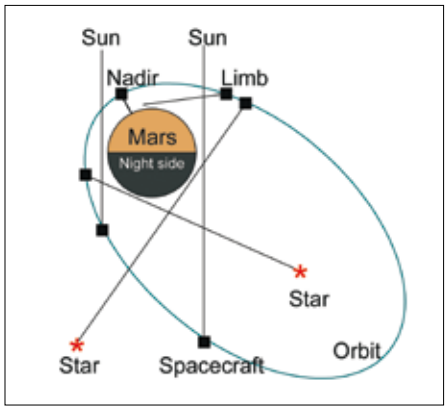

Fig. 7. SPICAM's various modes of observation. The black line indicates the line-of-sight to the target. Apart from the nadir orientation, the spacecraft holds a constant celestial orientation, which allows it to scan across the target (limb) or to observe an occultation of a star or the Sun.

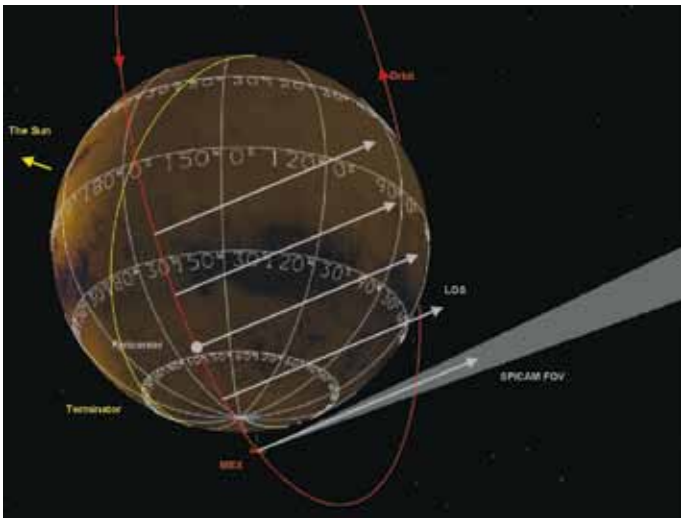

Fig. 8. The geometry of limb-grazing observations, which maximise the time spent observing the limb from an eccentric orbit. It was used successfully on Mars Express, and is also employed by Venus Express. The spacecraft is oriented with the +*Z*-axis (SPICAM line-of-sight) fixed inertially, scanning the limb twice. In this case, the line-of-sight was perpendicular to the velocity vector at pericentre, for optimum vertical resolution at the limb.

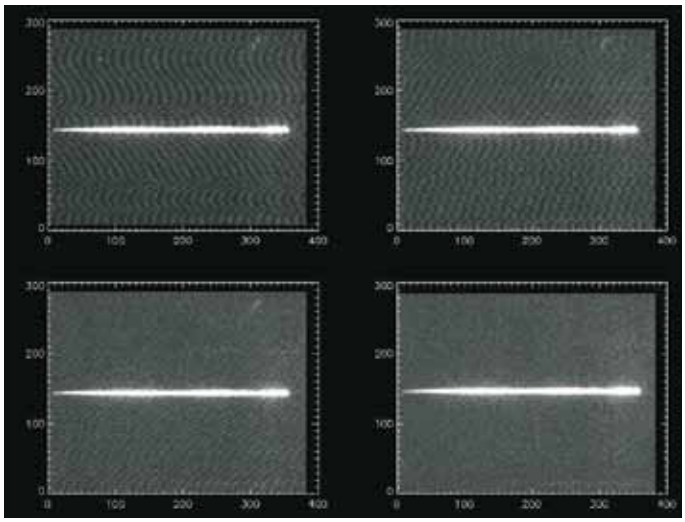

Fig. 9. Distribution of light over the whole detector when a star is observed without the slit. The intensity (in ADUs) is colour-coded. The spectrum is horizontal, along the CCD lines, parallel to the spacecraft *Y*-axis. Optical aberrations spread the spectrum over several lines of the CCD. The slit orientation is parallel to the spacecraft *X*-axis, along the column axis of the CCD (vertically on this figure). The 'tapestry' effect is a residual electronic noise (pseudo-periodic), after subtraction of offset and dark charge.

the radiators cooling some instruments should not be illuminated by the Sun, and a window of 4 h per day is reserved for uplink telecommanding, among others. As a result, the plan adopted 3 months in advance of execution is a compromise between contradictory requirements from the various instruments and the spacecraft, usually resolved during lively animated teleconferences between ESA and the Principal Investigator teams. Table 3 indicates the type and number of observations obtained with SPICAM from orbit insertion (25 December 2003) to 4 April 2005.

3.3.2 Geometry of nightglow/dayglow limb observations: the tangential limb mode

Airglow spectroscopy and radiometry are powerful methods for investigating the upper atmospheres of the terrestrial planets. After the pioneering work by the UV spectrometers of Mariner-6, -7 and -9 (Barth et al., 1971; 1992), this technique was neglected for the following 30 years at Mars, except for rare observations in the EUV with rockets and Earth-orbiting observatories.

While dayglow was clearly measured and identified in the Mariner observations, the first detection of nightglow in the atmosphere of Mars was made with SPICAM (Bertaux et al., 2005a). This was the result of SPICAM's high sensitivity and the dedicated spacecraft operations to optimise the geometry of limb observations, yielding higher signals than the nominal nadir-looking geometry around pericentre. This geometry is illustrated in Fig. 8.

Planning a limb observation requires finding an inertial direction such that, during the orbital motion, the line-of-sight (LOS) scans across the limb. In order to maximise the duration of the observation, the LOS skims the limb tangentially, with a selectable minimum altitude. For any point M on the eccentric orbit, there are two LOS directions that will skim the limb tangentially, with a specified minimum altitude Z_{min}. They are contained in the two planes tangential to the sphere of radius $R_{Mars} + Z_{min}$, which also contain the tangent to the orbit at M (the velocity vector). One is selected to plan the observation, as well as the point M, according to the desired position of the tangent point at minimum altitude. One particularity of this kind of observation is

that several geometrical parameters of the LOS tangent point vary significantly and simultaneously during the observation: altitude, latitude and solar zenith angle. Given the success of this observation mode on Mars Express to detect weak emissions (two discoveries: NO bands at night, and aurora), it is also used on Venus Express.

3.4 Flight Performance of the UV Spectrometer

3.4.1 Pointing quality

For all SPICAM modes, the quality of the results depends on the pointing quality. The pointing accuracy of Mars Express is usually (but not always) much better than the specified 0.1°. Although in principle they are boresighted, there is some offset between the centre of SPICAM's CCD detector and the +*Z*-axis: 0.17° in one direction (along the wavelength axis, parallel to the spacecraft's *Y*-axis), and <0.01° in the perpendicular direction along the *X*-axis, as determined by star spectra during cruise and outside the atmosphere in the alignment mode, which provides a full image of the CCD (Fig. 9).

For a star observation, the spacecraft is requested to position the inertial direction of the star (α, δ) exactly along the *Z*-axis, or with some offset from the *Z*-axis, along a direction defined by two angles θ, ϕ, in the body axis reference frame. θ is the angle of the projection of this direction on the *X*,*Y* plane of the *X*-axis, and ϕ is the angle of this projection with the direction.

Several offset angles were tried, projecting a test star's spectrum in various places on the detector. Figure 10 shows the recorded spectrum of Sirius (41 times in total) in ADU units, on the same wavelength scale, obtained between orbits 906 and 1410 (spanning about 5 months). It shows the excellent stability of the instrument, with no sign of ageing. The curves are different between ~135 nm and 180 nm. This is the effect of the sapphire window, which protrudes into the middle of this wavelength interval for nominal pointing. The sensitivity is higher outside of the window than through it, because its transmission is <1. There is no abrupt change on the curve at the position of the sapphire edge because a point on the cathode at or around the edge 'sees' the grating over an angle of ~20°, partly through the window and partly outside, providing a continuous response to a continuous spectrum.

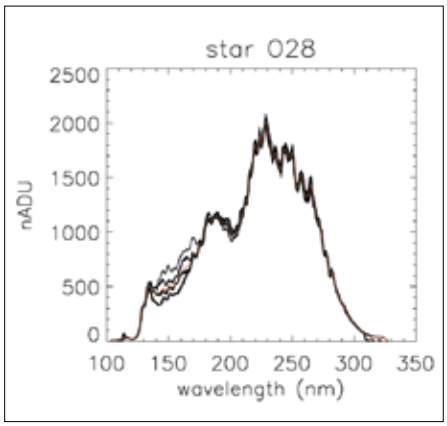

Fig. 10. Forty-one spectra of Sirius (O28 in the SPICAM star catalogue) recorded outside the atmosphere of Mars, between orbits 906 and 1410 (spanning 5 months). They are shown in ADU units, and on the same wavelength scale. The different offset pointings resulted in various positions on the detector. The excellent stability of the instrument is evident, with no sign of ageing. The curves differ between ~135 nm and 180 nm, resulting from the edge of the sapphire window, which is positioned in the middle of this wavelength interval for nominal pointing.

It was recently discovered that the pointing is not perfectly repeatable. With exactly the same offset angles (θ, ϕ) the spectrum of star Zeta Puppis should be at the same place on the detector, but it is not. As shown in Fig. 11, there are two places where it differs by about 0.1°, corresponding to about 6 nm in wavelength shift. At each position, all spectra of one class are precisely superimposed. This problem triggers two difficulties. The first is that the commanded offset pointing cannot be relied upon to establish the wavelength assignment of each pixel of the star spectrum, so the star spectrum recorded outside the atmosphere has to be examined carefully to determine exactly its wavelength assignment (the wavelength of each pixel). The second is that a number of star occultations with the slit in place have failed.

Star occultations are usually made without the slit, because a star is a point source. Some occultations were performed on the dayside with the slit, which partially eliminates the solar light scattered at the limb by dust and the atmosphere. Some were successful: the star signal has about half the strength than without the slit, because of optical aberrations in the off-axis parabolic mirror. Several others failed because of the pointing unrepeatability. This problem may affect other instruments. It comes from startracker A or the redundant startracker B not being perfectly co-aligned.

The pointing stability is quite good. When a star is observed outside of the atmosphere, the signal is usually recorded in five bands of eight CCD lines, the central band collecting >90 % of the total star signal (computed from Fig. 13). The signal in the central band does not show periodic fluctuations (at least before the deployment of MARSIS), which would be a sign of angular oscillations. All slew manoeuvres of the spacecraft (at a maximum 0.5°/s) are followed by a 'tranquilisation' period of about 10 min, before the spacecraft may be considered stable and SPICAM is switched ON. In fact, in order to monitor the spacecraft motions, dedicated observation of a

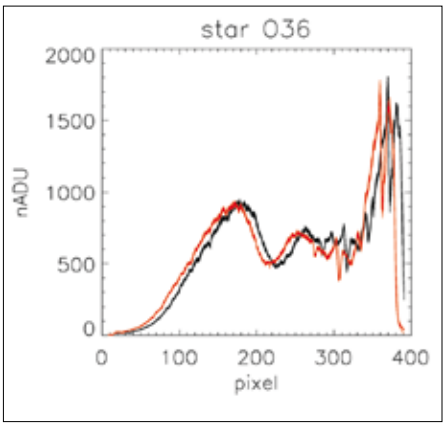

Fig. 11. Thirty-one spectra of star Zeta Puppis (O36 in the SPICAM catalogue) recorded as a function of pixel position. 310 nm is at left, 110 nm is at right (reversed scale). They all fall on only two places. In red, 23 spectra (red curves) fall at the expected position, which is determined by the strong stellar Lyman-α absorption line, centred on the same pixel as the atmospheric martian line observed with the slit. In black, 13 spectra are shifted by about 12 pixels, corresponding to a pointing error of 0.12°, which is linked to the use of redundant startracker B instead of the nominal startracker A.

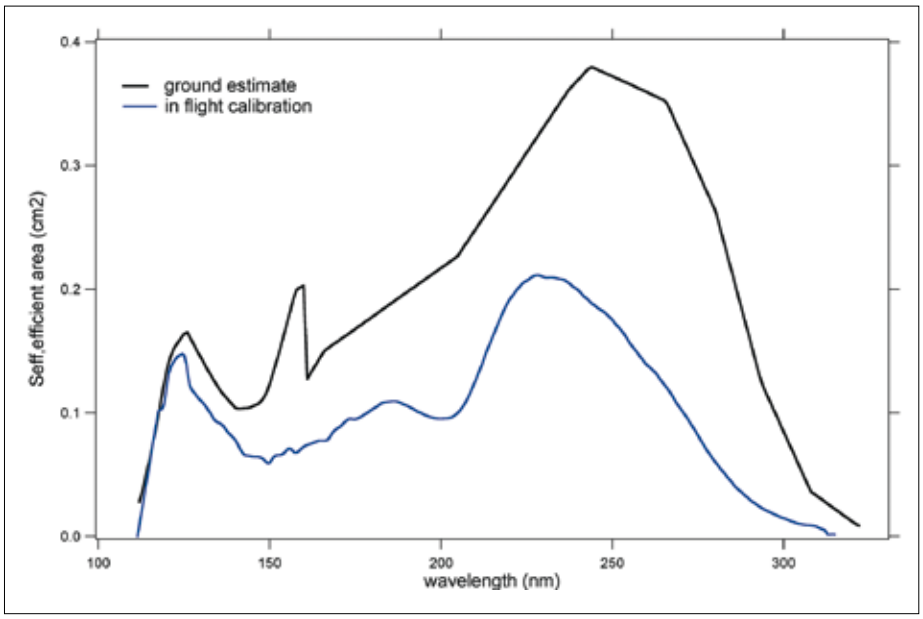

Fig. 12. Sensitivity of SPICAM to a stellar source, expressed in cm². Black curve: estimation from ground calibration of the various optical elements. Blue curve: sensitivity determined by comparison of the measured spectrum (in ADU) of Zeta Puppis with the IUE absolute spectrum of the same star. The gain level used was defined by *HT* = 20, and the gain was determined to be 1.55 ADU per photo-event from an independent statistical analysis of observed fluctuations of the star signal. The long-wavelength decrease is due to the CsTe response, while the short-wavelength decrease is due to the cut-off of the MgF_2 window of the detector. The sharp transition in the black curve near 160 nm takes into account the transmission of the sapphire window, which has a sharp cut-off below 160 nm. The actual curve has a smooth transition, because the photocathode near the mechanical edge is seeing part of the grating through the sapphire window, and another part without the sapphire window.

star should be made, with the slit in place and five bands of two or four lines, and SPICAM switched on even before reaching the star. One could then analyse the signal and determine the oscillations in the two directions, across the slit (the total signal in all bands should fluctuate) and along the slit (the distribution of the signal among the five bands should fluctuate).

3.4.2 Absolute photometric calibration from star observations

The absolute photometric calibration was performed first on the ground. All optical elements were measured separately and the whole instrument was calibrated, but with limited accuracy, because of inherent difficulties in the vacuum UV. Fortunately, stars can be used to obtain a more accurate determination of the sensitivity as a function of wavelength. The measurements obtained by IUE were used as a reference. However, two problems were encountered. Delta Scorpii was used initially but this turned out to be a poor choice because in 2002 it experienced a large brightness surge in the visible, and it is unknown if its UV flux has changed since IUE's measurements. The second problem is that IUE might show variations that are not intrinsic to the star, but rather to the quality of IUE pointing: IUE's FOV was 20 arcsec, and centring was not always perfect. Hubble Space Telescope (HST) calibration in the UV was also performed using IUE spectra, and four stars were indeed SPICAM targets: Zeta Puppis, Beta Cen, Eta Uma and Zeta Oph. SPICAM's absolute calibration is therefore based on this quartet of stars, and IUE data selected by HST investigators are being used (although they differ slightly from the IUE database in some wavelength regions).

Independently, the Lyman-α sky background (extended source) as measured by SWAN on SOHO was compared with HST measurements of 1996 and 2004.

Throughout this period, the ageing of the SWAN sensors was monitored through observations of UV stars (Quémerais et al., 2006). Full consistency was found between the calibration factors found by comparing HST and SWAN measurements of the Lyman-α sky background after 8 years, and the ageing was determined by the SWAN star signal variation during the same period.

The IUE spectrum, given in erg/(cm^2 s Å), is converted to a photon flux Φ (in photons/(cm^2 s nm). SPICAM data are in ADU units, the output of CCD reading. As described above, the high voltage of the image intensifier may be adjusted to increase or reduce the ADUs per photo-event (one photoelectron created at the cathode of the image intensifier, creating a pulse of light in the CCD), a parameter designated as G, the gain of the detector system.

The calibration factor of SPICAM is therefore $G\ S_{\text{eff}}$, where S_{eff} is the 'efficient area' expressed in cm^2, and defined in the relation:

$$N_{\text{photev}} = \Phi\ S_{\text{eff}}$$

where N_{photev} is the number of photo-events detected by SPICAM per second and per nanometre. There is also the relationship:

$$N_{\text{ADU}} = G\ N_{\text{photev}}$$

resulting in the calibration equation:

$$G\ S_{\text{eff}} = \Phi\ /\ N_{\text{ADU}}$$

The gain G was determined on the ground for various levels of the voltage of the image intensifier. It varies from 1.0 to 79 in the whole range of possible commanded voltage levels, defined by the instrument parameter *HT* (from 1 to 255). The gain was also checked in flight by a statistical method, by determining the mean number of photo-events contained in the whole band devoted to the star signal outside of the atmosphere. The total ADU signal fluctuations were analysed, and the gain G determined as:

$$G = \text{Var}\ (S_{\text{ADU}})/\ (2\ S_{\text{ADU}})$$

where S_{ADU} is the mean value of a series of measurements, Var(S_{ADU}) is the variance of the series, and the factor 2 comes from the non-gaussian distribution of the number of electrons coming from a single photo-event (Sandel & Broadfoot, 1986).

Figure 12 shows the sensitivity of SPICAM to a stellar source, S_{eff} (in cm^2), as a function of wavelength. The drop at the short-wavelength cut-off is due to the opacity of the MgF_2 window, while the drop at long wavelength is due to the drop-off of the CsTe cathode (the solar blind behaviour). This curve represents the sensitivity of the instrument for a star source placed at the 'correct' position, defined as the centre of the spectrometer slit. The nominal wavelength assignment is also defined as such, making it valid for all extended source measurements collected with the slit in place. Figure 10 indicates that, when the star is elsewhere, the sensitivity across the detector is similar (at least in the small region explored), except near the edge of the sapphire widow. Also, this curve is valid only when the star signal is integrated over 8 CCD lines (centred on CDD line 144), collecting 90% of the total signal.

When using this S_{eff} curve for the calibration of extended source measurements (filling the whole slit), this 90% factor has to be taken into account (because the whole signal is collected with an extended source), along with the actual FOV of one CCD line: 50 µm (slit width) × 23 µm (CCD pixel size) and the focal length of 120 mm of the parabolic mirror. The solid angle dω subtended by one CCD line is therefore 7.986×10^{-8} sr. In Rayleigh airglow units, 1 R = $10^6 / 4\pi$ photons/(cm^2 s sr), so an extended source with a brightness B of 1 R/nm would give:

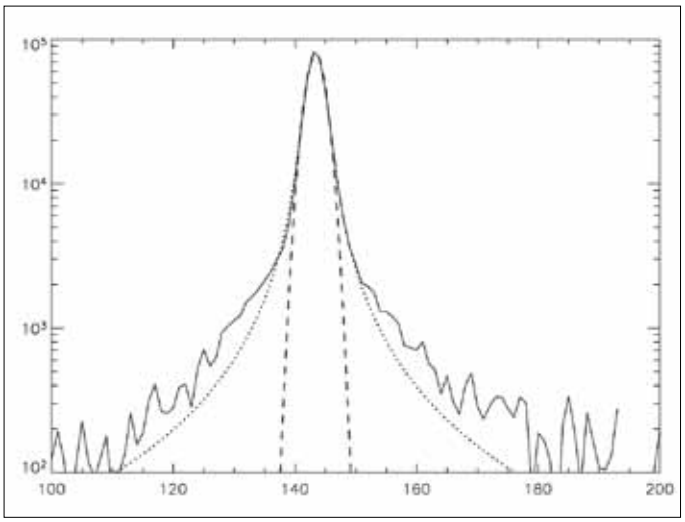

Fig. 13. Solid line: distribution of light along the column axis of the CCD (perpendicular to the dispersion direction) of a stellar image taken in the imaging mode, during the cruise to Mars, displayed in Fig. 9. All wavelengths are summed. The dashed line is a Gaussian fitted to the central part, while the dotted line is a Lorentz profile fitted to the external part.

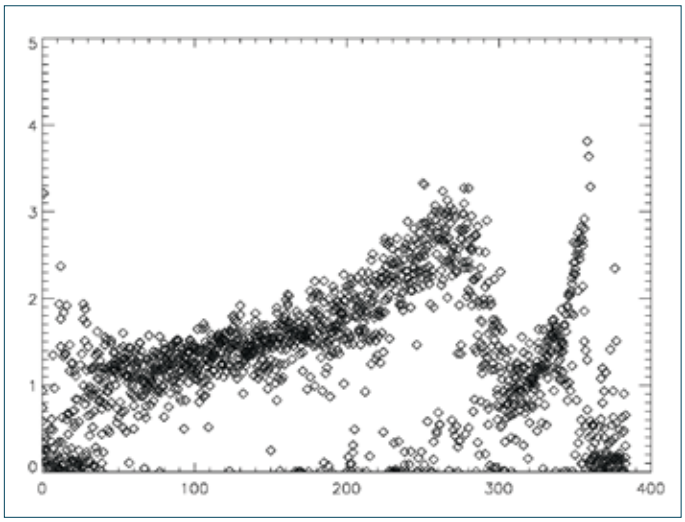

Fig. 14. For each column of the CCD, the vertical width of the stellar spectrum recorded in Fig. 9 is displayed in pixel units as a function of pixel number in the wavelength direction, increasing from right to left. The rapid change around pixel 290 is due to the effect of the sapphire window glued on to the MgF_2 window of the image intensifier, combined with the rapidly changing index of refraction with the wavelength of MgF_2 at short wavelengths. The absence of the window (pixels > 270) improves the focusing for a while. The optical adjustment made on the ground is a compromise to set a good focus over the whole wavelength range. It may be assumed that the spectral resolution also changes accordingly as a function of wavelength.

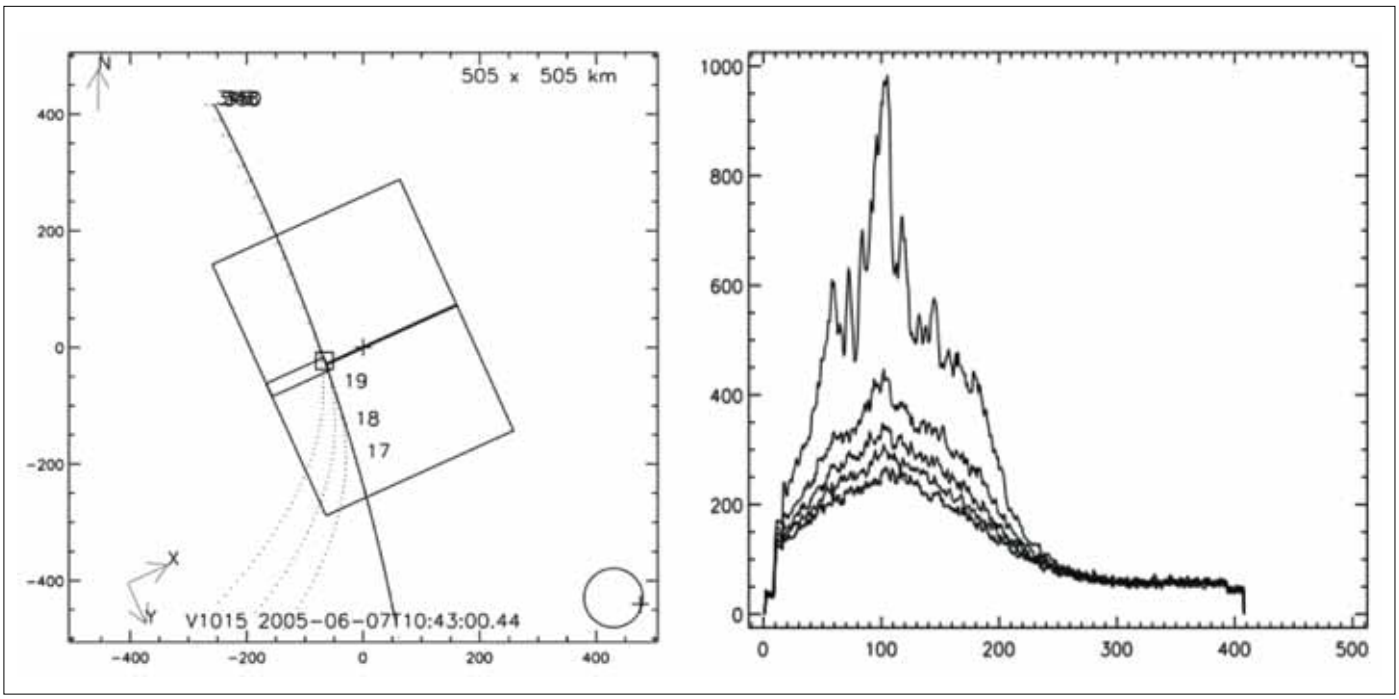

Fig. 15. *Left*: the geometry of the limb observation designed to study stray light. The slit was perpendicular to the limb, with the large part of the slit on the bright part of the limb. *Right*: the spectra recorded at five points of the narrow slit. The nearest point to the limb sees a normal solar spectrum (scattered by dust at the limb) while the others, further away, see only stray light generated through the large portion of the slit.

$$N_{\mathrm{ADUB}} = G\,B\,\mathrm{d}\omega\,S_{\mathrm{eff}} / 0.9 = 1.06 \times 10^{-2}\,S_{\mathrm{eff}}$$

in ADU per second and per nm, for each line of the detector, at gain $G = 1.5$.

When a star is observed without the slit, the light is spread over many CCD lines, with a distribution perpendicular to the dispersion axis (along CCD columns), as shown in Fig. 13. When the usual configuration of five bands of eight CCD lines each is used, the relative content is 1, 3, 90, 5 and 1%, respectively, for bands 1 to 5. This spreading is most likely due to scattering on the surface of the grating, or within the MgF_2 window of the detector. It is a sign of internal stray light, generated after the slit or focal plane of the mirror. Some photons are detected away from their nominal positions, both vertically and in wavelength. Analysis of solar light scattered at the limb (see below) determined the level of stray light, mainly from the large part of the slit, and allowed a systematic correction to be made for it.

On some rare occasions, evidence was found of external stray light, defined as detected photons coming from outside the nominal FOV defined by the slit at the focal plane of the parabolic mirror. This external stray light is still being characterised.

3.4.3 Internal stray light correction

Knowing that the light from a star is spread over a large area (Fig. 13), it was suspected that, when the whole slit is illuminated, the light entering the slit at places other than the lines of the CCD readout will spread over the whole CCD. In particular, a large contribution from the wide part of the slit might be expected.

This problem was resolved with the limb observation during orbit 1788 on 7 June 2005 (solar longitude 225.7°, distance to the Sun 1.39 AU); 1181 spectra were recorded in about 20 min. The observation was made with inertial pointing and grazing geometry, with a minimum altitude of 50 km below the limb, so the limb crossing was slow. The measuring lines were binned by four, covering lines 135 to 155, which are all on the narrow part of the slit, near the centre of the CCD (line 144). The distribution of dust-scattered light at the limb can be considered as a knife-edge to a first approximation: very bright below a certain altitude, with a very rapid drop above. The spacecraft was oriented with its *X*-axis (and slit direction) perpendicular to the limb, with the wide slit looking at lower altitudes than the narrow slit (Fig. 15). Scanning the whole limb up to 200 km (duration 200 s from 0 km to 200 km), there were times when only the wide slit was illuminated by the bright limb.

Figure 16 shows the mean light detected on the CCD as a function of time. The signals of the five bands are very similar, with the shift in time corresponding to the shift in altitude at the limb. The limb signal is expected to drop rapidly, but there is still a slow decrease after the initial fast reduction (between 700 s and 900 s after the beginning of the observation); this is suspected to be stray light from the wide slit. Indeed, the spectrum of this emission (Fig. 17) is completely different from the usual nadir or limb spectra (Fig. 20). There are no strong UV features of the solar UV spectrum. The fifth band, nearer the wide slit, detects more light than the first, which is further from the upper part of the CCD, where the wide slit is. This also confirms that, closer to the wide slit, more stray light is collected in the observed bands. This stray light represents around 10% of the signal. A detailed study was performed by Perrier (2005), yielding the contribution of stray light from all parts of the slit to the read bands. Assuming that the whole slit is illuminated by the same spectrum, it is then possible to subtract from each measurement the spectrum of stray light in Fig. 17 scaled by an appropriate factor, depending on the actual intensity recorded. This was done for the correction of the nadir data for the extraction of ozone content. When the scenery is not uniform over the slit FOV on the ground at a scale of a few km (as over the polar caps), the correction for stray light will not be so accurate.

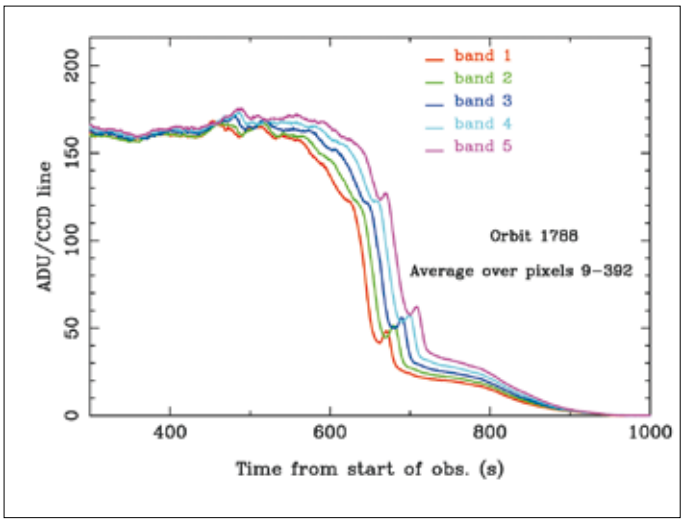

Fig. 16. Light detected when the LOS crossed the bright limb on orbit 1788. The observation was made with inertial pointing and limb-grazing geometry, starting below the limb and ending with a limb-crossing configuration. The measuring lines were binned by four, covering lines 135 to 155, which are all on the narrow part of the slit, near the centre of the CCD (line 144). The integration time (per spectrum) was 320 ms; *HT* = 1 (hence total gain of 1.005). All curves are alike, with a time shift corresponding to the difference of angle/observed altitude at the limb. There is evidence of a detached layer at time 700 for band 3. The signal is expected decrease rapidly above the limb, but there is a signal for a long time. This is interpreted as internal stray light entering the spectrometer through mainly the wide part of the slit and scattered everywhere. The spectrum observed (Fig. 17) does not have the standard shape of the solar spectrum (Fig. 20).

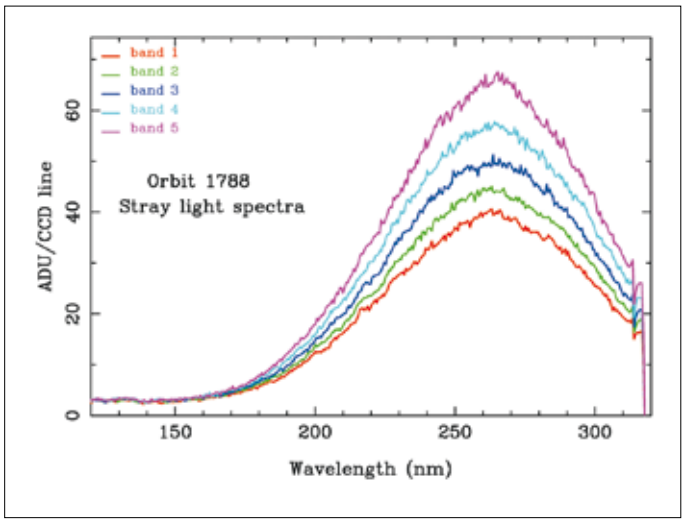

Fig. 17. For each band, the spectrum displayed was averaged from *t* = 750–800 s (Fig. 16). With the associated geometry file, it is known that the five bands are observing between altitudes of 80 km and 200 km, where the limb is normally very dark. At the same time, the wide slit is still illuminated by altitudes below the limb upper limit. The spectral shape exhibits no solar spectrum features (see Fig. 20). For these two reasons, it is believed that the observed signal is internal stray light from the wide part of the slit. 'Internal' signifies photons that have gone through the slit, from the corresponding FOV, but are detected away from their nominal positions (in both the spectral and vertical directions).

4. Nadir UV Observations

4.1 Measurement of UV Surface Albedo of Olympus Mons

The summit of Olympus Mons is the highest point of the planet, with therefore the least atmosphere and dust content. Observations there were used to build a reference spectrum, containing the solar flux, the sensitivity curve of SPICAM, and the albedo of the martian terrain. Other spectra are divided by this reference spectrum, a classical method in spectroscopy, to concentrate on the variations of the spectra from one site to another.

When looking to the nadir, the measured light in the UV is a sum of several contributions:

– solar light scattered by the atmosphere (Rayleigh scattering) and dust/aerosols;
– solar light scattered by the ground.

For both sources, photons can be identified that have been scattered once by the ground and once by the atmosphere, and in which order, before emerging from the top of the atmosphere. In the UV, where the ground albedo is weak according to HST and Phobos-2 (Wuttke et al., 1997), it is not obvious how to predict *a priori* if an increase in dust and gas above the ground will raise or lower the emerging quantity of light. The increase in gas will increase the Rayleigh scattering and decrease the radiation reaching the surface and backscattered upward, but the increase in dust might increase or decrease the light, depending on the quantity of dust and the single-particle albedo. Data collected across Olympus Mons, which offers a wide range of altitudes and atmosphere/dust quantities, provides a good opportunity to determine this. Figure 18 shows the raw data for the five bands on orbit 1437 across Olympus Mons. Figure 19 shows the intensity in ADU/CCD line as a function of latitude (the ground track is

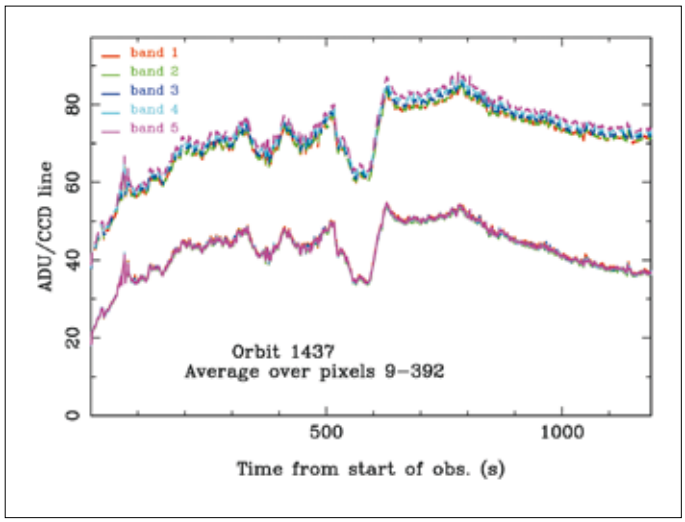

Fig. 18. The upper curves are raw data for the five bands of orbit 1437 across Olympus Mons (intensities integrated over the whole spectrum, dashed lines). The solid lines are after subtraction of offset, dark charge and internal stray light. After the correction, the five bands have exactly the same intensity.

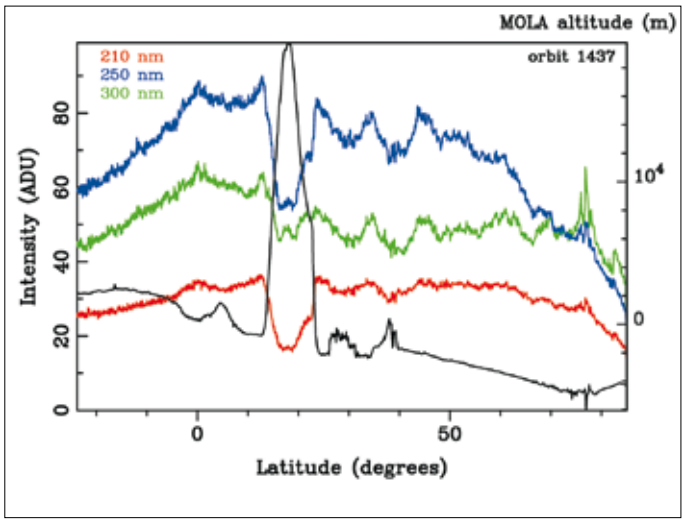

Fig. 19. Intensity measured by SUV (in ADU/CCD line) as a function of latitude during orbit 1437 over Olympus Mons at three wavelengths: 210, 250, 300 nm. The MGS/MOLA altitude of the ground observed at nadir is included in black (right scale). The signal falls at all wavelengths with increasing altitude on the flanks of Olympus Mons, but the relative decrease is larger at shorter wavelength. This is explained by more Rayleigh scattering at low altitudes (an effect clearly seen from aircraft on Earth: the ground looks blueish, except over high mountains).

climbing northward) for three different wavelengths: 210, 250 and 300 nm. Ground altitude is plotted in black, showing the strong relief of Olympus Mons around 17°N. There is a strong drop in intensity when the ground point is higher, stronger at 210 nm than at 250 nm and then at 300 nm, which is consistent with a reduction in Rayleigh scattering with higher altitude.

Figure 20 shows examples of spectra from the same orbit. The shapes reflect the solar flux scattered by the ground and atmosphere/dust, multiplied by the detector sensitivity and affected by the instrumental spectral resolution (both wavelength-dependent). Strong solar features structure the observed spectrum. The recorded intensity decreases below 220 nm and above 290 nm, so only the 220–290 nm range was kept in order to retrieve ozone quantities.

One way to derive the surface albedo is to study large topographic variations, providing large variations in surface pressure. This occurs above Olympus Mons: the surface pressure at the summit is ~1 mbar, while it is ~6 mbar at the base. Data were averaged from the five bands and within a range of ~5 nm around the selected wavelength, in order to increase the signal-to-noise ratio. From the absolute calibration of the instrument (Fig. 12), the measured radiance factor was derived and plotted in Fig. 21 as a function of the surface pressure predicted by the GCM of Forget et al. (1999). Data show a linear behaviour, which can be extrapolated down to zero surface pressure. The value obtained corresponds to the radiance factor if there were no atmosphere. In other words, it is the surface albedo, multiplied by the cosine of the solar zenith angle (SZA). The same method was applied to each wavelength, yielding the surface albedo of Olympus Mons as a function of wavelength (Fig. 22).

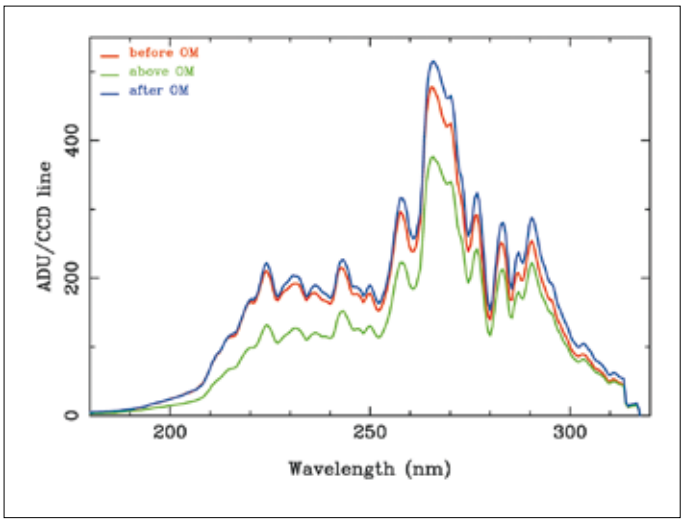

Fig. 20. Examples of SPICAM-recorded spectra, in ADU. The shapes are dictated by solar features, detector sensitivity and instrument resolution. The spectra were averaged over the five bands and 20 s, i.e. 100 spectra averaged, and collected over Olympus Mons (OM). The spectrum at the summit (in green) is less intense and less violet than those from lower altitudes, before and after Olympus Mons; there is more Rayleigh scattering at lower latitudes.

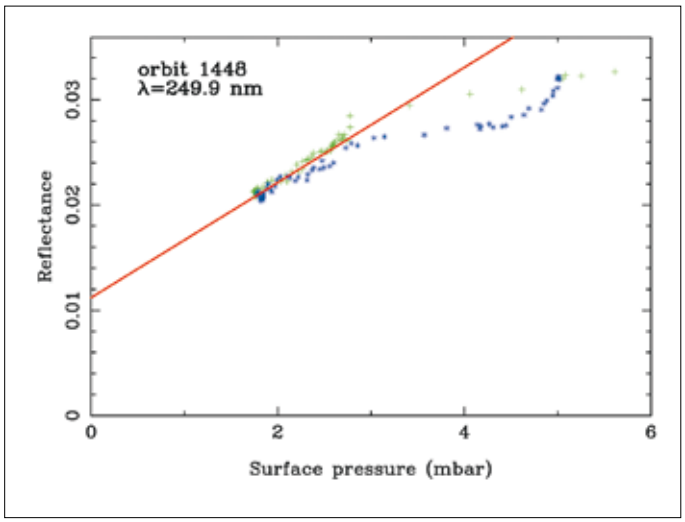

Fig. 21. Radiance factor above Olympus Mons as a function of surface pressure (predicted by a GCM), at λ = 250 nm. The linear fit is plotted in red, which yields the radiance factor from the surface only when extrapolated to zero pressure. When divided by cos(SZA), it gives the surface albedo. The green points are northward of the summit; blue points southward.

In the radiative transfer modelling (see below), it was assumed that the surface albedo varyied linearly with wavelength, defined by its two values at 210 nm and 300 nm. For consistency, a linear fit to the observed albedo of Olympus Mons was obtained in the range 220–280 nm, where it is linear.

4.2 Ozone Retrieval Methodology

The ozone absorption cross-section reaches maximum around 250 nm, showing a broad band with a characteristic shape. This absorption is imprinted in the solar UV radiation backscattered by the surface, the gas and atmospheric dust. The highly structured shape of the solar spectrum (Fig. 20) means that it is not easy to evaluate visually the quality of a fit of the recorded data by a model of what should be seen by SPICAM. Rather, the ratio of two recorded spectra will display much more clearly the absorption of ozone if their ozone contents are different. Therefore, all SPICAM nadir UV spectra have been divided by a data reference spectrum to yield an ensemble of relative spectra, to be fitted by a model. This method was also used by Barth et al. (1973) for ozone retrieval from the Mariner-9 UV spectrometer. The advantage of this 'relative' method is that it avoids the issue of the exact absolute calibration efficient area S_{eff} and the gain G of the detector. Moreover, a simulated solar spectrum at the exact spectral resolution (variable with wavelength) of the instrument is not required in this method. Such a method thus prevents the results from being affected by instrumental calibrations and instrumental parameter uncertainties.

A data reference spectrum is first established, corresponding to an ozone-free atmosphere, with a minimal amount of dust and aerosols. These conditions are naturally realised above the highest mountain, Olympus Mons. The reference spectrum was defined as the average of spectra recorded above Olympus Mons during orbit 1448, near the top of the volcano (mean surface pressure P_0 = 1.9 mbar); it is shown in green in Fig. 20. It is assumed that this reference spectrum is unaffected by ozone (as confirmed by GCM predictions) and dust (dust is minor at this altitude).

Taking the example of orbit 231, all recorded spectra were first divided by the data reference spectrum, and then averaged over the five bands and 50 s to obtain 35

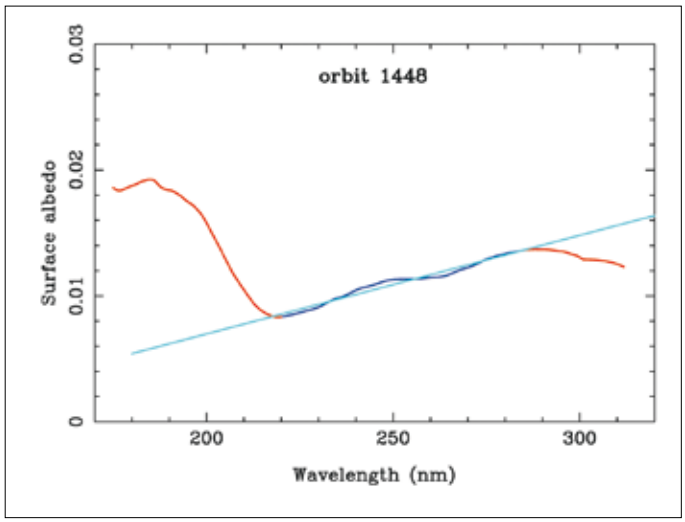

Fig. 22. The surface albedo (red) as a function of wavelength derived by extrapolation to zero altitude (Fig. 21) and division by cos(SZA). The exact value depends on the calibration curve of the instrument. Blue gives a linear fit of the albedo in the range 210–290 nm.

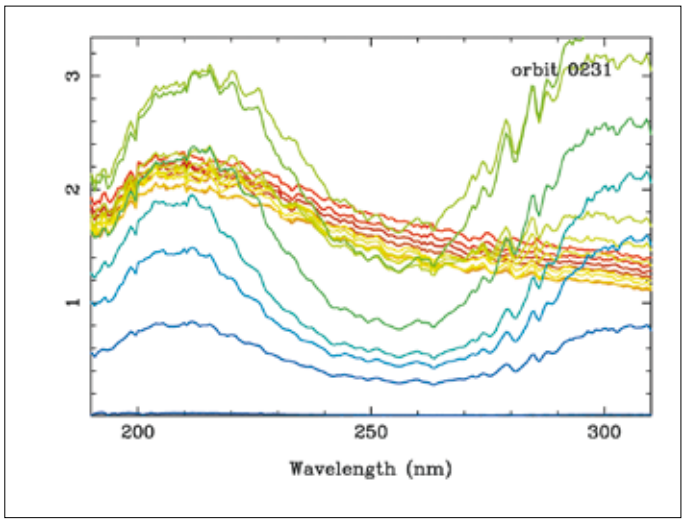

Fig. 23. Examples of relative spectra: spectra from orbit 231 divided by the reference spectrum above Olympus Mons. The colour code varies with SZA, from red for low SZA to blue for high SZA. The large trough centred at 255 nm is due to ozone absorption. During this observation, the spacecraft was looking from low latitudes of the northern hemisphere to high latitudes: as the SZA increases, the observed latitude increases. The trough depth of the ozone absorption band at 250 nm and the corresponding ozone quantity increases when going north. The fine-scale wavelength structure is not due to atmospheric components (the Hartley band of ozone absorption is broad and featureless at the resolution of the instrument) but to an instrumental effect (shift of wavelength scale) that was not not fully corrected.

averaged relative spectra (a typical number for a standard orbit). Every other averaged relative spectrum is plotted in Fig. 23. The colour code varies with the SZA (red for a low SZA, blue for a high SZA). During this observation, the spacecraft was looking from low to high latitudes of the northern hemisphere, and the SZA was increasing with latitude. The further north Mars Express was, the more ozone absorption band at 250 nm appears in the data. The season was early spring ($L_s = 8.6°$); for the last spectra, the SZA is closer to 90° and the signal becomes rather low.

4.3 Radiative Transfer Model and Fitting Method

To model UV spectra observed by SPICAM, a full radiative transfer code based on the Spherical Harmonic Discrete Ordinate Method (SHDOM) in a plane-parallel atmosphere and adapted to the atmosphere of Mars (Perrier et al., 2006) was built to simulate multiple scattering. The model was run once to simulate the data reference spectrum (DRS) over Olympus Mons, and to establish a model reference spectrum (MRS). Then, for each relative data spectrum to be fitted, the model was run for a variety of unknown parameters. The resulting simulated spectrum was divided by the MRS, to be compared with the relative data spectrum, as in Fig. 23.

The atmosphere is modelled over 0–100 km by 51 layers 2 km thick. The exact geometry corresponding to each spectrum (SZA, phase angle, emission angle between local vertical and SPICAM) was taken into account. The surface pressure was taken from the GCM by Forget et al. (1999), and the density of the atmosphere at the altitude of each layer was deduced from the hydrostatic equilibrium. The ground albedo is described by two parameters: its values at 210 nm and 300 nm, and a linear behaviour is assumed in the 210–300 nm range. The values at 210 nm and 300 nm were taken from the linear fit (Fig. 22) over the range 220–280 nm.

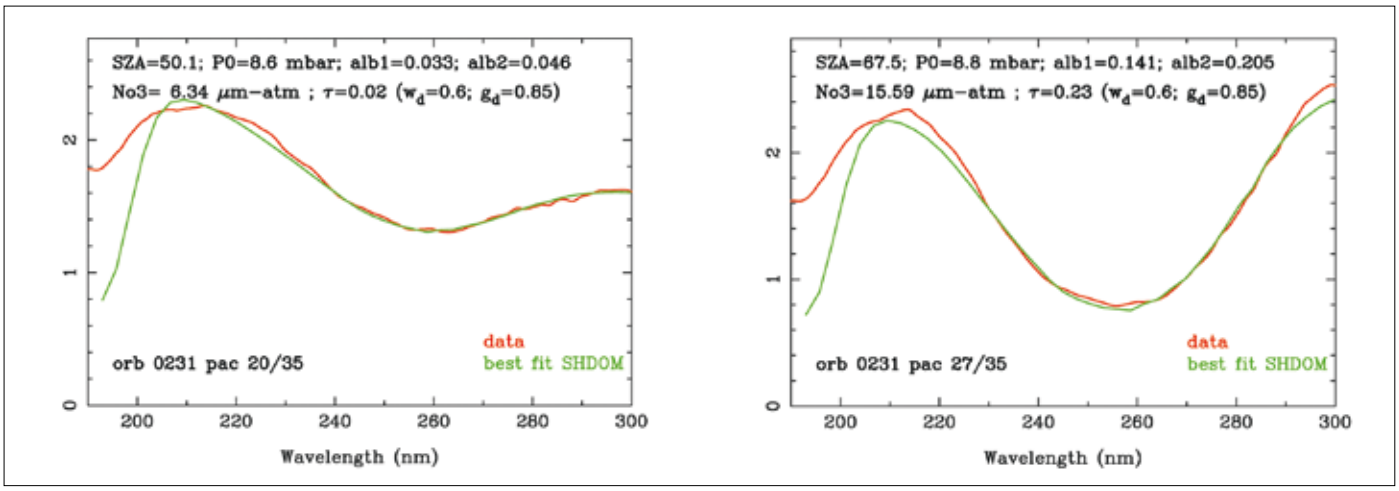

Fig. 24. Two examples of fits for orbit 231, at 54°N (left) and 71°N (right). The data are in red and the best fit in green. At 54°N, the retrieved ozone column is 6.3 µm-atm, whereas at 71°N it is 15.6 µm-atm, showing a large increase in ozone with latitude at northern early spring (L_s = 8.6 for orbit 231).

The phase function of scattering for the ground was assumed to be lambertian. Rayleigh scattering and extinction of all gases were taken into account, as well as pure absorption by CO_2. Ozone was represented by a single free parameter in the model, its integrated column density, while its relative vertical distribution was assumed to be that predicted by the 3D model of Lefèvre et al. (2004).

Dust scattering in the atmosphere is described by the Henyey–Greenstein phase function, with a single scattering albedo $\omega = 0.6$ and an asymmetry parameter $g = 0.85$, independent of wavelength. As for its vertical distribution, dust was assumed to be uniformly mixed with the gas of the atmosphere. There is only one free parameter related to dust: the total vertical opacity calculated at 6.1 mbar. There is no scaling parameter free in this fitting process. The study did not account for the possible presence of clouds.

For each data-relative spectrum, relative data were smoothed over 10 pixels, fitting was restricted to the range 220–290 nm, and only one pixel out of five was fitted, letting 25 independent wavelengths points be fitted. The space of the four free parameters was searched for a best fit using the Levenberg–Marquardt algorithm fitting method. The four free parameters were: ground albedo at 210 nm, ground albedo at 300 nm, ozone column density and dust opacity (both integrated vertically). In this study, the error bars on the data were assumed to be equal at each wavelength, justified because the signal (in ADU) spanned a factor of only 2.5 in the wavelength range considered.

Figure 24 shows, for orbit 231, that the fit is remarkably good in the wavelength range retained. Below 210 nm, the true absorption by CO_2 is clearly present in the model and data (though to a lesser extent in the data).

All the data-relative spectra are completely independent of the absolute calibration of the instrument, in a fashion similar to the technique of solar/stellar occultation. However, in the model, the relative spectra depend somewhat on the choice of the ground albedo for the MRS, which was determined from the absolute calibration of the instrument. This is because the radiance factor is a nonlinear combination of surface and atmosphere contributions. Changing the surface albedo in the MRS will have little effect on the retrieved ozone value, but the albedos of other points on Mars would change nonlinearly.

4.4 First Ozone Map

For each orbit, the best fit was computed of the observed spectrum with the model described above and the Levenberg–Marquardt fitting method, with four free parameters. Then, for each observed area of the atmosphere, the quantity of ozone

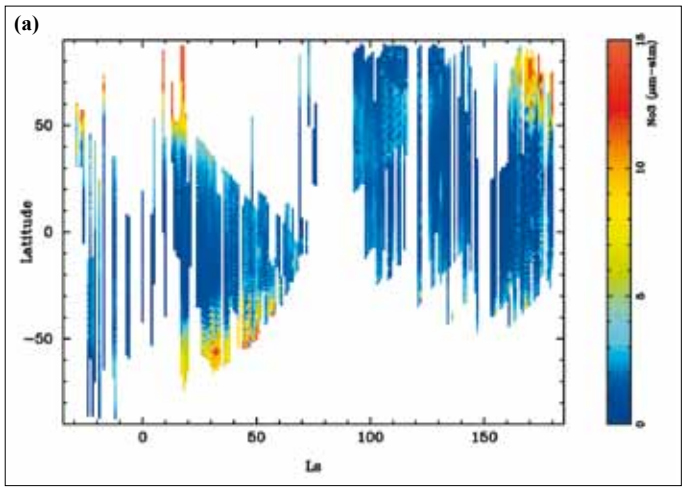

Fig. 25. The first L_s–latitude ozone map, from L_s = 330° to 180°. The dataset coverage in season and latitude is variable, depending on observational and technical constraints. Around L_s = 80° the pericentre was on the nightside and nadir dayside observations were very limited. Sharp variations were measured in the ozone column density.

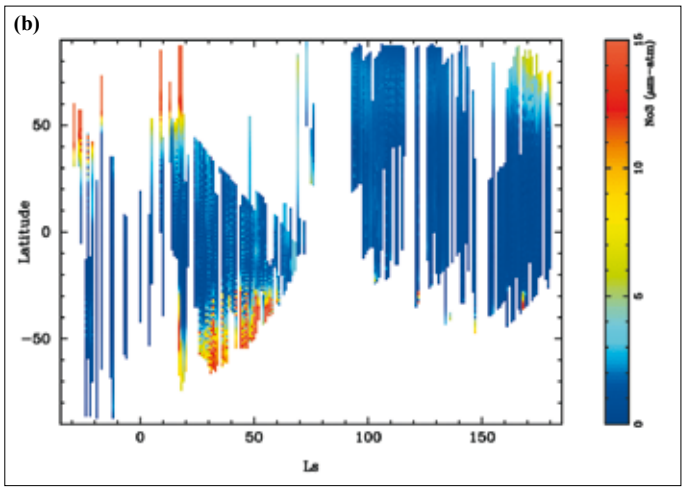

Fig. 26. GCM ozone prediction compared with SPICAM data.

present at the instant of observation was obtained. It is convenient to represent the results in the (geographical) latitude versus solar longitude plane. This plane is divided into sectors of 1 square-degree. When one of these sectors had been observed several times, the average value of the ozone quantity was kept. As far as possible, values were interpolated in unobserved sectors along the latitude axis to complete the dataset. This then produces a map of the ozone quantity as a function of the latitude and the solar longitude. Figure 25 presents the first ozone map ever measured, in units of µm-atm (1 µm-atm = 2.689×10^{15} mol cm^{-2} = 0.1 Dobson units). The map covers only the column range (0–15 µm-atm) in order to improve the contrast for low ozone quantities, although in some places SPICAM was able to measure up to 30 µm-atm. Three ozone-rich regions are visible at high latitudes: in the northern late winter–early spring, during the autumn in the southern hemisphere, and at the end of the northern summer. There are also noticeable variations from day to day.

A noticeable point with the ozone map is the distribution of the available data. Few data are available at high latitudes. This is due both to the large solar zenith angle, and to the need to share observing time with other instruments: SPICAM is usually on at the same time as the imagers, around the pericentre, while the high latitudes can only be observed far from pericentre. There is a lack of data within L_s = 70–90° because of power limitations during solar eclipses. For these reasons, the coverage in season and latitude is highly variable.

Sharp variations are evident in the ozone quantity, depending on the latitude and season. There are three main ozone-rich regions visible on the latitude–season map: the high northern latitudes during late winter and early spring; the high southern latitudes during autumn, and the high northern latitudes during summer.

4.5 Comparison of Ozone Data with GCM Predictions

The SPICAM results were compared (Fig. 26) with the 3D distribution of ozone computed by the GCM described by Lefèvre et al. (2004). For each orbit, the O_3 column was extracted from the GCM for the same location and time as the measurements. All of the gross features of the data map were well-captured by the model, including the location of the three large maxima in the latitude–season maps, and the large day-to-day variability.

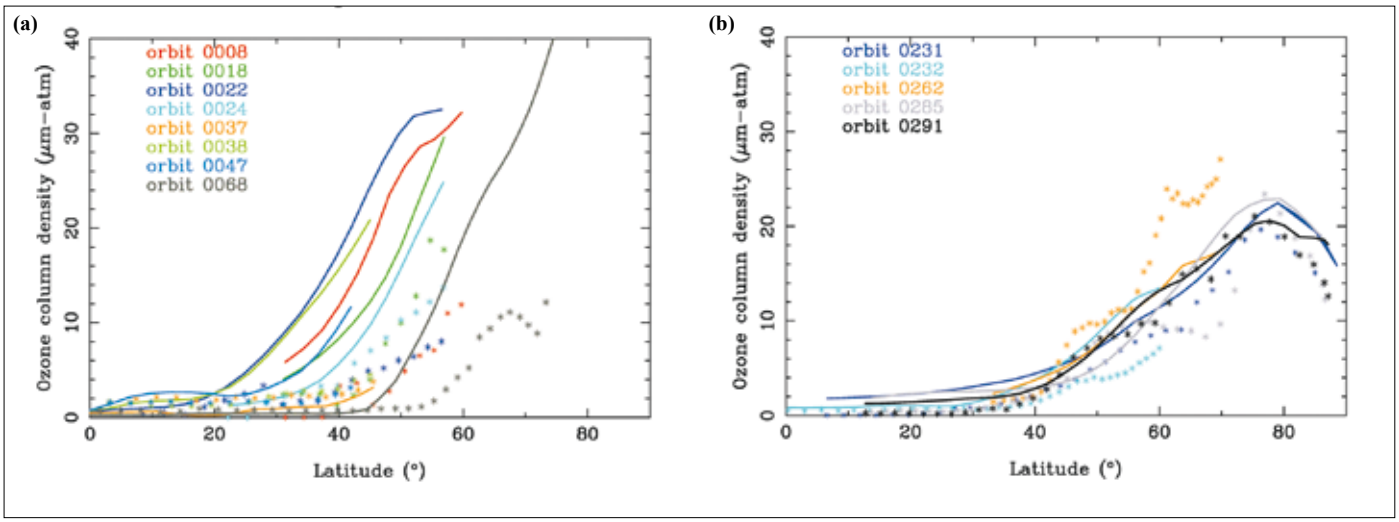

Fig. 27. Detailed comparison of the SPICAM ozone measurements and the GCM calculations for two periods.

Figure 27 compares the SPICAM ozone measurements and the GCM calculations for two periods. In the northern hemisphere in late winter (Fig. 27a, $L_s = 330–360°$), SPICAM observes very low O_3 columns at low and mid-latitudes, and an increase at high latitudes with a large variability and maximum values in the 10–20 µm-atm range. This is qualitatively consistent with the model results, but the predicted quantities are substantially over-estimated at high latitudes, possibly because of an underestimate of water vapour (a scavenger of ozone) in the model. This may indicate that the seasonal decrease in polar ozone from mid- to late winter is not fast enough in the model. Alternatively, an over-estimation of the size of the polar vortex could also explain the increase in ozone that occurs at a latitude too low compared to the observations.

In early spring (Fig. 27b, $L_s = 0–18°$), SPICAM and the model calculations show excellent agreement. The sharp variability of the O_3 column measured by SPICAM is similar to the model simulation slightly earlier in the season (Fig. 27b). The increase in ozone observed above 40°N is now well in line with the GCM prediction.

However, in orbit 262 there is more observed ozone than predicted in the model, and this effect was also seen in many other orbits (not shown here). This discrepancy has been eliminated by considering, in the chemical scheme, an additional reaction, the rate of which has been measured in the laboratory.

It is the reaction of H_2O_2 (and other HO_x radicals) on water ice grains that tends to destroy H_2O_2 (Lefèvre et al., 2008). Since H_2O_2 is a major scavenger of ozone molecules, fewer H_2O_2/HO_x molecules will induce a higher concentration of ozone. This is the first time that a heterogeneous reaction has demonstrated an important role in the atmosphere of Mars, similar to some reactions in Earth's atmosphere that explain the Antarctic ozone hole, where polar stratospheric clouds play a major role. This is an interesting illustration of comparative planetology.

4.6 Early South Pole Observations

During the Mars Express mission, observations found the first clear spectral signature of H_2O ice at the south pole (simultaneously with OMEGA; Bibring et al., 2004), and made the first UV albedo measurements of martian water ice. Here we discuss the results obtained over the south residual cap during orbit 30 (18 January 2004). The residual cap is easily identified in Fig. 28 by its higher visible albedo; it does not contain the geographic pole, but is centred at 87.5°S, 320°E. Figure 28 shows the footprints of the fields-of-view of the two spectrometers as Mars Express was nadir-pointing: circular, 1° diameter for SIR, and rectangular, 0.02 × 0.08° for SUV, which projects to 42 km and 0.8 × 3 km, respectively. A UV spectrum was taken

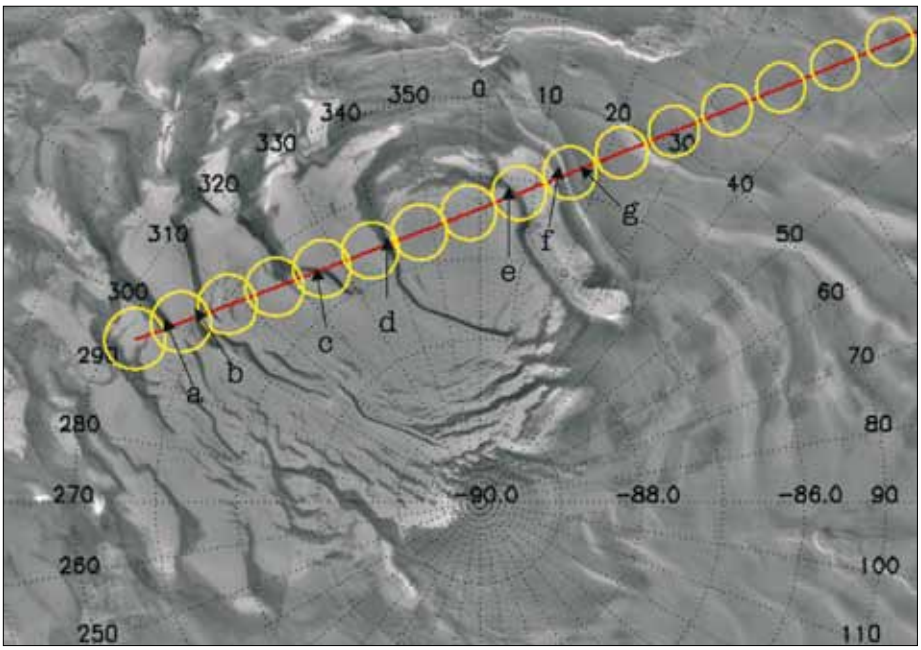

Fig. 28. A Viking map of of the south polar cap. The red line represents the SPICAM UV FOV ground track, and the yellow circles the SIR FOV during the nadir observations of 18 January 2004.

each second, with light integrated for 0.64 s; the FOV moved by about 2 km during this time. A full IR spectrum was acquired in 24 s, but each of the 3984 wavelength samples was acquired during 6 ms, giving a negligible spatial lag: each individual IR sample corresponded to a 1° circle, but since the SIR was sequentially sweeping the wavelengths the FOV was moving accordingly, along the trajectory shown in Fig. 28. The circles are given for the longest wavelength of each IR spectrum. (Also, Fig. 67, a typical SPICAM IR spectrum, clearly shows the water-ice signature).

The martian season of the SPICAM observations corresponds to $L_s = 336°$, late summer for the southern hemisphere: the seasonal CO_2 cap was long gone and the pole was still illuminated by the Sun, which allows analysis of the spectrum of the backscattered solar light. Figure 29 plots the UV reflectance recorded to nadir as a function of acquisition time, showing very strong fluctuations only on the permanent polar cap, with deep troughs corresponding to low-albedo channels apparent in the Viking polar cap image (Fig. 28), identified by the letters a–g in Fig. 29.

Over the permanent cap, the UV reflectance is rather high (0.11), much higher than the 0.02–0.03 recorded beyond the polar cap. However, the high value is still much lower than laboratory measurements of pure H_2O and CO_2 ices (Hapke, 1981), indicating that there is also some dust mixed with the icy material, as might be expected from the ubiquitous dusty character of the martian atmosphere.

Beyond the cap (from around 210 s to 500 s after the start of observation; Fig. 29), the reflectances at 230 nm and 270 nm are almost the same, which means that ground albedo or dust do not cause strong variations in the spectral reflectance. Over the bright regions, the reflectance increases by a factor of 1.6 between 230 nm to 270 nm. It can be assumed that the dust/atmospheric conditions are the same between bright region 6 and region g just outside the cap: this implies that the strong reflectance variation over 230–270 nm is due to ground ice albedo variations with wavelength. Indeed, laboratory measurements of pure H_2O and CO_2 ices (Hapke, 1981) indicate a decrease in reflectance over 230–270 nm, but unfortunately for both types of ice. The reflectances at both wavelengths are the same in the holes a–f, which means no ice is seen in these regions, either because it is in shadow or because the ground is similar to that beyond the cap, where the ground albedoes are also identical at these two wavelengths.

Further systematic UV studies will extend to the north pole, and to the seasonal caps.

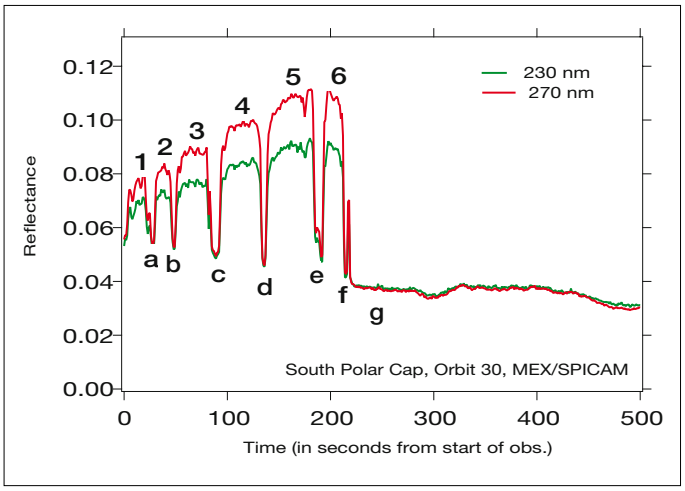

Fig. 29. Nadir UV reflectance at 230 nm and 270 nm along-track over the south polar cap and further north (on the left). The letters a–g indicate regions of low reflectance, in both the SPICAM UV data and in the Viking image of the polar cap. The UV albedo is much higher on the ice lobes (1–6) identified on the Viking images than outside the cap (the region beginning at letter g). While the reflectances at 230 nm and 270 nm are identical outside the cap and between the lobes, it is lower at 230 nm on the lobes, typical of the known signature of ices.

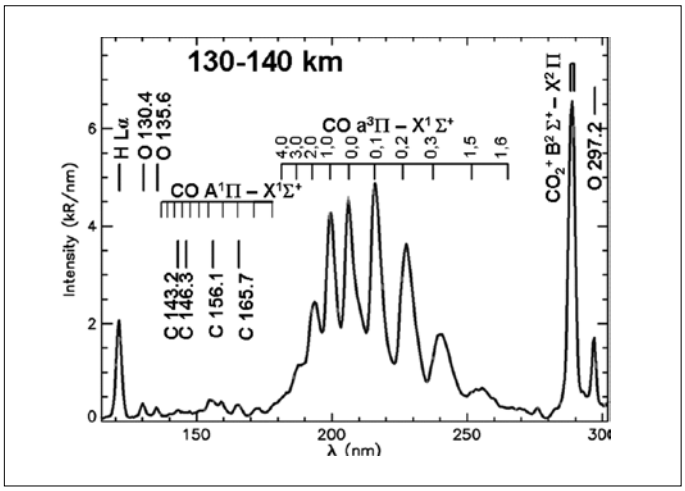

Fig. 30. Spectra obtained by SPICAM UV, at SZA = 14–37°, L_s = 135–171°. 1024 individual spectra measured at altitudes between 130 km and 140 km were averaged.

5. Limb UV Observations

5.1 UV Dayglow

The upper atmosphere/thermosphere/ionosphere (~100–250 km) is an intermediate atmospheric region strongly coupled with the lower atmosphere, and coupled above via the ionosphere with the solar wind (Bougher et al., 2000). Wave coupling of the lower and upper atmospheres is observed to be significant, with diurnal Kelvin waves and semi-diurnal tides providing significant temperature and wind perturbations in the lower thermosphere (Forbes et al., 2002; Bougher et al., 2000; 2001; Wang & Nielsen, 2004, Withers et al., 2004).

Four methods have been used so far to observe the upper atmosphere of Mars. *In situ* observations have been made by descent probes: Mars-6 (Kerzhanovich, 1977), Viking-1 and -2 (Seiff & Kirk, 1977; Nier & McElroy, 1977) and Mars Pathfinder (Schofield et al., 1997; Magalhaes et al., 1999). Accelerometer measurements were made of the total density *vs.* altitude during the aerobraking phases of Mars Global Surveyor and Mars Odyssey between 110 km and 170 km in altitude (Keating et al., 1998; 2003). Remote sensing has been used to explore the upper atmosphere, and radio occultation has provided the electronic profile between 95 km and 200 km in altitude (Bougher et al., 2001; 2004). The fourth method is remotely sensing the airglow emission of the upper atmosphere.

UV is a good spectral range for observing the main martian components: CO_2, CO, O, H and C. From Earth, the Extreme Ultraviolet Explorer (EUVE) observed the He species at 584 Å (Krasnopolsky et al., 1994); the Far Ultraviolet Spectroscopic Explorer (FUSE) at 904–1183 Å detected D, H_2, H, O, N, C, Ar, He, N^+, C^+ and Ar^+, and the bands of N_2 and CO (Krasnopolsky et al., 1998; Krasnopolsky & Feldman, 2001; 2002); and the Hopkins Ultraviolet Telescope at 820–1800 Å (Feldman et al., 2000). Four missions to Mars carried UV spectrometers: Mariner-6, -7 and -9 from 1969 to 1971 (Barth et al., 1971; 1972; Stewart, 1972) and Mars Express. The main objectives of SPICAM UV for Mars' upper atmosphere are to identify the main parameters of the thermosphere and exosphere and to derive some elements of the ionosphere. Figure 30 presents an average of more than 1300 spectra measured in the martian dayglow obtained by SPICAM UV. The spectrum illustrates the main emissions, identified by Mariner-6 and -7, that

Table 4. Dayglow emissions between 1200 Å and 3000 Å.

Line	*λ (nm)*	*Excitation process*[1]	*References*
CO_2^+ $B^2\Sigma^+ - X^2\Pi$	288.3–289.6	PI (CO_2), EI (CO_2)	Barth et al. (1971, 1972), Stewart et al. (1972), Fox & Dalgarno (1979), Witasse (2000)
CO $A^3\Pi - X^1\Sigma^+$	190.0–270.0	RS (CO), EE (CO), ED (CO_2), PD (CO_2), DR (CO_2^+)	Barth et al. (1971, 1972), Stewart et al. (1972), Fox & Dalgarno (1979), Conway (1981), Haider et al. (1992)
CO $A^1\Pi - X^1\Sigma^+$	128.0–280.0	ED (CO_2), PD (CO_2), DR (CO_2^+)	Barth et al. (1971), Gutchek & Zipf (1973), Fox & Dalgarno (1979), Feldman et al. (2000)
C C	156.1 165.7	ED (CO_2), PD (CO_2), RS (C)	Barth et al. (1971, 1972), Fox & Dalgarno (1979), Feldman et al. (2000)
O	297.2	PD (CO_2), ED (CO_2), EE (O), DR (O_2^+)	Barth et al. (1971, 1972), Fox & Dalgarno (1979), Witasse (2000)
O	135.6	ED (CO_2), EE (O)	Barth et al. (1971), Strickland et al. (1972), Fox & Dalgarno (1979), Feldman et al. (2000), Witasse (2000)
O	130.2–130.5–130.6	EE (CO_2 < 200 km), RS (O)	Barth et al. (1971), Strickland et al. (1973), Feldman et al. (2000)
H	121.6	RS (H)	Anderson & Hord (1971), Barth et al. (1971, 1972)

[1] The species in parentheses are the neutral atmospheric species leading to such emissions and excited by either photoionisation excitation (PI), photoelectron impact ionisation excitation (EI), photoelectron impact excitation (EE), photodissociative excitation (PD), resonant scattering and fluorescent scattering (RS), dissociative recombination (DR), photoelectron impact dissociative excitation (ED).

constitute the dayglow between 1200 Å and 3000 Å. The different emissions, their names, sources and spectral ranges are detailed in Table 4. The carbon lines at 1261, 1277, 1432 and 1463 Å are excluded because, although reported in Barth et al. (1971), they are not firmly identified in the SPICAM spectrum.

Figure 30 was obtained using 24 selected orbits with limb scanning of the dayglow emissions. Such an orbit set covers a large range of solar longitude, solar activity, local time and local latitude, and allows reconstruction of the temperature and density profiles for the CO_2 species (Fig. 31a). The temperatures are in good agreement with the thermospheric model of Angelats i Coll et al. (2005). Several probings of the atmosphere above 200 km altitude observed the region's two main constituents: the H and O atomic species. The first can be observed at altitudes of up to 1500 km, whereas the latter is typically detected below 500 km (Fig. 31b).

Figure 31 displays the Cameron band intensity *vs.* altitude measured by SPICAM at low solar activity compared with Mariner-6, -7 (high solar activity) and Mariner-9 (medium solar activity) measurements. The differences in intensity are probably due to calibration over-estimation in the case of Mariner-6 and -7 (Stewart et al., 1972), but also to different solar activity conditions when compared to Mariner-9 in particular. The exospheric temperatures between 150 km and 200 km were retrieved by a simple analysis of the Cameron profile, assuming that within this altitude range the atmosphere can reasonably be considered to be close to a barometric optically thin atmosphere, and that the main process leading to Cameron band emission is photodissociative excitation of its main constituent (CO_2). Such a method was used to analyse Mariner-9 data (Barth et al., 1972). For SPICAM, it yields an exospheric temperature of 228±6K for SZA = 14–37° (dark thick line in Fig. 31a), 212± 12K for SZA = 37–60° (green thick line in Fig. 31a) and 196 ± 15K for SZA = 60–83° (yellow thick line in Fig. 31a). In contrast, Mariner-6 and -7 reported 315–350K (L_s = 200°), Mariner-9 325K and 268K (L_s = 306–38° but probably with significant heating due a global dust storm; Bougher

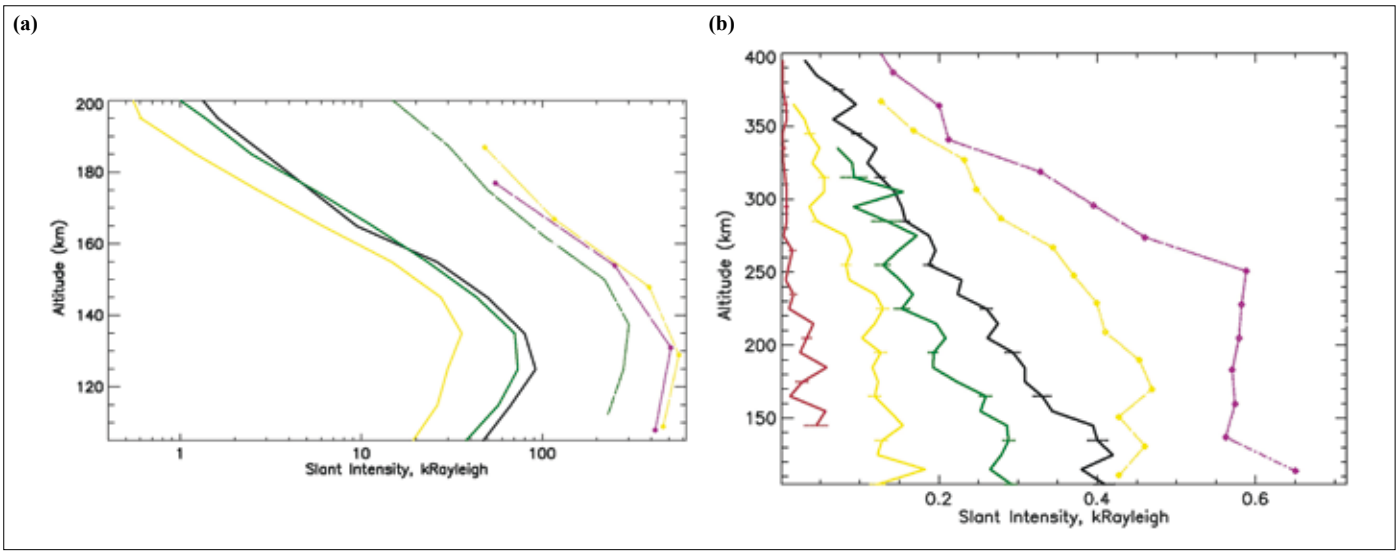

Fig. 31. (a) Cameron band emission (CO $A^3\pi$–X^1E^+, see Table 4) variation vs. altitude; and (b) O 130.4 nm emission variation vs. altitude. These profiles are for spectra measured at L_s = 135–171° and SZA = 14–37° (dark thick lines), 37–60° (green thick lines), 60–83° (yellow thick line) and 83–105° (red thick lines on panel b only). Dashed violet lines are from Mariner-6 data (L_s = 200°, one orbit at SZA = 27°), dashed yellow line from Mariner-7 (one orbit at SZA = 44°) and dashed green line (panel a only) from Mariner-9 (orbit 62). Each SPICAM profile was obtained using a few thousand individual spectra measured during 10 different orbits.

et al., 2000), Viking-1 and -2 145K and 186K ($L_s \sim 00°$), Pathfinder 153K (L_s = 143° on the nightside) and MGS from accelerometer measurements 220–230K (full martian year). The martian thermospheric GCM of Bougher et al. (2000) predicts a variation in temperature at solar minimum of 200–220K from aphelion to perihelion.

Figure 31b was plotted similarly, with the oxygen emission at 130.4 nm measured by SPICAM UV at 120–400 km and derived from the same set of spectra used to calculate the Cameron band emission displayed in Fig. 31a. Figure 31b clearly confirms that the dayglow emission during SPICAM observations was significantly weaker than at the time of Mariner-6 and -7. SPICAM observations also provide information on the dependency of the O atomic component in the exosphere *vs.* local time (not shown in Fig. 31), *vs.* SZA (Fig. 31b, also displaying a significant and surprising increase of the oxygen height scale with larger SZA) and *vs.* solar longitude (also not shown). Such observations will be analysed with a global 3D model of the martian corona (Leblanc & Johnson, 2001; Chaufray et al., 2005) and used to constrain models describing the interaction of Mars with the solar wind. For H Lyman-α measurements, the Jeans thermal escape is simple to compute once the exobase density and exospheric temperatures are determined by SUV from the vertical altitude distributions of H and O atoms. An essential tool for interpreting the H and O intensity data is a good radiative transfer model, such as that developed at Service d'Aéronomie by Bertaux, and maintained and improved by Quémerais & Chaufray.

5.2 The NO Band Emission on the Nightside

Thanks to the high sensitivity of the SUV and the ability of Mars Express to perform grazing-limb observations, the first martian nightside emissions were discovered (Bertaux et al., 2005a). Except for the occasional aurora (see below), the UV spectrum of this nightglow is composed of H Lyman-α emission (121.6 nm) and the γ and δ bands of nitric oxide (NO, 190–270 nm, respectively, transitions $A^2\Sigma^+$–$X^2\Pi$ and $C^2\Pi$–$X^2\Pi$), produced when N and O atoms combine to produce the NO molecule. This is reminiscent of the Venus nightside emission. While some UV Venus nightglow was detected by Mariner-5 (Barth et al., 1967) and Pioneer Venus (Stewart et al., 1979), the first spectrum was acquired with IUE and identified as NO radiative recombination (Feldman et al., 1979; Stewart & Barth, 1979). It was proposed that N and O atoms are produced by EUV photo-dissociation of O_2, CO_2 and N_2 in the dayside upper atmosphere, and transported to the nightside where recombination occurs, a mechanism later supported by 3D modelling (Bougher et al., 1990) and

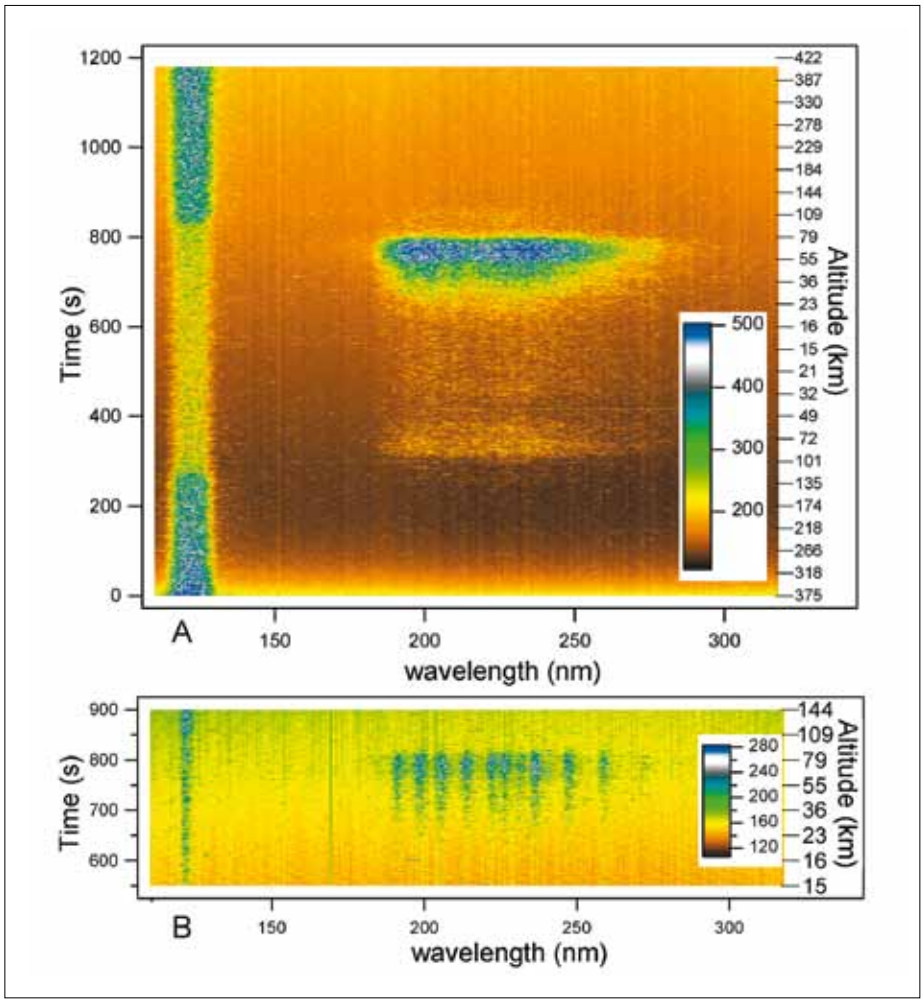

Fig. 32. Time variation of the nightglow spectrum along the grazing-limb observation. The intensity is colour-coded; these are raw data (ADU/pixel), uncorrected for dark current and radiometric sensitivity. *Top*: low spectral resolution band 4 (large slit), containing only Lyman-α emission at 121.6 nm and a broadband extending over 190–270 nm. The observation point is moving toward southern latitudes, while altitude falls and rises again as a function of time (right scale). *Bottom*: A subset of simultaneously recorded data at high spectral resolution (~1.5 nm). Band 1 (narrow slit) contains only Lyman-α emission at 121.6 nm and a well-structured band (190–270 nm), identified as NO γ and δ bands (Fig. 33). Some single-pixel vertical lines are artefacts due to pixels with a larger dark current. (From *Science*, Bertaux et al., 2005a)

discussed thoroughly in terms of atmospheric circulation. It is clearly the same mechanism on Mars, with important implications for atmospheric circulation.

At the time of this observation (orbit 734, 16 August 2004, 07:00 UT), the pericentre was on the nightside, at an altitude of 266 km and a latitude of 16°S. The spacecraft was descending from north to south (Fig. 8). The attitude was fixed inertially so that the LOS, aligned with the +*Z*-body axis, provided a grazing view of the limb as Mars Express passed through pericentre. As a result, the altitude of the LOS tangent point (Mars Nearest Point, MNP) changed from 375 km to a minimum of 15 km and back to 422 km. At the same time, the latitude changed from 11°S to 70°S. The whole altitude range at the limb was therefore scanned twice, but at different latitudes on the descending and ascending branches. The observations were taken around pericentre of orbit 734, Mars was at a solar distance of 1.66 AU and the season was $L_s = 74°$, near the northern summer (southern winter). The spectrometer slit was maintained parallel to the limb. Five band spectra were acquired (numbered 1–5; 32 CCD lines binned together): the first two with the narrow slit (spectral resolution of 1.5 nm), and three others with the wide slit during each second.

Figure 32 (top) is a colour-coded image of the time series of spectra of band 5 (low resolution). The most obvious spectral features are the H Lyman-α emission, visible at all times, and the broadband emission at 190–270 nm, of variable intensity, which was present only when the MNP altitude was lower than ~80 km. The higher resolution of band 1 (Fig. 32, bottom) reveals a well-structured band with a constant shape.

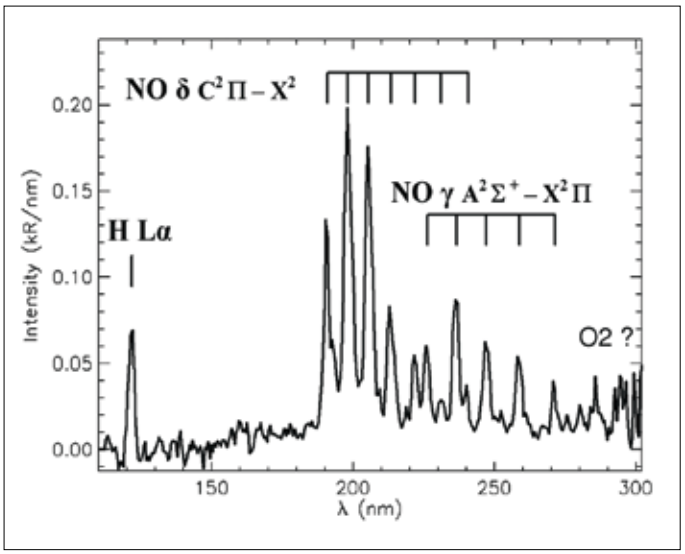

Fig. 33. Spectrum of the martian nightglow obtained during orbit 734. Except for Lyman-α at 121.6 nm, all the observed lines coincide precisely with the main NO γ and δ vibrational state transitions responsible for the Venus NO nightglow. The absolute radiometric calibration comes from SPICAM observations of hot UV stars. The total NO intensity is 2.33 kR, with a 74% contribution of the δ-band and 26% from γ-bands). The (0,1) line of the δ-band alone is, at 475 R, 27% of the total δ-bands. Spectral features above 280 nm could be attributed to the O_2 Herzberg I system, also expected from the recombination of O+O. (From *Science*, Bertaux et al., 2005a)

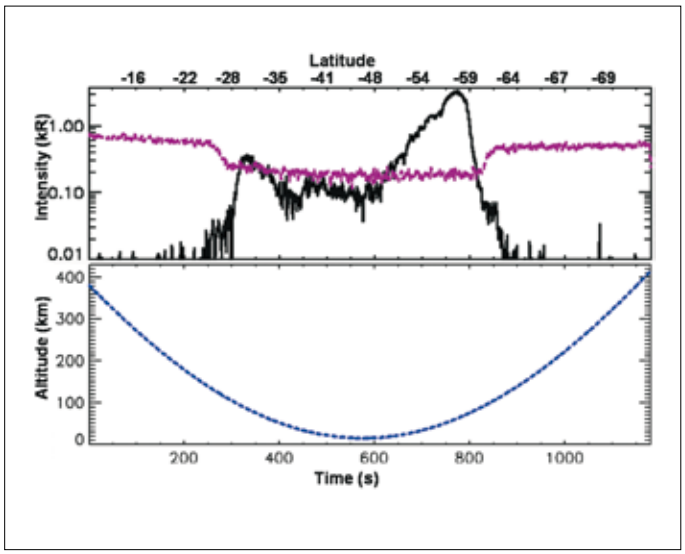

Fig. 34. *Top*: integrated intensity (wide-slit band corresponding to Fig. 32, top) of the Lyman-α emission and the whole NO band at 190–270 nm, as a function of time. *Centre*: altitude of the tangent point MNP. The NO emission displays two peaks, each time the LOS crosses 70 km altitude. The second peak is brighter by a factor of ~10, and is at high southern latitude. *Bottom*: latitude of the tangent point MNP. (Adapted from *Science*, Bertaux et al., 2005a)

By summing a number of spectra, the calibrated spectrum was obtained (Fig. 33), where the γ and δ bands of nitric oxide NO (transitions $A^2\Sigma^+–X^2\Pi$ and $C^2\Pi–X^2\Pi$, respectively) were identified.

Figure 34 plots the integrated intensity of the Lyman-α emission and the entire NO band region of 190–270 nm, as a function of time. The interplanetary Lyman-α emission and the martian corona Lyman-α emission from H atoms contribute to the observed emission. The martian Lyman-α emission is solar radiation scattered by H atoms on the dayside and transported to the nightside by radiative transfer. CO_2 is a strong absorber at Lyman-α, and the atmosphere of CO_2 is opaque to Lyman-α below the altitude at which $\tau = 1$ (optical thickness of CO_2 along the LOS at Lyman-α). Therefore, when the tangent point of the LOS is below this Lyman-α horizon, only the part of the LOS between the spacecraft and this opaque sphere contributes to the emission. The disappearance of the interplanetary emission and possibly some contribution of the martian corona beyond the tangential point is seen at times 280 s and 820 s after the beginning of observation, corresponding to the same altitude of 102±2 km and to a 1.64×10^{19} cm^{-2} CO_2 slant density for $\tau = 1$. This corresponds well to slant density estimates derived from SPICAM stellar occultations (see below) around this altitude; this type of observation is a new method for retrieving the CO_2 density and temperature at each limb crossing.

The light curve of the NO emission rate (Fig. 35) displays two peaks, 350 s and 770 s after the beginning of the observation (06:50:48 UT). The second peak is about 10 times brighter than the first. Both correspond to an LOS altitude of ~70 km, but to different latitudes, 35°S and 60°S, respectively. This behaviour can be explained by assuming a locally spherically symmetric NO emitting layer confined to a spherical shell of thickness ~20 km centred at 70 km altitude, but with a much more intense emissivity rate (photon/cm^3/s) at latitude 60°S than at 35°S. The emission seen at a tangent altitude below 60 km is produced essentially within

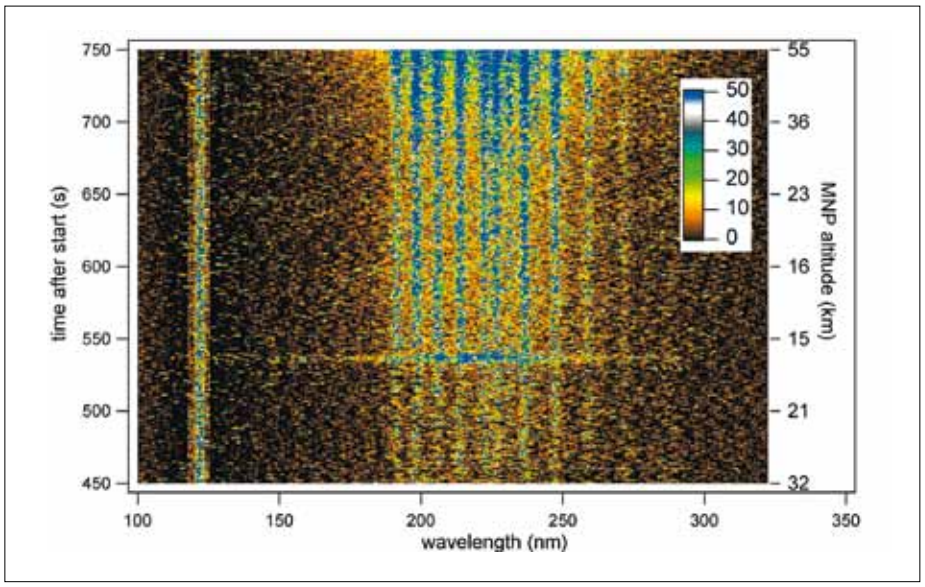

Fig. 35. Time variation of the martian nightglow intensity spectrum recorded during the grazing limb observation with spatial bin 2 (narrow slit, spectral resolution ~1.5 nm, one spectrum/s, data subset from 450 s to 750 s after the start of observation). It contains the H Lyman-α emission at 121.6 nm and a well-structured band (190–270 nm), identified as NO γ and δ bands (Fig. 33). The intensity in ADU/pixel is colour-coded. Altitudes of the MNP of the LOS are indicated at right. At the time of the peak marked 'aurora' in Fig. 36, the spectra are obviously different from the typical NO spectrum.

the portion of the 60–80 km shell, along the LOS, before or after the MNP point (Bertaux et al., 2005a).

The local emissivity rate of NO UV bands (in photon cm^{-3} s^{-1}) is proportional to the N and O abundances, [N] and [O]. At the altitude of their formation on the dayside, [N] and [O] are too small to give rise to detectable recombination. But when a gas parcel descends, both concentrations increase, and the emissivity rates will increase as the product [N] × [O], until a significant fraction of [N] (or [O]) atoms are recombined (according to models, the abundance of O is higher than N atoms, so [N] is the limiting factor for the NO emission). This leads to a layer of emission centred at an altitude of 70 km, corresponding to a CO_2 density of 2×10^{14} cm^{-3}.

The NO band intensity may be used to estimate the downward flux of N atoms in the polar night. The peak intensity of 2.2 kR of the NO δ band measured horizontally may be converted into a vertical intensity of 85 R, corresponding to 85×10^6 emitted photon cm^{-2} s^{-1}. Taking into account the fraction of photons emitted in the δ band with respect to all photons emitted $f = 0.77$, and $\varepsilon = 0.45$ the efficiency of the radiative N+O recombination as a loss process, this intensity corresponds to a total of 2.5×10^8 recombinations cm^{-2} s^{-1}, which must be compensated for by an equal downward flux of N atoms through the $z = 80$ km altitude level (at the place of the observation).

The observations were obtained at $L_s = 74°$, shortly before the southern winter solstice. At this season, the part of the atmosphere where the maximum emission intensity was observed at 70°S is never illuminated by the Sun. Any N and O present there must have been transported from lower latitudes, where sunlight was available to photodissociate N_2, O_2 and CO_2. The observed NO intensity can only be explained by a descending vertical flow in the upper polar atmosphere. This circulation pattern is consistent with GCM predictions (Forget et al., 1999). However, this model shows that, at this particular season, the circulation around 60 km is modulated by thermal tide waves that propagate from the lower atmosphere and are modified by the *in situ* heating due to the absorption of near-IR radiation by CO_2. These processes are key for understanding the upper atmosphere dynamics (and thus for future aero-manoeuvres, for instance), but they remain poorly understood. Numerical simulations results are model-dependent (Forget et al., 1999) and few observations are available. Within this context, the NO emission process identified here provides a powerful way to constrain GCM model behaviour above 60 km, in conjunction with spacecraft drag measurements (Keating et al., 2003).

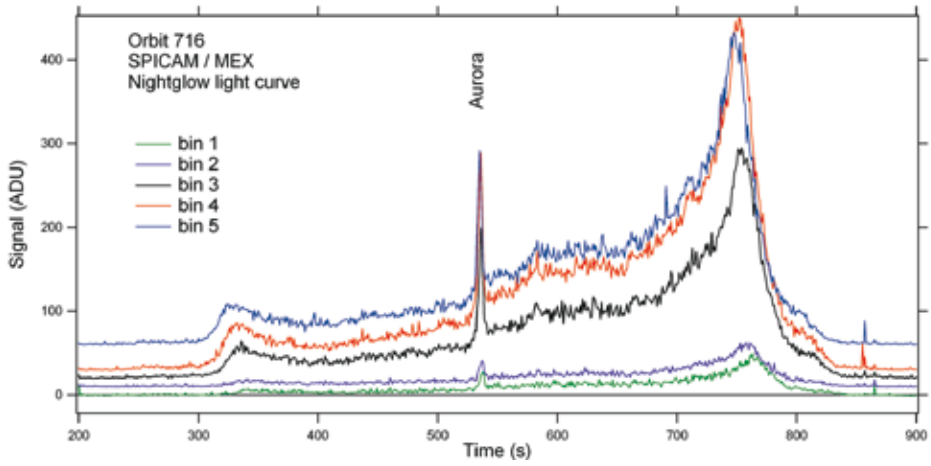

Fig. 36. Signal intensity for all five spatial bins as a function of time between 200 s and 900 s. Units are ADU per spectral pixel = 0.54 nm, averaged from 181 nm to 298 nm. There are 40 ADU per detected photon for the particular high voltage used here. The curves for spatial bins 2–5 are vertically displaced for clarity (respectively by 10, 20, 30 and 60 ADU). Spatial bins 3–5 have low resolution but high sensitivity, and bins 1 and 2 are less sensitive but have higher spectral resolution. A conspicuous spike marked 'Aurora' is observed in all bins at 535 s. This is the time at which the spectra in Fig. 35 differ from the usual NO spectrum. (Figure taken from *Nature*, Bertaux et al., 2005b)

5.3 The Discovery of Auroral Emission

Auroral emissions in planetary atmospheres 'are those that result from the impact of particles other than photoelectrons' (Fox, 1986). The potential of SPICAM's UV spectrometer to monitor these emissions is illustrated by the first observation of an aurora in the martian atmosphere (Bertaux et al., 2005b). It is a new type of aurora not seen before in the Solar System. Auroras on Earth and the giant planets lie at the feet of the intrinsic magnetic field lines near the magnetic poles. Auroras on Venus are diffuse, sometimes spreading over the entire disc. Martian auroras, in contrast, are a highly concentrated and localised emission controlled by the crustal magnetic field anomalies.

In the observation on orbit 716, the SPICAM LOS was permitted to drift slowly across the nightside limb to search for any weak emission, because no martian nightglow had been reported before, as sketched in Fig. 7. Figure 35 is a colour-coded image of the time series of high-resolution intensity spectra, similar to the NO observations. The most obvious spectral features are the H Lyman-α emission at 121.6 nm and the well-structured band at 190–270 nm of the NO molecule.

In Fig. 36 the nightglow signal, integrated over the wavelength range of the NO bands (181–298 nm), is displayed as a function of time for the five spatial bins. The signal is more intense for bins 3–5 than for bins 1 and 2 because the FOV is wider and the source is extended. All curves show the same behaviour, almost identical to the variation of the NO emission observed 6 days later on orbit 734, which is explained by the variation of the altitude and the latitude of the MNP when the LOS scanned across the NO emitting layer, confined in the altitude range 60–80 km, and more intense at high southern latitudes (around time 750 s). There is, however, a strong peak in all spatial bins between times 533 s and 540 s (increase by a factor of 3 to 4) that has no equivalent during orbit 734. The emission could be located by a kind of 'triangulation', using the five simultaneous FOVs of SPICAM UV. It coincides (Fig. 37) precisely with the region of strongest crustal magnetic field *B* reported by MGS (Acuña et al., 2001), and is a sign of electrons moving along the magnetic field lines, possibly connected to the interplanetary magnetic field at this location and time. The detected horizontal extent of this aurora is 30 km minimum, but it could be more extended along the LOS. The altitude of the observed emission is 129 ± 13 km. Still, it could extend more vertically, since it was scanned horizontally. The emissions in the Mars auroral spectrum (Fig. 38) are the CO $A^3\pi$–X^1E^* Cameron band between 180 nm and 240 nm (694 ± 50 R), long observed on the martian dayside (Barth et al., 1971), as well as emissions associated with atomic carbon resonances and with the CO $A^1\pi$–X^1E^+ fourth positive group between 135 nm and 170 nm, and emissions associated with the CO_2^+ B^2E^u–$X^2\pi_g$ doublet at 289 nm (71 ± 42 R).

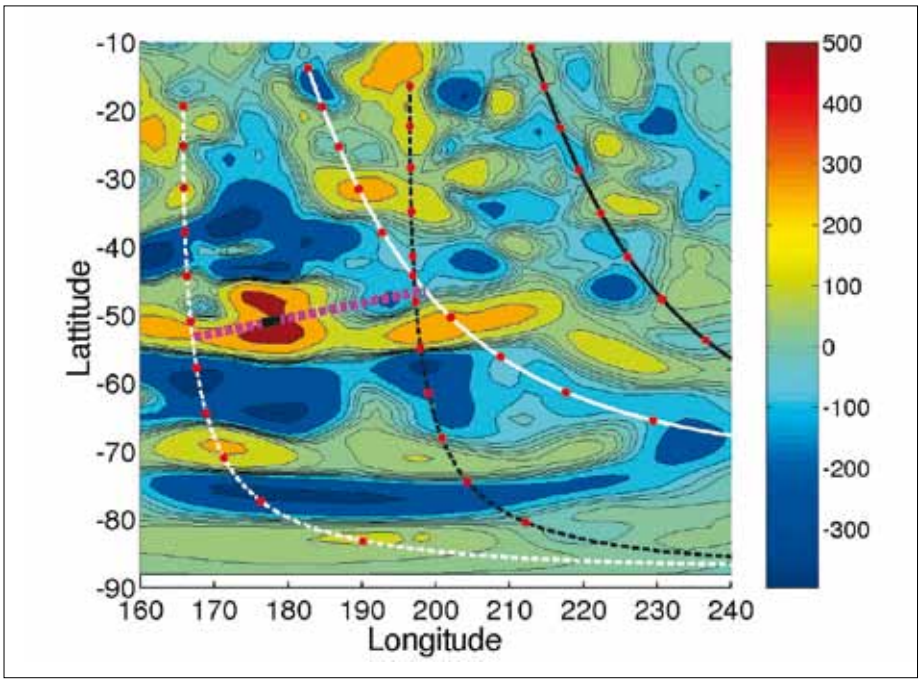

Fig. 37. Radial *B* field component (nT) at 200 km altitude of the crustal field deduced from MGS aerobraking and science phasing orbits (Acuña et al., 2001). White dashed line: satellite position during orbit 716 (start at the top and end of the orbit at the bottom of the figure). White solid line: position of the MNP. Dark solid and dashed lines: orbit 734 during which no emission was recorded. Magenta dashed line: SPICAM LOS at 535 s; the dark rectangle on the line is an estimate of the extended emitting region. (From *Nature*, Bertaux et al., 2005b)

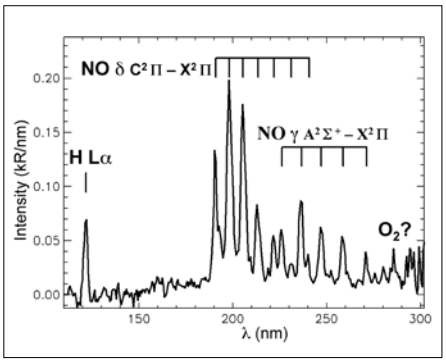

Fig. 38. Spectrum formed by averaging spectra obtained between observation times 541 s and 548 s, typical of the NO emission, which also contain the CO emission. (From *Nature*, Bertaux et al., 2005b)

6. Atmospheric Vertical Profiling by Stellar Occultation in UV

6.1 General Principles

The occultation technique has been used to measure O_3 in Earth's atmosphere since the 1970s. Early attempts observed only one or two wavelengths at a time, making the identification of the absorber species uncertain. With the advent of multi-pixel detectors, the absorbing species in a multi-spectral occultation can be safely identified via their spectral signatures. There is also the potential to discover new, unexpected species in the atmosphere. The method of absorptive occultation spectroscopy was reviewed by Roscoe et al. (1994) and Smith & Hunten (1990). In terrestrial stratospheric research, it has become the most advanced method for long-term monitoring of ozone. The most remarkable results in the IR are from ATMOS/Atlas, which provided a set of high-resolution spectra of Earth's atmosphere. In the UV–visible, SAGE-3 uses full wavelength coverage of the Sun. The Scanning Imaging Absorption Spectrometer for Atmospheric Chartography (SCIAMACHY) of Envisat (ESA, 2001) is performing solar occultation and nadir observations, while the Global Ozone Monitoring by Occultations of Stars (GOMOS) instrument is dedicated to monitoring ozone and other species by stellar occultations (more than 400 000 ozone, NO_2 and NO_3 profiles have been collected so far; Hauchecorne et al., 2005). SPICAM is thus in line with the most advanced instrumentation deployed for studying Earth's atmosphere.

So far, the only solar occultation measurements at Mars were performed during the Phobos mission by the Auguste instrument (Blamont et al., 1989; Krasnopolsky et al., 1989). Although the mission was not fully successful, the solar occultation studies covered more than a month, significantly improving our knowledge of the martian water vapour profile (Krasnopolsky et al., 1991; Rodin et al., 1997), aerosol vertical distribution (Chassefière et al., 1992; Korablev et al., 1993) and ozone distribution (Blamont & Chassefière, 1993). The promising results were not fully developed because of the failure of the Mars-96 mission.

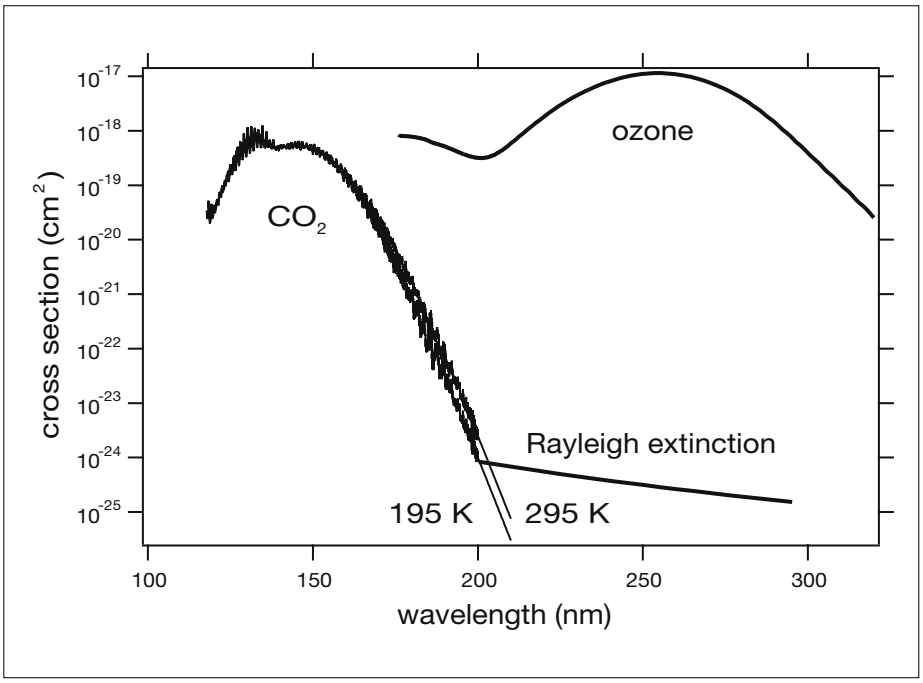

Fig. 39. Extinction cross-sections of CO_2 and ozone for temperatures found at Mars in SPICAM's spectral range. Aerosols/dust would add to the absorption. Rayleigh extinction for CO_2 is indicated.

SPICAM is the first instrument to use stellar occultations at Mars, routinely delivering vertical profiles of CO_2 density, temperature, ozone and aerosols by measuring the atmospheric transmission as a function of wavelength, as originally planned for SPICAM on Mars-96. The methodology is to use the spectral absorption of atmospheric components to retrieve their vertical distributions. The spectrometer's UV wavelength range of 110–300 nm encompasses the whole CO_2 absorption band (110–200 nm) and the ozone Hartley band centred at 250 nm (Fig. 39). Dust absorbs everywhere, but is easier to see above 200 nm, clear of the CO_2 absorption.

The principle of using a stellar occultation to measure atmospheric transmission is quite simple (Fig. 40). Along the spacecraft orbit, stars are occulted one after another by the planetary limb opposite to the velocity vector. At a predetermined time, the spacecraft is oriented so that SPICAM's LOS points towards a given star. The stellar spectrum is recorded above the atmosphere (say, at 200 km), unaltered by atmospheric absorption, to serve as a reference spectrum $F_0(\lambda)$. Then, while the spacecraft is maintained on a 3-axis inertial attitude, the LOS to the star cuts deeper and deeper into the atmosphere, down to total occultation. At 1 s intervals, the spectrum $F(\lambda,z)$ is recorded as the LOS slices through the atmosphere at a tangent altitude z. The atmospheric transmission at z is:

$$T(\lambda,z) = F(\lambda,z) / F_0(\lambda)$$

The first step in the data processing is to establish the transmission by correcting instrumental effects (the CCD dark charge) and perhaps background light at the limb.

The second step is to fit a simple forward model to the measured transmission at each altitude (spectral inversion):

$$T_{mod}(\lambda,z) = \exp(-\sigma_{CO_2}(\lambda)\, N(CO_2) - \sigma_{O_3}(\lambda)\, N(O_3) - \tau_{dust}(\lambda))$$

where $\sigma_{CO_2}(\lambda)$ and $\sigma_{O_3}(\lambda)$ are respectively the cross-sections of CO_2 and ozone, and $N(CO_2)$ and $N(O_3)$ their slant densities (along the LOS), and $\tau_{dust}(\lambda)$ is the optical thickness of dust, described by 1, 2 or 3 parameters as a function of λ.

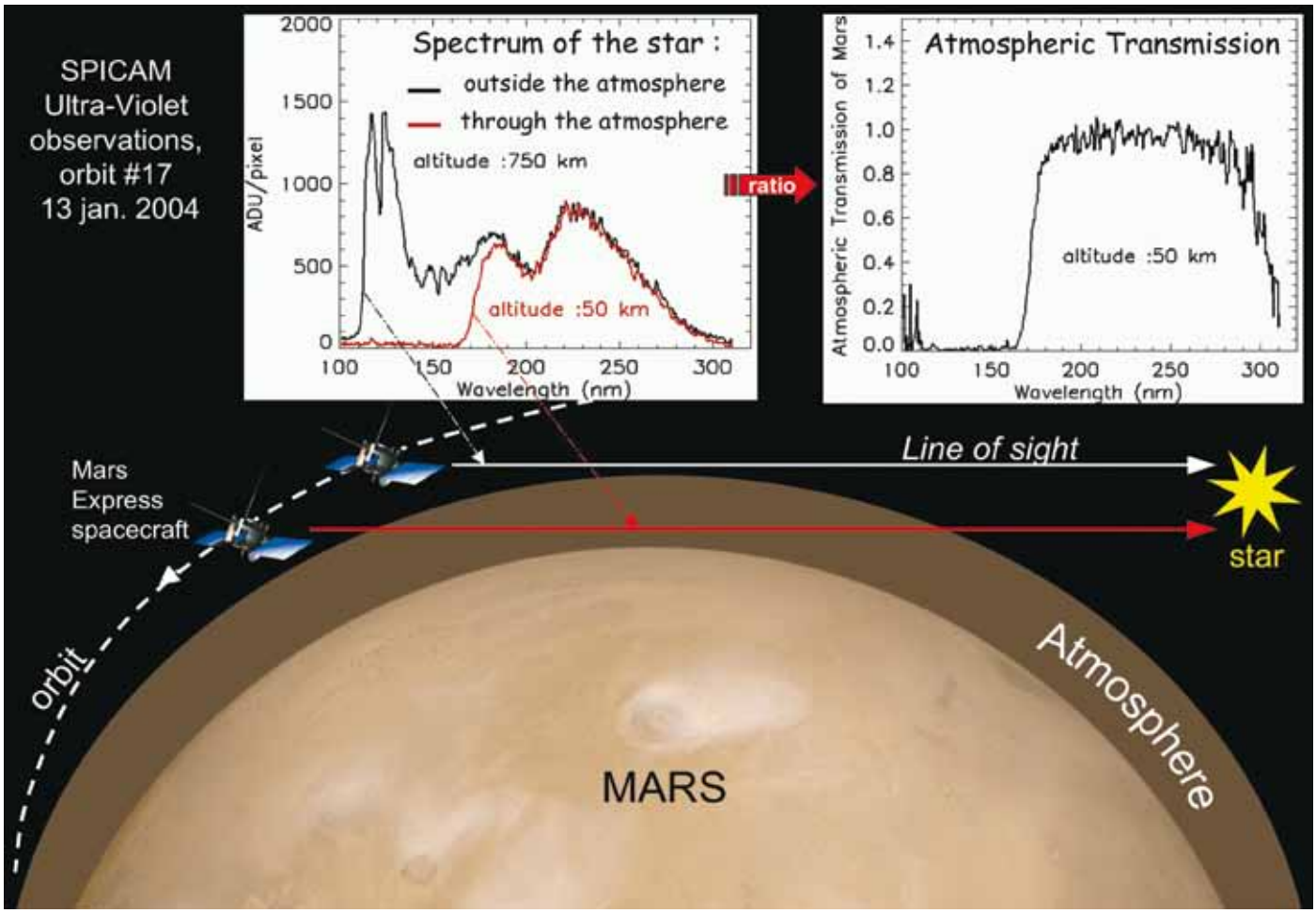

Fig. 40. The occultation principle. From the two spectra obtained outside and through the atmosphere, atmospheric transmission can be derived. The spectra shown here come from the very first stellar occultation made by SPICAM at the beginning of the mission, the first by any instrument at Mars. Shortward of 180 nm, the signal is completely attenuated by CO_2.

The third step is to perform the vertical inversion of the slant densities, to retrieve the local densities by a modified onion-peeling technique, including Tikhonov regularisation inspired from GOMOS work.

From the retrieved CO_2 density, the vertical profile is integrated from the top to yield the pressure, and the law of perfect gases is applied to determine the temperature. The CO_2 density is retrieved from about 150 km altitude down to 10–30 km, depending on the dust load in the lower atmosphere, where the star signal disappears. For solar occultations, a lateral viewport is used, and five points on the Sun are recorded together, allowing retrieval of five profiles at each occultation, to be merged together.

The three steps are described here for stellar and solar occultations. As expected, stellar occultations at deep night are preferred because of minimal limb light background. Retrieval simulations with expected instrumental characteristics were performed before flight (Korablev et al., 2001).

Stellar occultation offers three important features:

— an absolute concentration derived from a relative measurement (the method is self-calibrating, so there is no need for instrument calibration);
— excellent vertical resolution whatever the distance to the planet (because the star is a point source);
— the accuracy of the altitude knowledge is independent of the spacecraft attitude, unlike limb-emission methods. The LOS is entirely determined by the direction of the star in the sky (known) and the position of the platform along its orbit.

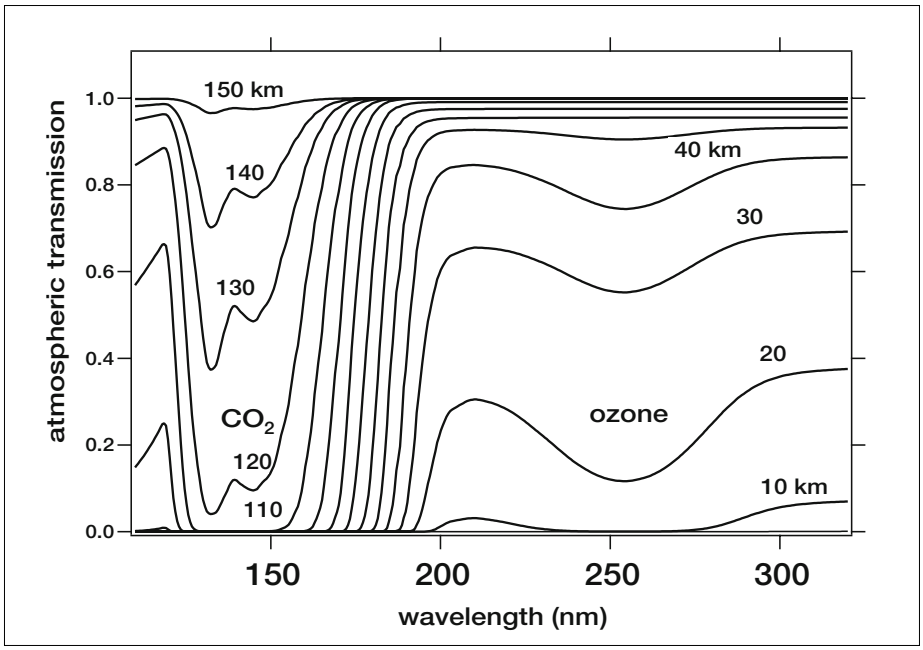

Fig. 41. Synthetic spectra of Mars atmosphere transmission in occultation for various grazing altitudes. Dust is taken into account here, mostly visible as a continuous and absorption above 210 nm (with some slope).

Stellar occultations are observed preferably on the nightside of the orbit, and do not affect the operation of dayside mapping instruments. The LOS is oriented towards a bright UV star and maintained during the whole occultation of typically 1–4 min; SPICAM is ON for 20 min. Limiting the number of occultations is the spacecraft orientation, which is a resource to be shared between the various investigations. This procedure has several features:

— when a star is occulted during one orbit, it will be occulted on following orbits at about the same latitude, but at different longitudes;
— the vertical profiling is not restricted to the spacecraft track, unlike other methods;
— hot stars are preferred because they are brighter in UV. Their UV spectra are flatter than the solar spectrum, with more UV below 200 nm, so stellar occultations can probe higher altitudes than solar occultations;
— rising stars can also be followed because the tracking system is not closed-loop.

The CO_2 cross-section presents an enormous dynamic range in the UV, so CO_2 absorption is detectable beginning at an altitude of 150 km. For decreasing tangential heights, the CO_2 has a sharp cut-off that increases in wavelength, up to 200 nm at z = 80 km (Fig. 41). Longward of 200 nm, the transmission spectrum is dominated by dust and CO_2 Rayleigh extinction, with an ozone trough at 255 nm. The trough depth is a direct measure of ozone line density. From the signal-to-noise ratio in the stellar occultation mode, the O_3 line density N_h accuracy depends on the UV magnitude of the star. The Rayleigh extinction above 200 nm can be computed from the CO_2 line density determined below 200 nm, and the remaining continuous absorption above 200 nm is attributed to the dust/aerosol content, allowing determination of the vertical distribution and spectral characteristics in the UV (Figs. 42 and 43).

Results from Mars Express stellar occultations have been presented at a number of conferences; see Quémerais et al. (2006) on the data and inversion processes, Montmessin et al. (2006) for the cloud and dust distributions, Forget et al. (2006) for the CO_2 density and temperature measurements, and Lebonnois et al. (2008) for the ozone results. These last three topics are summarised below.

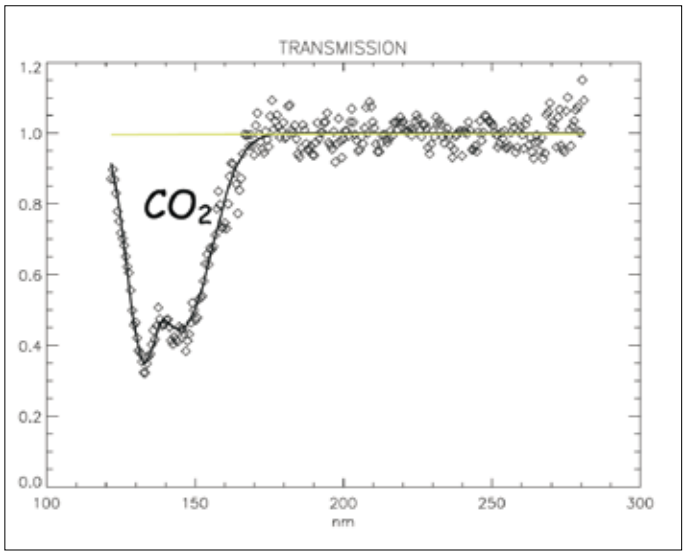

Fig. 42. SPICAM measurements of spectral atmospheric transmission during a stellar occultation at high altitude, where only CO_2 absorption is present.

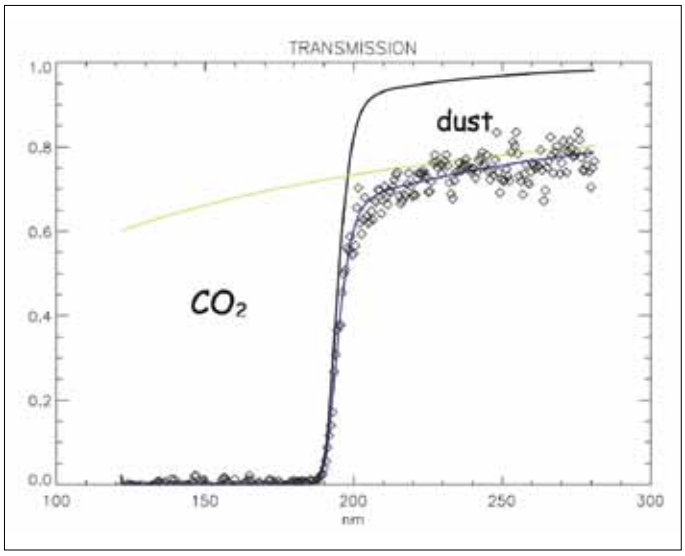

Fig. 43. As Fig. 42, but lower in the atmosphere. The green curve is the absorption attributed to aerosols fitting the data, in addition to CO_2 absorption and Rayleigh extinction.

6.2 CO_2 Density and Temperature Profile

6.2.1 Thermal structure of the martian atmosphere

Theory tells us that the temperature structure of the thermosphere above 120 km is dominated by the balance between EUV heating, non-LTE cooling and molecular diffusion. In the middle atmosphere (40–120 km) the vertical structure is determined primarily by non-LTE solar heating and radiative cooling in the absorption bands of CO_2, and by solar EUV heating at higher levels. The thermal structure is modified by the circulation driven by this force, and by tides and gravity waves that propagate from the lower atmosphere, break and deposit their energy in this region. Lower- and upper-level circulation models (including GCMs) were extended into the middle atmosphere, and need adequate temperature/density data to be validated.

Until recently, there were few temperature profiles of the upper atmosphere: Viking Lander entry profiles (Seif & Kirk, 1977), and an indirect derivation above 120 km from Mariner-9 airglow (Stewart et al., 1972). New profiles were derived from Mars Pathfinder entry accelerometry (Magalhaes et al., 1999) and MGS aerobraking data (Keating et al., 1998). The MGS Thermal Emission Spectrometer produces 3D temperature fields up to 35 km in nadir mode, and up to 65 km when limb viewing (Conrath et al., 1998; 1999). Radio occultation studies from Mars probes have resulted in profiles below 20 km (see Hinson et al., 1999 for recent Pathfinder profiles). Ground-based microwave observations based on CO lines profiling (Clancy et al., 1990) constrain temperature profiles on large (planetary) scales up to 50 km. Yet the thermal structure and the circulation of this part of the atmosphere is of primary importance on Mars. Unlike on Earth, where the circulation in the troposphere is somewhat decoupled from the circulation in the stratosphere and troposphere, the vertical extension of the meteorological phenomenon on Mars appears to be considerable. In some cases, it probably reaches the top of the neutral atmosphere, around 120 km (e.g. the Hadley cell during northern winter). The circulation there may even affect the meteorology at much lower altitudes (Forget et al., 1996). For instance, the strong warming of the polar night atmosphere during dust storms is thought to result from an enhancement of the meridional wind between 60 km and 100 km (Wilson, 1997). In fact, this behaviour of the martian atmosphere may limit the performance of the GCMs and thus our understanding of the martian

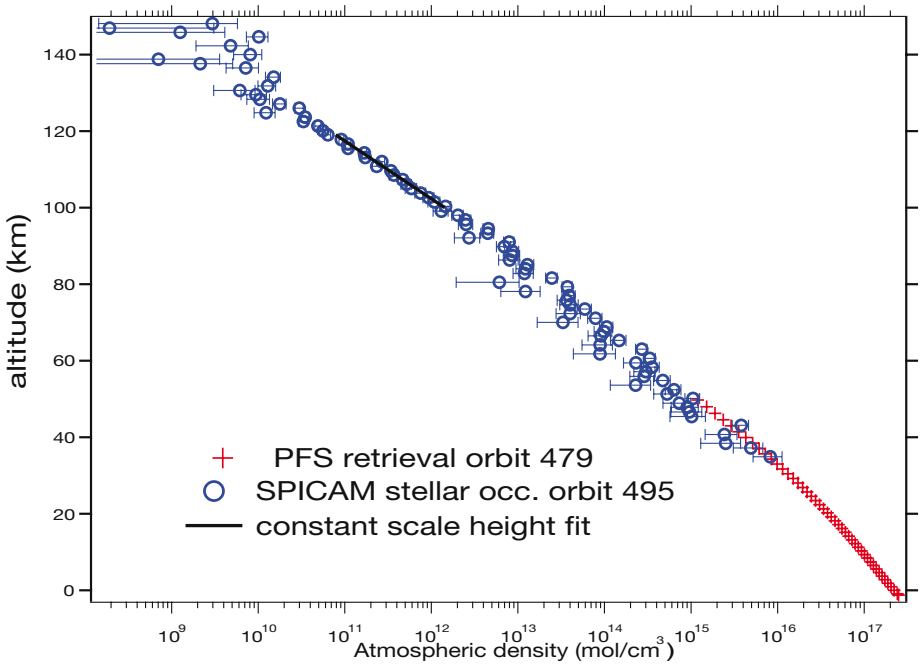

Fig. 44. An example of density retrieval. The PFS data (courtesy D. Grassi and V. Formisano), illustrate good agreement. The PFS air-temperature fields are retrieved in the indicative range 3–45 km via numerical inversion of the radiance observed in the CO2 15 μm band, performed on a single-spectrum basis. The resulting profiles have a vertical resolution of the order of some km, intimately limited by the nature of radiative transfer. The SPICAM vertical profile is obtained by stellar occultations during a nearby orbit. The PFS and SPICAM vertical profiles overlap at 30–60 km, showing good agreement between the retrievals.

meteorology. How can we account for these upper atmospheric processes? Is the lower thermosphere circulation of importance? Their limited vertical coverage (<65 km) means that MGS/TES and similar instruments cannot solve the problem, leaving SPICAM as the single optical spectroscopy experiment covering this altitude range.

6.2.2 Data analysis

Once the line density of CO_2 is determined from the transmission spectra for each altitude (one altitude per second), the local density $n(z)$ is determined from an Abel vertical inversion of the line density vertical distribution during a single occultation. The hydrostatic equation then allows temperature to be determined (Quémerais et al., 2006). Figure 44 is an example of density retrieval in the atmosphere of Mars. The inclusion of Planetary Fourier Spectrometer (PFS) data illustrates the good agreement and the complementarity of the two sets of measurements as a function of altitude.

There is some dependence of CO_2 absorption cross-section on the temperature T; the retrieval process in this case is more complicated, so this effect has been ignored so far.

Although night stellar occultations are preferred, some daytime occultations must also be performed on especially bright stars on the bright limb. On Mars Express, the pointing is usually so good that the star image can be placed in SPICAM's 50 μm slit (0.02°). SPICAM UV offers a fair cover of density/temperature profiles as a function of local time, latitude, geography and solar activity: the sampling is a crucial test of the validity of sophisticated thermospheric GCMs. Once validated (or invalidated and modified accordingly), such models could be used as predictive tools for managing aerocapture/aerobraking operations in the future.

Figures 45 and 46 present examples of two slant-density profiles compared with the prediction of the GCM of Forget et al. (1999) run for the same time and location. Figure 45 shows a significant drop in the data at altitudes <100 km, not predicted by the model, while in Fig. 46 the agreement with the model is much better at high altitudes. For a while, it was suspected that the discrepancy could come from neglecting the variation of CO_2 cross-section with temperature for this very cold region (a small scale-height for the slant-density implies a low temperature). However, that would produce a systematic discrepancy, which is not found. In addition, high-

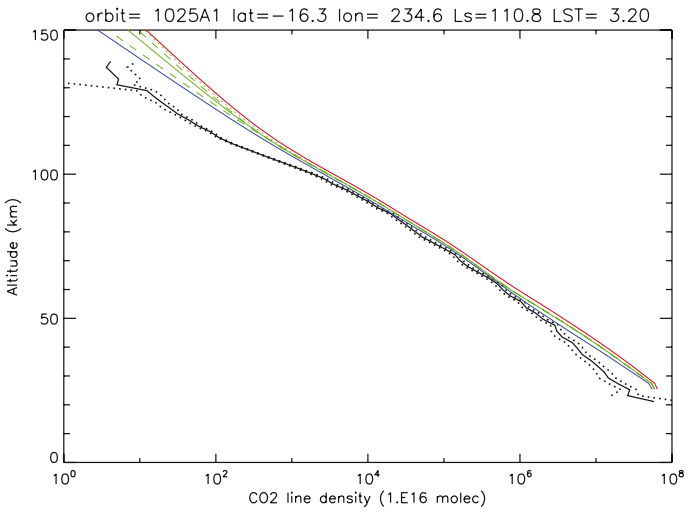

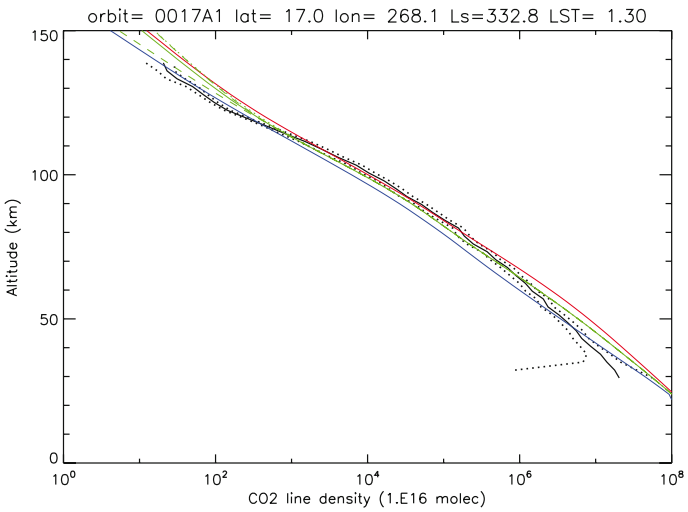

Figs. 45 (*left*) and 46 (*right*). Comparison of measured slant-density profiles with the prediction of the GCM of Forget et al. (1999) run for the same time, geometry and location. The black line is the SPICAM data, with dotted lines at ± error bar. Several models are compared. Blue curve: clear (no dust); green curve: MGS scenario; red curve: dusty atmosphere. There is a significant deficit of CO_2 above 100 km in the data, which is not present on other orbits (Fig. 46, right). It must therefore be real, and indicates a low temperature in the region 100–110 km.

altitude clouds were detected on some occasions (see below), always connected to low temperatures at high altitude. The profile of Fig. 45 is therefore seen as realistic and is fully confirmed by the extensive analysis of CO_2 and temperature profiles presented in Forget et al. (2008).

6.2.3 The case for molecular oxygen

Molecular oxygen is the result of CO_2 photo-dissociation. O_2 provides in the Schumann–Runge bands (170–210 nm) an additional absorption that should be measurable. Calculations show that the difference in transmission between an atmosphere with O_2 ($O_2/CO_2 = 10^{-3}$) and one without O_2 amounts to 2% around 80 km, in a bandwidth of about 20 nm around 190 nm. The absorption decreases somewhat below. In principle, one expects a constant mixing ratio of O_2 in altitude and over the planet, inasmuch the chemical reactions that control this molecule are understood, constantly produced by photo-dissociation of CO_2. The UV occultation technique is one way to access this important molecule. Although on Mars there is a conspicuous O_2 emission at 1.27 µm, it is produced by photo-dissociation of ozone. It does not trace the density distribution of O_2 as would the UV absorption seen in occultation. Some recent processing at LPL appears to have definitely found O_2 UV absorption, with a mixing ratio of 0.7% (Lewis & Sandel, private communication). This is a high value compared to the adopted value of 0.13% derived from Viking measurements. If confirmed, it would be an important feature to reproduce in the modelling of photo-dissociation of CO_2.

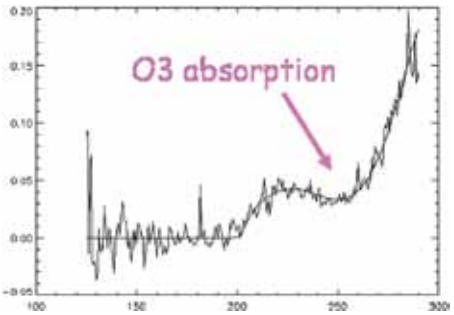

Fig. 47. Spectral transmission at 15 km altitude during orbit 174 (a single 1 s measurement). The ozone absorption trough is well seen, superimposed on the dust continuum above 200 nm wavelength.

6.3 Ozone Vertical Profiles from Stellar Occultations

The analysis of transmission spectra yields slant densities of CO_2, dust and ozone as a function of altitude. Inversion of these vertical profiles allows us to retrieve vertical profiles of local densities, with an altitude resolution of close to 5 km. Before Mars Express, there was only a single ozone vertical profile, obtained by Blamont & Chassefière (1993) by solar occultation on the Phobos-2 mission. The quality was not excellent, partly because the ozone quantity was low at that season. For SPICAM's numerous stellar occultations, some show no detectable ozone, but on others the UV absorption signature is quite conspicuous, as illustrated in Fig. 47.

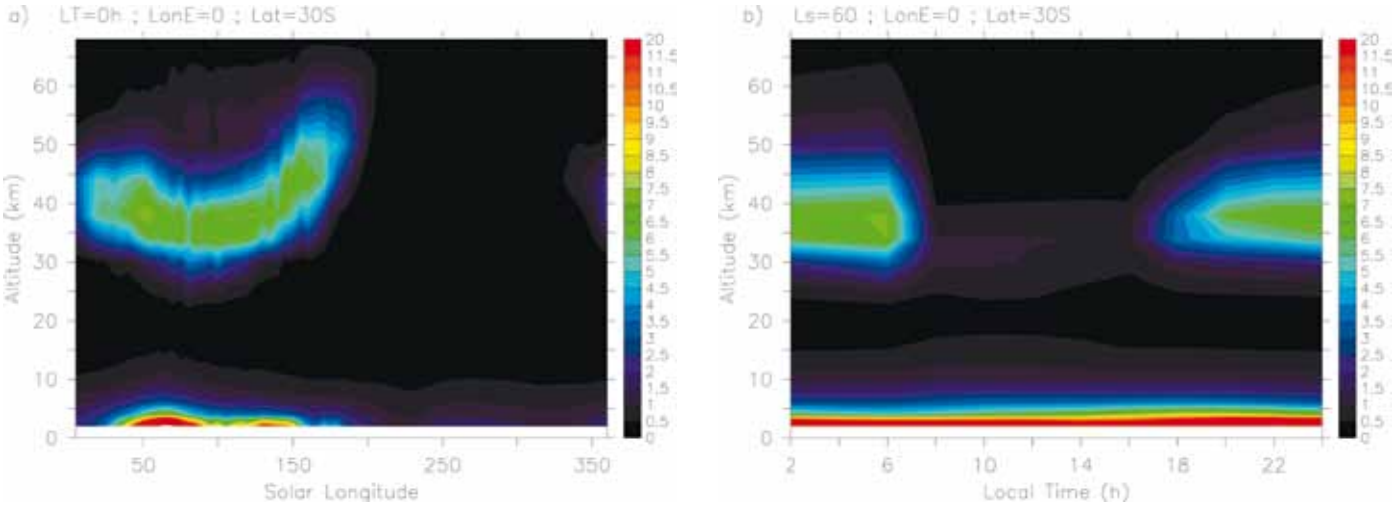

Figs. 48 and 49. Evolution of the vertical distribution of ozone in the GCM (Lefèvre et al., 2004) at (0°E/30°S) as a function of (a) solar longitude, local time is fixed to midnight; and (b) local time, solar longitude is fixed to 60°.

Vertical profiles of ozone in the altitude range 20–30 km to 70 km are analysed here as functions of the latitude and season (solar longitude, L_s) of the observations. The occultations analysed so far mainly cover the southern hemisphere, during autumn and winter (L_s = 8–155°). Most are taken at night. The upper limit for detection of ozone is a density of roughly 10^8 cm^{-3}, and the error bars are usually of a few 10^8 cm^{-3}, rising to 10^9 cm^{-3} when the profile is especially noisy. The profiles show the presence of two ozone layers: one near the surface, the top of which is visible mainly in high-latitude occultations, below 30 km altitude; another layer at 30–60 km altitude, with characteristics that are highly variable with latitude and season.

The higher layer is first seen on orbit 247, at L_s = 11°, 16.8°N/2.3°E, with a peak abundance of $(4.7 \pm 0.7) \times 10^8$ cm^{-3} at 52 km altitude. On both sides of the equator, the ozone abundance at the peak (~45 km altitude) tends to increase from 1–4 × 10^9 cm^{-3} until L_s ~ 40°, where it stabilises at around 6–8 × 10^9 cm^{-3}. After the southern winter solstice (L_s ~ 100°), the peak abundance starts to decrease again, and this ozone layer is not detected after L_s ~ 130°. At high southern latitudes (above 60°S), a small ozone layer is observed around 50 km altitude, with an abundance of approximately 2–5 × 10^8 cm^{-3}. At these high latitudes, below 30 km, ozone increases with decreasing altitude, indicating the presence of a surface layer of ozone. On some profiles, structures are observed within one of these ozone layers.

A recent model (Lefèvre et al., 2004) predicted the presence of these two ozone layers (Figs. 48 and 49). At this season, a nocturnal layer at 30–70 km altitude is predicted. This layer arises at sunset from the recombination of O atoms, but is destroyed by UV photons when the Sun rises. Its abundance is linked to the amount of HO_x radicals, and therefore of water vapour, present at these altitudes. This water vapour abundance is linked to the altitude of the hygropause, which is variable with season. Around aphelion season (L_s = 71°), the hygropause is low, and this modelled ozone nocturnal layer is predicted to be quite stable during the northern spring and summer. The densities of ozone observed during L_s = 40–100°, for mid- to low latitudes is in good agreement with the model, but the observed seasonal behaviour is different, which implies that season-dependent mechanisms destroying ozone are underestimated in the model. At high latitudes, the altitude layer is also overestimated by the model. The observed top of the surface layer is also in general good agreement with the model. This difference in the seasonal behaviour between observations and the model may be linked either to the vertical distribution of water vapour and its evolution with season, or to the possible role of heterogeneous chemistry at the surface

of dust particles or water ice clouds. SPICAM observations have the potential to explore both hypotheses in more detail in future studies.

6.4 Stellar Occultation Results: Aerosol Vertical Profiles

6.4.1 Impact of aerosols on the martian climate

An important component of the martian atmosphere is dusty and volatile aerosols. The strong involvement of the aerosols in basic climate fields means that the lower atmosphere can be considered as a 'dusty climate' system. There is a permanent haze with a column optical depth of 0.1–1, depending on the season, with sporadic increases up to several units during dust storms, which is known to control temperatures in the troposphere and lower stratosphere. Heating and cooling by aerosols drive dynamical phenomena, varying in scale from general circulation to local waves that give rise to the atmospheric turbulence. The content and distribution of aerosols in the atmosphere are in turn controlled by atmospheric motion, as part of the complex feedback that makes the current climate extremely variable. Volatile aerosols also affect the thermal field by changing the optical properties and settling rates of particles. They therefore provide strongly nonlinear thermal feedback determined by the saturation curve, which is expected to be most significant during aphelion (Clancy et al., 1996; Rodin et al., 1999).

6.4.2 Observation description

While aerosols/dust may be observed on the dayside via their emission of scattered solar light, the stellar occultation technique remains unique for detecting condensation clouds during the night, in addition to plain dust particles. Figure 50A indicates the actual star spectrum signal as a function of MNP altitude and wavelength for a typical occultation. At high altitudes (z > 150 km), there is no absorption, and the structure of the signal is due to the spectrum of the star, with a strong peak at short wavelengths. The structure of CO_2 absorption is clearly visible at 120–180 nm, with a fainter region of ozone absorption around 250 nm. Quantitatively, for each occultation, the ratio of spectra taken through and outside the atmosphere gives an atmospheric transmission at each altitude above the point on the surface that is closest to the slant. If there is any absorbing or/and scattering species along the optical path between the star and the spacecraft, photons are lost and the resulting transmissions are lower than 1. The fitting procedure of the measured transmission is based on a Levenberg–Marquardt algorithm that is fed with the LOS-integrated (slant) molecular concentrations of carbon dioxide, ozone and the opacity created by aerosols along the LOS. Values returned for each parameter are compiled to determine the resulting vertical profile of each species. Figure 50C compares a fitted transmission spectrum and transmission derived from the data. It illustrates the prominent signatures of CO_2 and O_3 and shows the transmission attenuation created by aerosols over the whole spectral range. The comparison of transmission vertical profiles at specific wavelengths (Fig. 50B) confirms the consistency of the fitting procedure.

6.4.3 Detection of a seasonal signal

Since the very first occultation sequence made on 13 January 2004, more than 500 profiles have been collected by SPICAM. Some sequences were lost due to pixel saturation, or to a mispositioning of star image on the detector. A total of 412 could still be treated and yielded vertical profiles of atmospheric species, including aerosols (Fig. 51). The dataset spans a period between the end of the northern winter (at L_s = 330°, corresponding to the arrival of Mars Express) and the beginning of the northern autumn (L_s = 200°). Most observations were performed in the southern hemisphere.

Stellar occultation requires only the faint light of stars, so it offers coverage of night regions. On Mars, this is of particular interest because a crucial part of the climate is played out in the polar night regions where surface temperatures fall below the CO_2 condensation point. CO_2 condensed on the ground leads to significant seasonal variations in global pressure. Unfortunately, this aspect of the martian climate is incompletely documented. Temperatures have been retrieved from IR measurements,

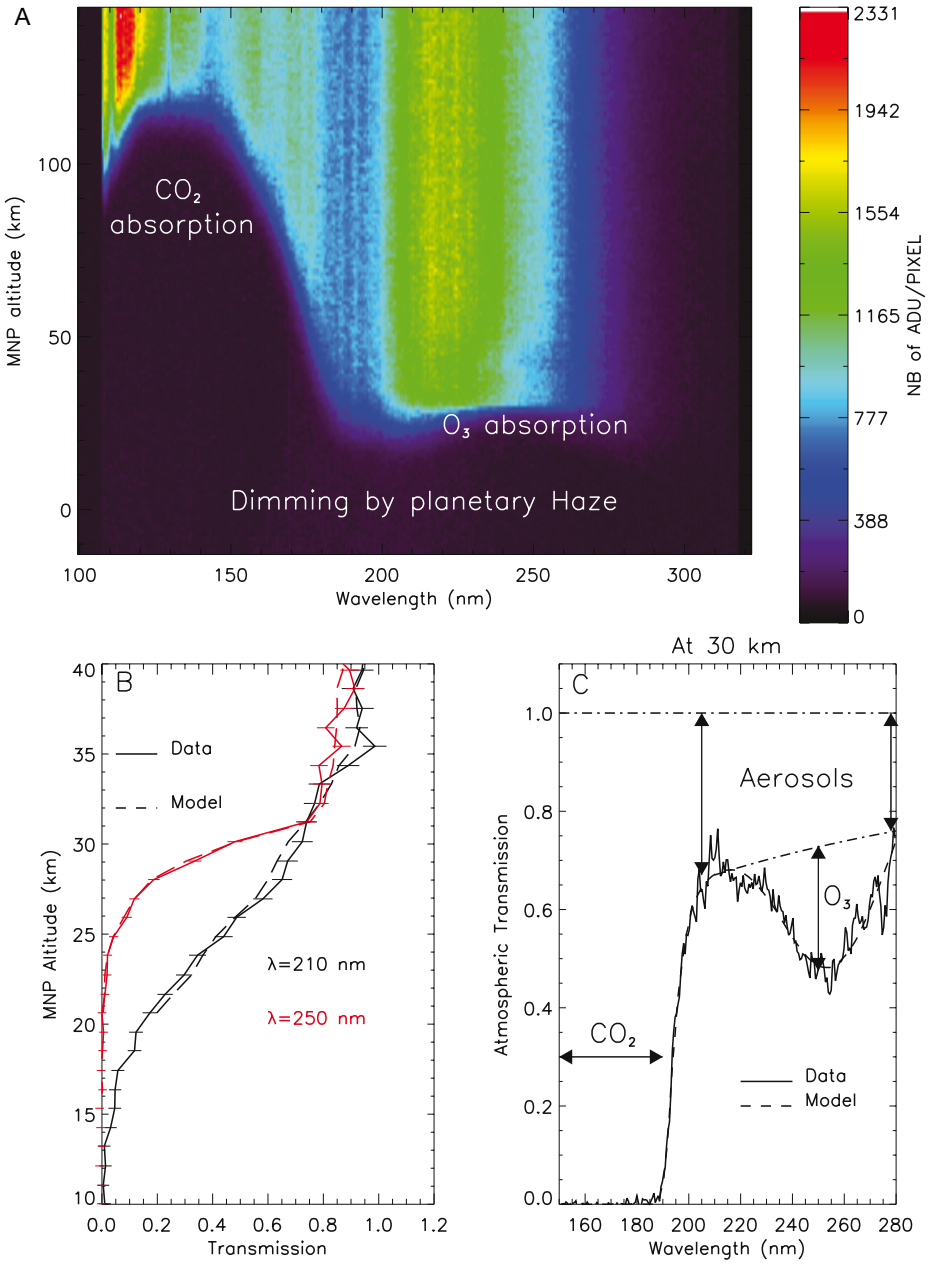

Fig. 50. A: sequence of spectra derived from orbit 505. The star signal (colour-coded in ADU) is plotted as a function of wavelength; as of the MNP altitude it is unabsorbed above 150 km. Below this, EUV absorption by CO_2 is clearly identified at 120–180 nm, while ozone absorption is seen at 220–280 nm. Atmospheric species can be derived down to 30 km. B: for the same orbit, a comparison of transmission profiles at two UV wavelengths. Modelled transmissions fitted to the data are plotted together with data values and corresponding error bars. C: a transmission spectrum and its fit. The spectrum was collected at 38 km, where the signatures of CO_2, O_3 and aerosols can be easily identified.

but there were almost no observations to infer the vertical structure of haze in these regions. The abundance of aerosols in the polar night is known to control the intensity of planetary-sale waves propagating in the mid-latitudes of both hemispheres during autumn and winter. Also, theoretical studies have produced the possibility of CO_2 storms in the polar night owing to the brutal release of latent heat during atmospheric condensation episodes. Observations collected so far by SPICAM do not support the existence of such meteorological phenomena. Instead, polar night regions are marked by the presence of a thin haze extending from the ground up to 30 km, probably composed of submicron particles. This type of haze vertical structure is consistent with a lack of convective activity, resulting from the roughly isothermal structure of the atmosphere. The presence of haze particles so deep in the polar night is nonetheless puzzling. No spectral signature can be used to identify the particle composition. If it is dust, it is possible that the particle size range estimated from the data may reflect the

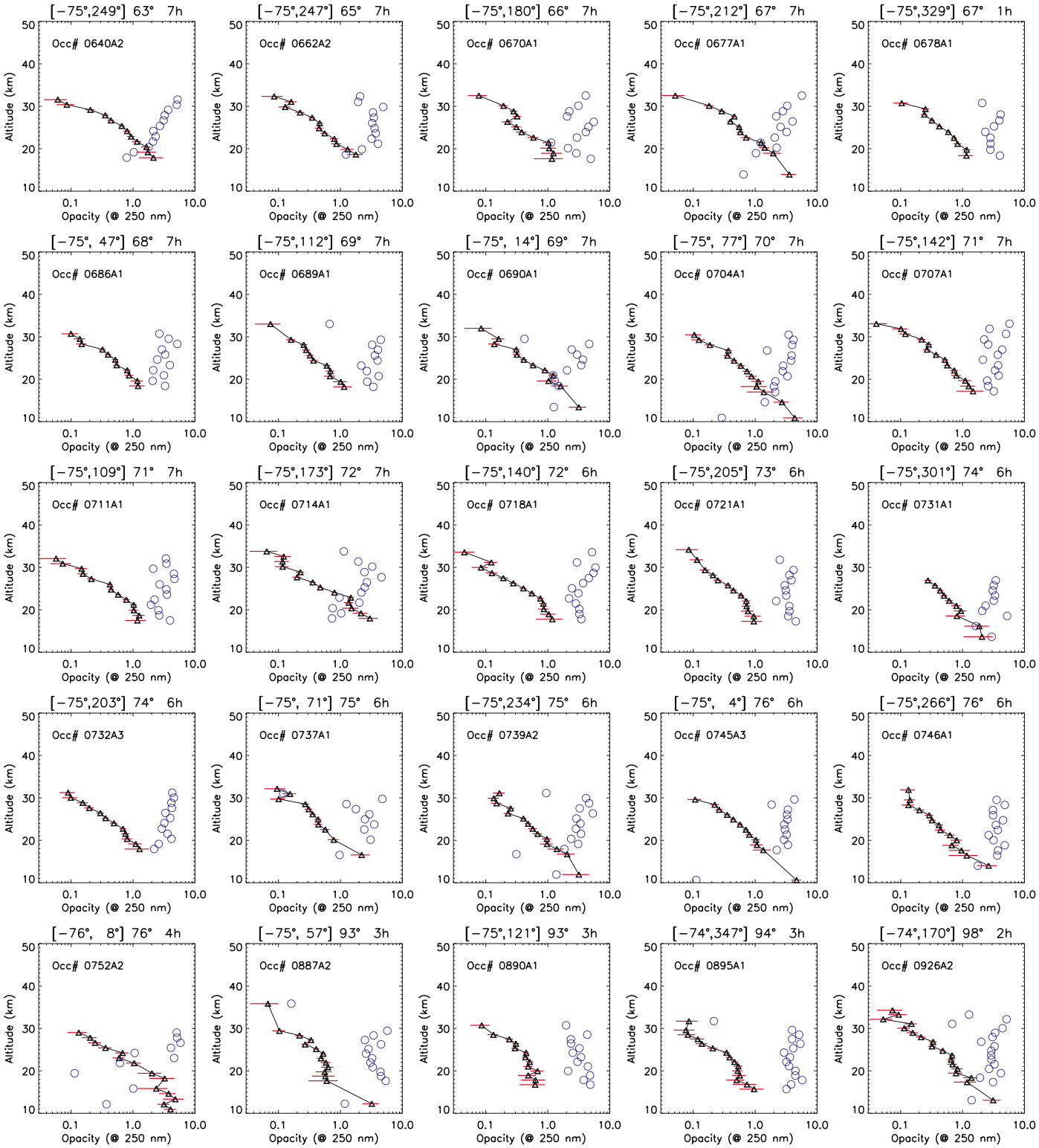

Fig. 51. A set of aerosol profiles retrieved from SPICAM stellar occultations in the southern hemisphere around the northern summer solstice. Solid lines show the aerosol opacity along the LOS as a function of altitude (red horizontal bars indicate measurement uncertainties). Blue circles give the value of the Angström coefficient α (opacity varies as $\lambda^{-\alpha}$; α is a parameter indicative of the particle size), on the same scale as opacity. Larger α means smaller particles. Values shown here suggest a particle size of <1 μm. The orbit number is at upper left; at top is the latitude and longitude of the occultation point and solar longitude L_s, and the local time. The atmosphere is clear above 30 km, which is rarely the case at other latitudes and seasons.

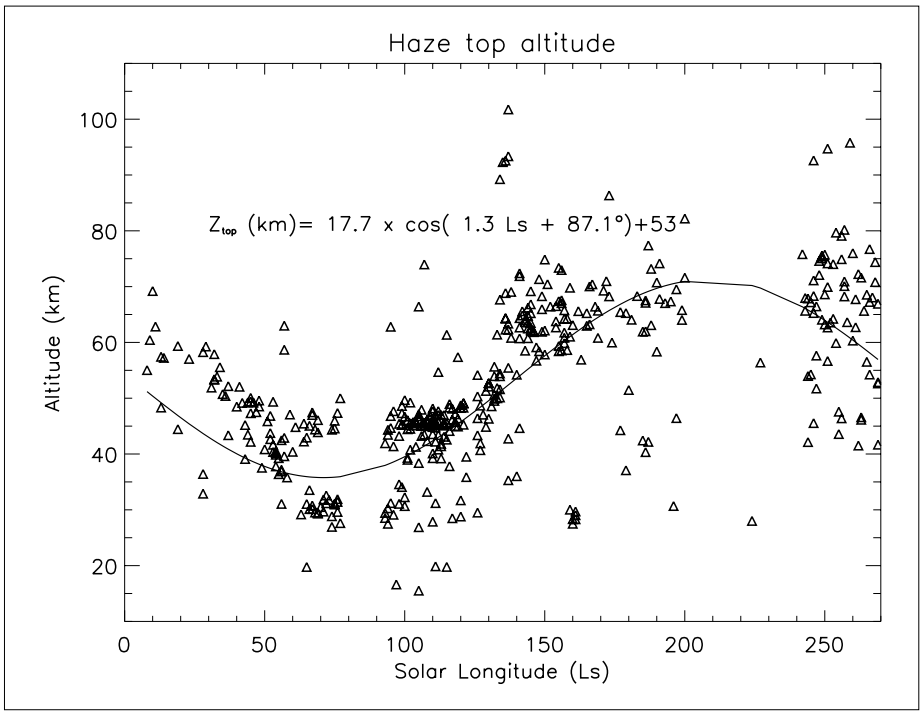

Fig. 52. Seasonal variation of the maximum elevation where particles can be detected by SPICAM in every stellar occultation profile.

presence of Aitken cores that can escape nucleation and thus scavenging by water-ice crystals. In any case, this information will be of great value for climate models, which are strongly sensitive to assumptions on the aerosol loading and vertical structure in these regions.

Also analysed was the seasonal evolution of the haze top (the maximum height at which particles can still be observable) as seen by SPICAM's stellar occultations. A strong seasonal signal is detected (Fig. 52), with the haze gradually losing altitude with deeper penetration into colder regions. This results from two distinct effects in combination: the stronger convection prevailing over sunlit terrain; the lower altitude of the hygropause following the cooling of air masses. With the second effect, the formation of water-ice clouds is favoured at lower altitudes, and the subsequent scavenging of dust particles above the hygropause results in the visible lowering of the whole haze layer.

6.4.4 Detection of cloud layers in the mesosphere

The notion that CO_2 clouds would appear frequently in the mesosphere was suggested by Mars Pathfinder images of the sky showing bright, blueish morning clouds possibly resulting from CO_2 condensation at high altitude. Until recently, however, no CO_2 condensate had ever been observed simultaneously with supercold temperatures (i.e. lower than the condensation temperature) . Indeed, SPICAM has detected the highest clouds ever recorded at Mars, at more than 100 km (Fig. 53). Simultaneous retrievals of aerosol and temperature profiles reveal very large portions of atmosphere where CO_2, the main gaseous compound, is supersaturated. This clearly suggests these mesospheric clouds are made of CO_2 ice.

These high-altitude clouds match the description of terrestrial noctilucent clouds (NLCs) that appear in the mesosphere of the polar regions. SPICAM's inferred UV opacities are typically very low (<0.01 when integrated vertically) and clouds would probably not be seen from the surface, unless perhaps just after sunset or before sunrise when cloud particles can scatter sunlight coming directly from below the horizon. Surprisingly, the observed clouds systematically stretch below the supercold

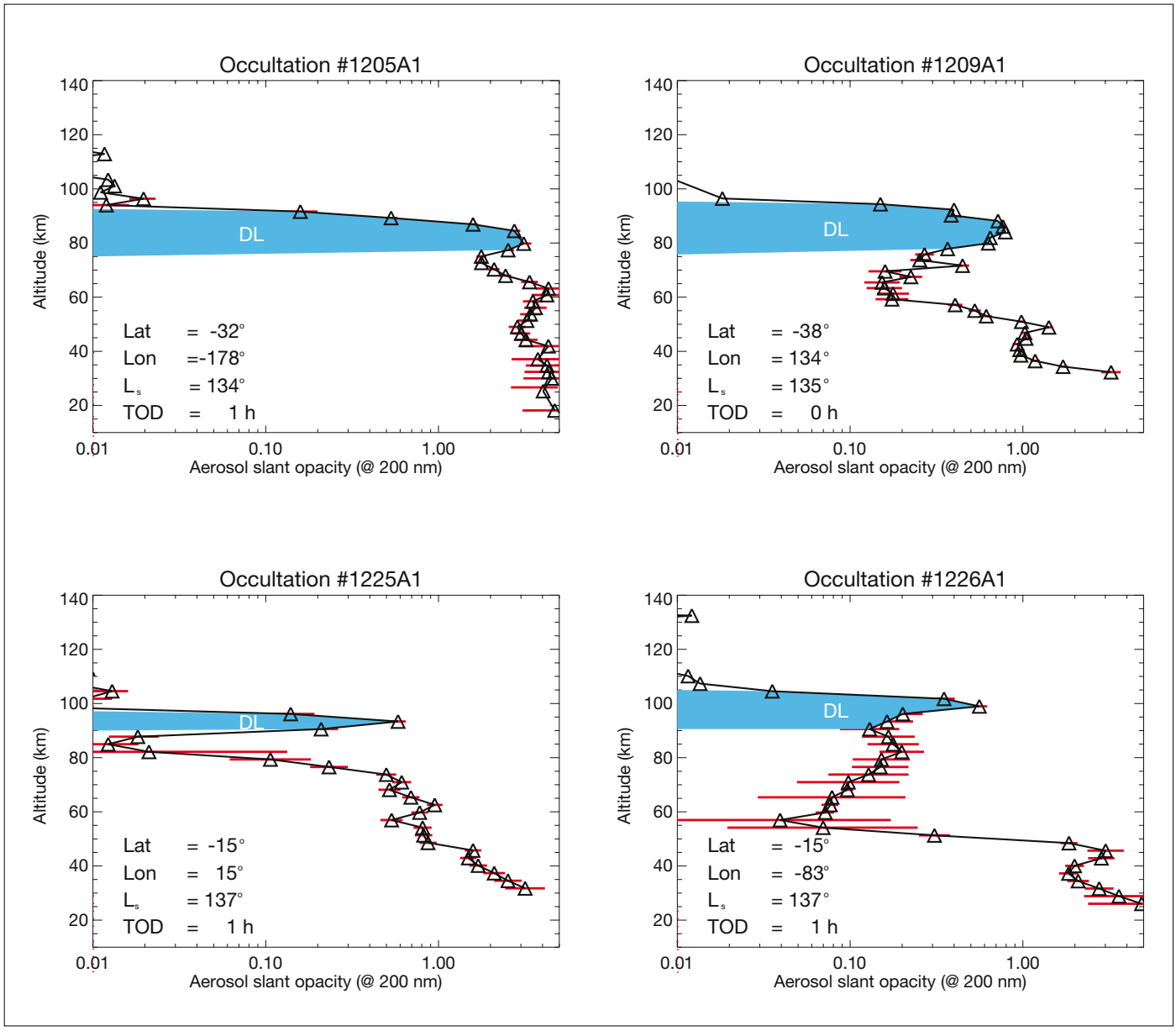

Fig. 53. Vertical profiles of the aerosol opacity along the LOS for four occultation sequences. Optical thickness is given at 200 nm. The vertical extent of the detached layer (DL) is shown for reference but observation geometry may stretch the image of the layer to altitudes well below its actual lower limit. Significant diurnal variations can be expected at high altitudes and clouds may disappear with daylight.

zone where they formed. A similar trend is observed for NLCs on Earth with respect to the saturation conditions of water vapour. It is, however, likely that CO_2 ice particles can fall significant distances into warmer, unsaturated air before their complete sublimation. In a rarefied atmosphere, condensation and sublimation processes are theoretically slower and must therefore compete with the short timescales of sedimentation. Using our estimates on cloud opacity and particle size, values for the cloud particle population can be derived – about a few million per cubic metre on average. Assuming CO_2 ice particles are formed heterogeneously, then a question emerges on the origin of the cloud condensation nuclei. Could they be supplied by a flux of meteoritic debris, as on Earth, or by an upward flux of submicron mineral dust particles stripped from the regolith? Vertical propagation of thermal waves appears

Table 5. Characteristics of the SPICAM near-IR channel (SIR).

Spectral range	1.0–1.7 µm
Spectral resolution	0.5 nm at 1.0 µm; 0.95 nm at 1.5 µm
FOV	1°
Telescope	Lens type, Ø 30 mm
AOTF	TeO_2, efficiency 70% (in polarised light), aperture 3.6 x 3.6 mm, ±3.5°
Detector	2 InGaAs PIN diodes (Hamamatsu G5832), Ø 1 mm
Transmission of optics	20%
NER	~5 x 10^{-9} W cm^{-2} sr^{-1}
Gain control	4 pre-chosen gain values
Number of spectral points	2 spectra with different polarisations, 332–3984 points each
Dynamic range	2^{16}, rounded to 2^{12}
Power consumption	5 W average
Dimensions	220 x 85 x 65 mm
Mass	700 g

only partly buffered by the release of latent heat induced by CO_2 condensation, as illustrated by the recurrent presence of supercold air pockets. As a result, the role played by microphysical processes, which control CO_2 ice particle formation and evolution, is critical in regulating the thermal state of the upper atmosphere.

7. The SPICAM AOTF Near-IR Channel

7.1 Technical Description

The near-IR channel works in the spectral range 1–1.7 µm with a resolving power superior to 1800. It is a lightweight (0.8 kg) extension of the UV channel that was added at late stage of the mission, partly in order to demonstrate the capability of the new acousto-optic tuneable filter (AOTF) technology in deep space. Its principal goal is to measure water vapour in the atmosphere, spectrally analysing solar radiation reflected from the surface and modified by atmospheric absorptions. This channel and its expected science return were described in Bertaux et al. (2004) and Korablev et al. (2002a); a more detailed description of the hardware is presented in Korablev et al. (2002b). This section summarises the in-flight performance and presents an overview of the main scientific results.

A single-pixel detector of InGaAs, associated with an AOTF, allows the measurement of the H_2O column at nadir with a very low-mass configuration. The AOTF device is based on the Bragg diffraction of an entrance beam by the ultrasonic acoustic wave excited within a crystal. It offers the potential to reach a resolving power, $\lambda/\Delta\lambda$, greater than 1000, which is ample to measure nadir H_2O by scanning the absorption line at 1.38 µm in the reflected solar spectrum. There are no moving parts, such as a chopper. This new concept in IR spectroscopy had never flown on a civil spacecraft but SPICAM has demonstrated its maturity for space research; it should have a great future.

The spectrometer is included alongside the SUV (see Fig. 4); its optical scheme is shown in Fig. 2 and its main characteristics are summarised in Table 5. A 30 mm diameter lens telescope has a focal ratio of 1/1.9. A 1 mm diameter circular diaphragm

in the focal plane defines the FOV. A collimator with two small lenses forms a beam into a custom-made TeO_2 AOTF crystal with an active zone of 23 mm. The divergence of the beams inside the crystal is neatly limited to 5.5°. The linear aperture has its minimal pupil of 3.12 mm in the centre of the crystal and is less than 3.5 mm at the edges. The output system separates the beams for different polarisations; the first lens compensates for the divergence of the output beam, and the second lens focuses the light at the detector. There are two detectors and two short-focus proximity lenses, one for the ordinary beam, and another for the extraordinary beam, allowing measurement of the polarisation of the incoming light with high accuracy (Glenar et al., 1994). Polarimetry measurements should enable characterisation of the properties of the atmospheric aerosol component (Santer et al., 1985).

The channel uses solar entry parallel to that of SPICAM UV, at 90° to the main axis +*Z*. An optical fibre delivers the solar light to the objective; its entry optics provide an angular FOV of about 4 arcmin. A collimator lens at the output of the fibre and a 45° flat mirror mounted on the objective's baffle complete the design (Fig. 54).

The AOTF uses a TeO_2 crystal in the non-collinear configuration. It produces two polarisations of the diffracted light. The acoustic wave is excited by a piezoelectric actuator, with a voltage varying at high frequency (~100 MHz), creating a pattern similar to that of a Bragg crystal. The diffracted beams are deflected at a small angle with respect to the undiffracted, 'white' output beams. If the acoustic wave is not applied to the crystal, there are only two undiffracted beams, and as soon as the acoustic wave is turned on, two diffracted beams appear. These two weak beams must be well separated from one another and from the strong undiffracted beams, which contain most of the spectrum.

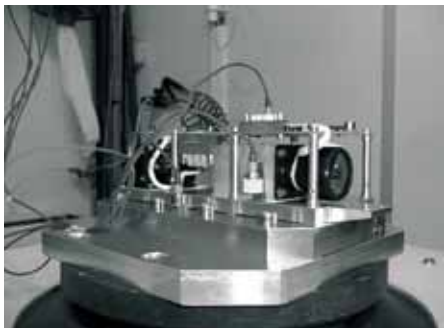

Fig. 54. The full IR channel of SPICAM on the vibration test bench. The entrance lens is at right and the detectors at left.

7.2 Operations and In-flight Performance

The IR channel has operated from the beginning together with the UV channel. The principal observation configuration is nadir, and at first the channel was not operated during stellar occultation (the faint IR signal is far below the detection capability). However, the channel was left on during most SPICAM UV operations in order to characterise the background signal better, and to avoid missing interesting limb observations. Up to March 2005 the SIR had performed 826 observations, including 447 nadir, 94 limb and 285 solar occultation sequences.

Owing to the nature of the AOTF sequential measurements from an orbiting spacecraft, each measured spectral point generally corresponds to a different spot on the surface. The FOV of 1° corresponds to ~5 km from the pericentre altitude of 250 km, so it is desirable to restrain the overall duration of the measurement of the whole spectrum to 5–10 s. However, the full scan of the spectral range at fine spectral sampling (3–4 points per element of the AOTF spectral resolution) requires 3984 points, and the reasonable integration time of 5.6 ms leads to 24-s measurements. Since the frequency of ultrasonic excitation of the AOTF is controlled by software, it can be randomly tuned to any wavelength within the spectral range, allowing us to optimise the measurement time without compromising the science return. This spectrometer can be programmed to scan up to three windows, and to determine for each one the bounds and spectral sampling. Furthermore, several sets of predefined 'dots' are available to characterise the spectral continuum (surface albedo, reflectance at limb, extinction, etc.). During the first orbits, AOTF's full range was used to acquire full spectra at maximum sampling, at the expense of longer sampling intervals. Then, after initial analysis, the spectra were restricted to the most interesting parts, by defining the parameters of the optimised window-dot sets for different observation modes (Fig. 55). Also, parameters such as gain and AOTF power were optimised. As a result, one spectrum per second was obtained in most cases.

The in-flight performance of the spectrometer does not differ substantially from what was expected after ground testing and calibration. The notable exceptions are a slight modification of the instrument background and measurements in the solar occultation mode.

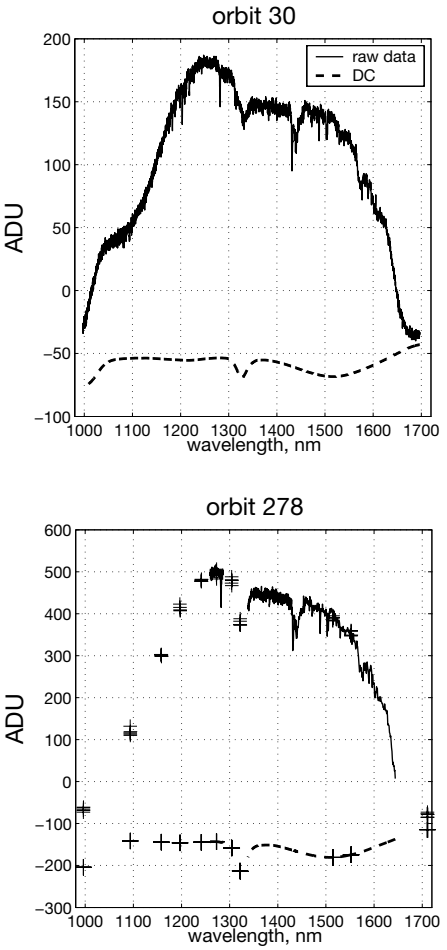

Fig. 55. An illustration of SIR operation modes. Top: a 'full spectrum', with the AOTF driving frequency spanning the entire range and the filter is sequentially tuned to all wavelengths 1–1.7 μm. With fine sampling, such a sequence requires several seconds (12–24 s, depending on integration time etc.). Bottom: optimised sequence, in which only the interesting portions ('windows') of the spectrum are scanned at maximal sampling; less important ones have reduced sampling, and the rest of the spectrum is characterised by only a few continuum points ('dots').

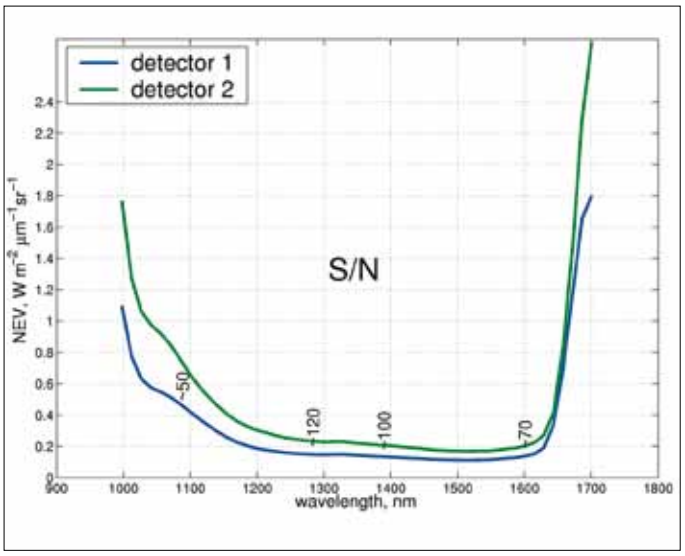

Fig. 56. Noise equivalent brightness of the SIR at 1–1.7 µm. Approximate signal-to-noise values for the sunlight reflected from the surface of Mars are indicated near the curve of detector 1, for a 6 ms sampling time.

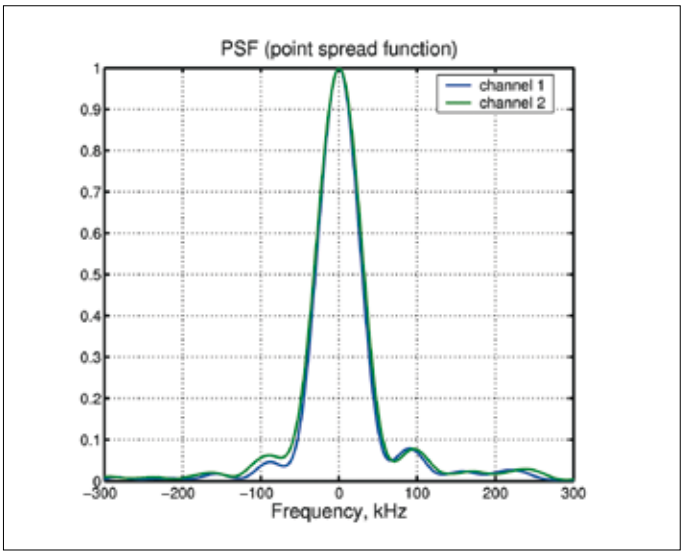

Fig. 57. Measured shape of the spectral instrument function as a function of frequency for two channels.

The spectrometer's measurements (Korablev et al., 2002b) are based on digital synchronous detection, when the dark current is subtracted from the useful signal. Therefore, theoretically the background signal is zero, except if there is a synchronised optical or electrical interference. While the former is unlikely, the latter comes from the radio-frequency (RF) driver of the AOTF itself. This kind of interference depends on RF frequency and power, and forms a characteristic pattern as a function of wavelength. This pattern, well characterised on the ground, changed after launch, with a bump added around 1.35 µm. Also noticed was a slight modification of the background in each observation mode due, most likely, to a modified thermal regime. A special effort was therefore made to characterise the background behaviour in flight. It should be noted that even the initial uncertainties were small, not affecting the derivation of robust quantities, such as water vapour content, and our current knowledge of the background allows comparison of absolute spectra that differ by less than 1–2%, which is necessary for polarisation studies.

Solar occultations were achieved after a number of attempts to direct the 'solar' axis of SPICAM to the Sun. The task was even more complicated than in the UV because of the smaller FOV and the lack of an imaging detector. Unlike on the ground, the spectra recorded via the solar entrance reveal some quasi-periodic fringes with an amplitude comparable or larger than the depth of the expected H_2O absorption features, possibly generated in the fibre's entrance optics. Moreover, the fringes are subject to modification during occultation, possibly because of a rapid change in temperature. In spite of these difficulties, the IR occultation data have been used to obtain vertical profiles of water vapour and aerosol extinction.

The ground calibration data and the flight data were reanalysed and an updated calibration database is available. The accuracy of ground data on the absolute sensitivity of the SIR was low; the absolute calibration in flight is done by comparison with OMEGA spectra for a few orbits with relatively homogeneous surface albedos.

The noise-equivalent brightness of a sampling of 6 ms is presented in Fig. 56, while the spectral response to monochromatic light (provided by a laser diode) is shown in Fig. 57.

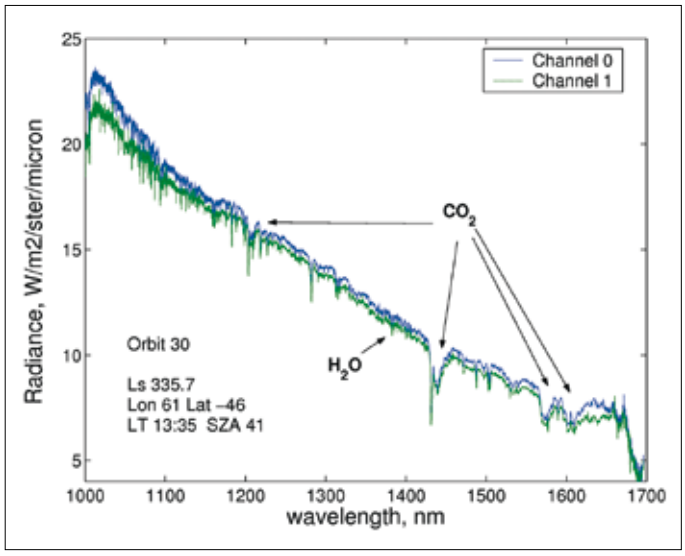

Fig. 58. An example of calibrated SIR spectra for orbit 30. Individual spectra for two different polarisations are shown.

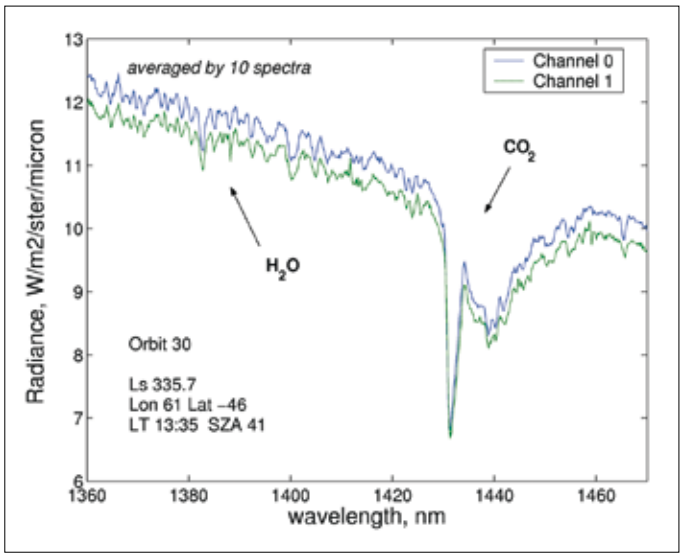

Fig. 59. A portion of the spectrum from Fig. 59, showing the vicinity of the H_2O absorption band at 1.38 μm, and the adjacent CO_2 band at 1.43 μm. For clarity with the complicated H_2O band, 10 consecutive spectra of orbit 30 are averaged together.

7.3 Water Vapour Measurements

Typical calibrated spectra measured by the SIR in nadir geometry for the early orbit 30 are presented in Fig. 58. The main features are the spectral slope towards longer wavelengths due to the solar spectrum, a large number of Fraunhofer lines, and some atmospheric absorption features, the most prominent being the CO_2 absorption bands at 1.43, 1.58 and 1.6 μm, and the H_2O absorption band around 1.38 μm (Fig. 59), which is the very band that was used on Viking-1/2 by the MAWD experiment (Farmer & LaPorte, 1972), which established the first H_2O season–latitude climatology.

The latter band was used for the routine retrieval of the total column water vapour abundance in the atmosphere. In the retrieval, an average of 6–10 spectra are generally used. Retrieval is made by a best fit of the observed spectrum by a direct model synthetic spectrum, computed line-by-line using the spectroscopic HITRAN-2000 database (Rothman et al., 2003). Atmospheric parameters are taken from either the European Martian Climate Database (Forget et al., 1999) or the NOAA Geophysical Fluid Dynamics Laboratory (GFDL) database (Richardson & Wilson, 2002). Water vertical distribution in the atmosphere is assumed to be uniformly mixed up to the saturation level (defined by the model temperature profile) and limited by the saturation above. Surface pressure and the air mass are calculated from the MGS/MOLA topography (Smith et al., 2001).

An important issue is an accurate solar spectrum, because numerous solar lines frequently mix with the signatures of the martian atmospheric gases. There are few sources of high-resolution solar spectra in the range of interest, so, for the time being, the spectrum by Kurucz (1995) is being used, although its spectral resolution (sampled at 1 cm^{-1}) is at the limit of what is required. In the future, the spectrum compiled from PFS data may be used (Fiorenza & Formisano, 2005).

Examples of synthetic fits to the SIR measurements are presented in Fig. 60. A synthetic spectrum is fitted to the data across 1355–1420 nm; the retrieved quantities are water vapour total column amount in precipitable microns, and the modification of the solar spectrum due to non-gaseous extinction and the reflectivity of the surface. Folded with the Sun's spectrum, this function is denoted as Sun multiplied by albedo in Fig. 60. The number of spectral points used in the fitting procedure depends on the

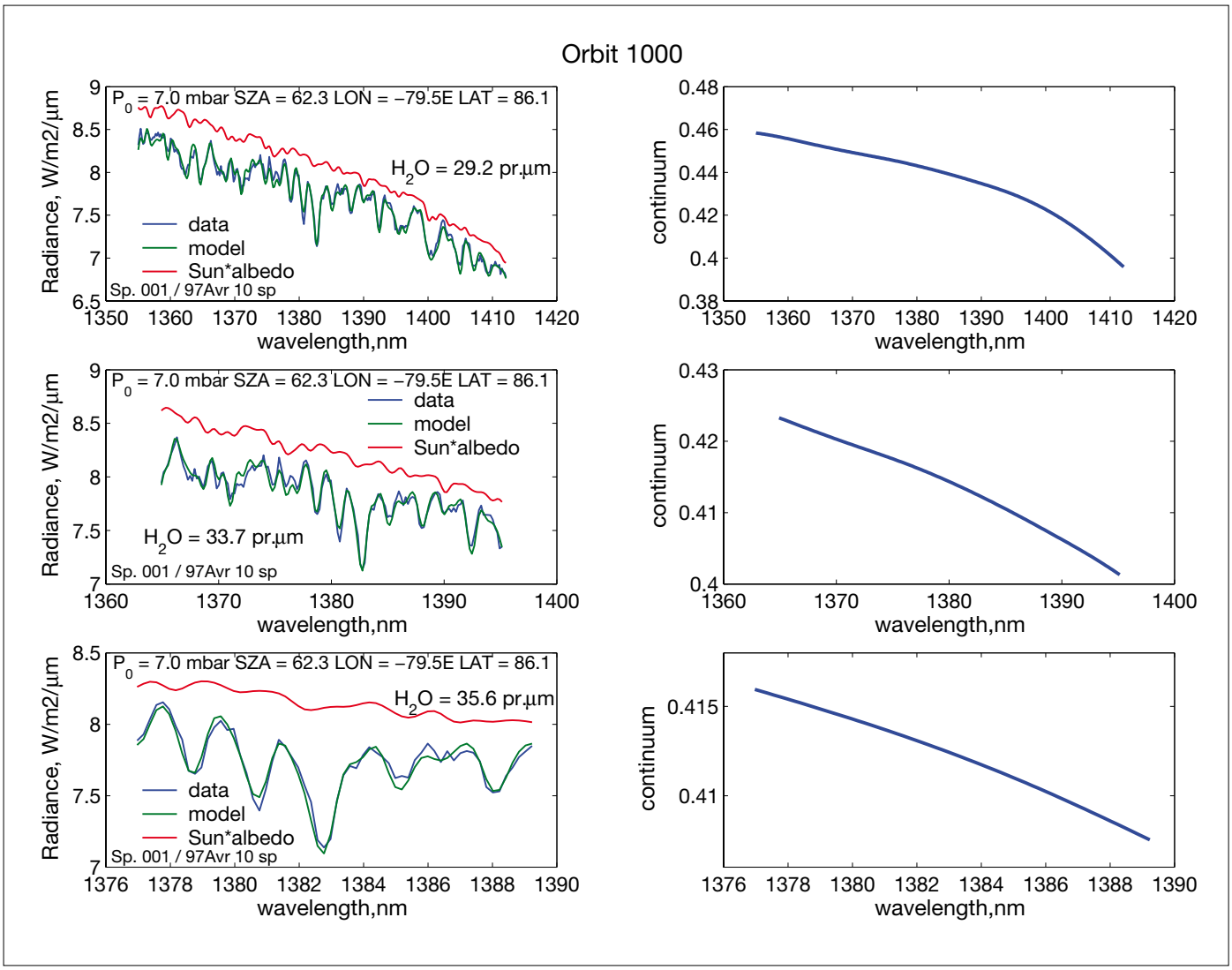

Fig. 60. Examples of fits to the SIR data in the H_2O absorption band at 1.38 µm. The same average spectrum for nadir orbit 1000 is fitted for different spectral ranges (from top to bottom): 1355–1412 nm, 1365–1395 nm and 1377–1389 nm. Blue curves: SIR calibrated data; green curves: synthetic fit; red curves: the solar spectrum modified by surface albedo (a wide H_2O ice band causes additional absorption longward of 1420 nm) and possible continuum atmospheric extinction.

SIR observation mode, and for a typical nadir orbit amounts to 170. The generally very good quality of the fit can be seen in Fig. 60.

Atmospheric aerosols for near-IR retrieval of H_2O are presently not taken into account, due mainly to the lack of dependable simultaneous measurements of dust and aerosol optical depths. Such measurements are possible using PFS and OMEGA data: at the bottom of the 2.7 µm band, or the dust opacity in the silicate 9 µm band, which is a by-product of thermal retrievals by PFS. The aim is to implement this synergy in the future. There is also a marginal possibility of estimating the aerosol contents fitting the shape of the 1.43 µm CO_2 band using SIR data. However, this problem is rather poorly constrained and the solution is not straightforward.

Figure 61 compares the water vapour profiles measured by SIR along two orbits with the two GCM predictions (Richardson & Wilson, 2002; Montmessin et al., 2004). The SIR measurements are smaller than the model results by a factor of 2–3, except for the north polar region, where there is also substantial disagreement between the two models. Model results depend on many factors, so no conclusions are drawn here, leaving the discussion for a paper dedicated to H_2O measurements.

A comparison of the different measurements reveals substantial discrepancies. Mars Express carries three instruments capable of measuring water vapour in the near-IR to thermal–IR spectral ranges. Modern climatology of Mars atmospheric

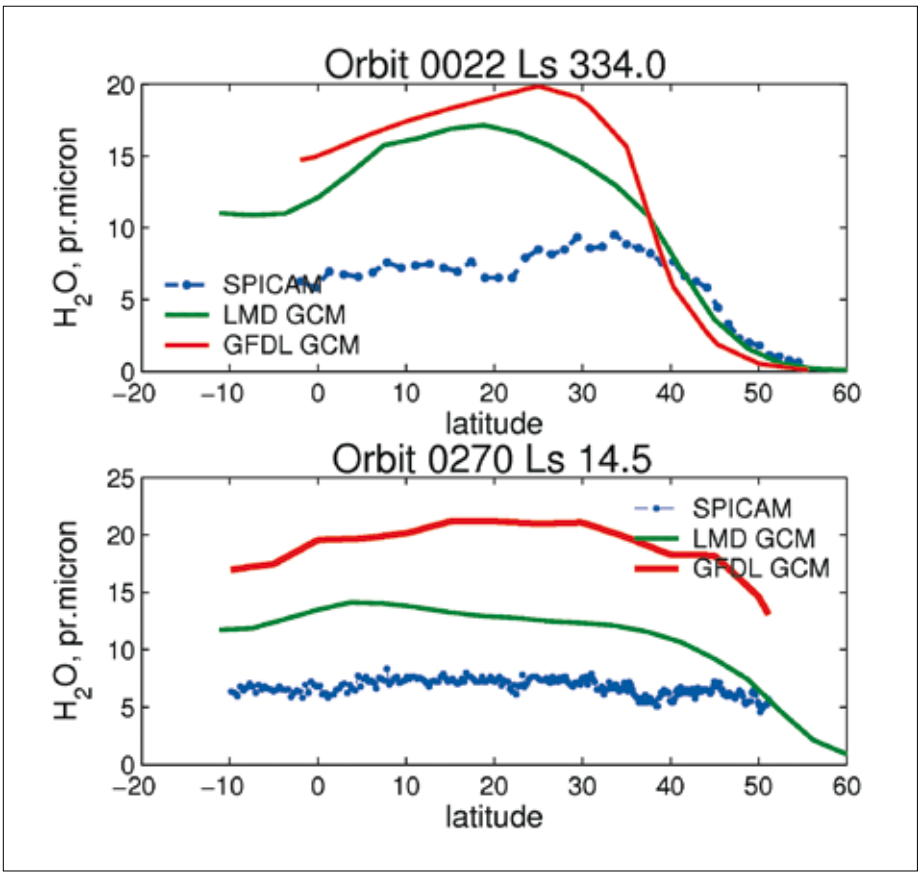

Fig. 61. Two SIR water vapour latitude profiles for different seasons (L_s = 334° and 14.5°) compared with predictions from LMD and GFDL GCMs. The noise and fluctuations of the SIR data are small. The overall variation is well captured by SIR at high latitude (L_s = 334°), but the level is generally lower than predicted by the models, which in fact give different predictions.

water is based on MGS/TES, with measurements performed in the thermal spectral range for three full martian years (Smith, 2004). Good knowledge of the temperature profile is required for the retrieval, and there is some evidence that TES sometimes overestimates water abundance. The data taken in the near-IR are sensitive to the aerosol content, and are sometimes underestimated (Fedorova et al., 2004). There are physical reasons to have different values at different wavelengths: vertical distribution (H_2O vertical mixing ratio is non-constant) and scattering by aerosols. Some comparisons of the data have shown substantial disagreements between the datasets, even within PFS measurements, and also between SPICAM, PFS (near-IR) and OMEGA. SPICAM's H_2O amount was a lower limit for all other observations. The comparison of water-vapour datasets, including from Mars Express, MGS and ground-based measurements, to resolve the discrepancies has been the focus of a dedicated team working at the International Space Science Institute (ISSI, Bern, CH) since November 2005. Mars Express should build its own H_2O climatology model; the contribution of SIR to this database is essential.

It should be noted that, following an ISSI workshop on Atmospheric Water Vapour, Smith (2004) found an anomaly in the TES/MGS retrieval, which, when corrected, yielded lower H_2O values by up to 25%, alleviating the discrepancies somewhat. Still, the amount of water vapour measured by SPICAM appears to be a lower limit for all other observations. Why is it so small? In the present analysis the effects of multiple scattering by dust are not taken into the account. It might be a possible explanation, but as shown by Fedorova et al. (2004) for an air mass factor <3, which is the case for nearly all Mars Express nadir observations, the effect of dust impact on the near-IR spectra does not exceed 20–30%. This is supported by the generally good agreement among PFS thermal–IR measurements, which are supposedly not affected by aerosols, and SPICAM data.

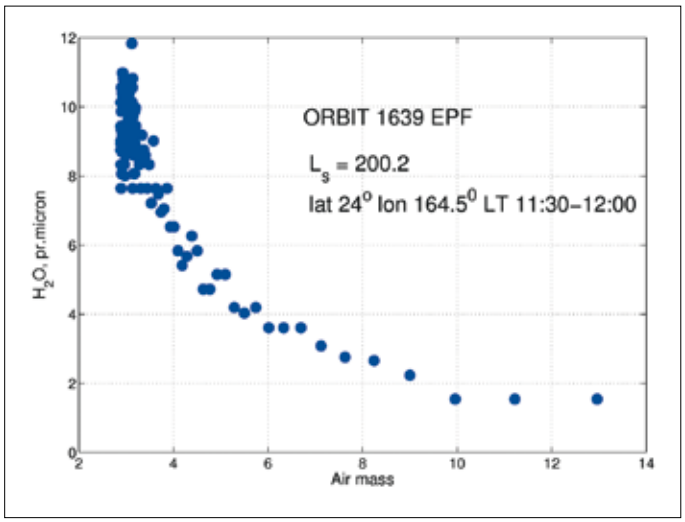

Fig. 62. Retrieved water vapour content (total vertical in precipitable microns) from EPF observations during orbit 1649, plotted as a function of the air mass. It should be constant, but there is a decrease in the retrieved amount. This is the effect of dust, which was not accounted for in the fitting model.

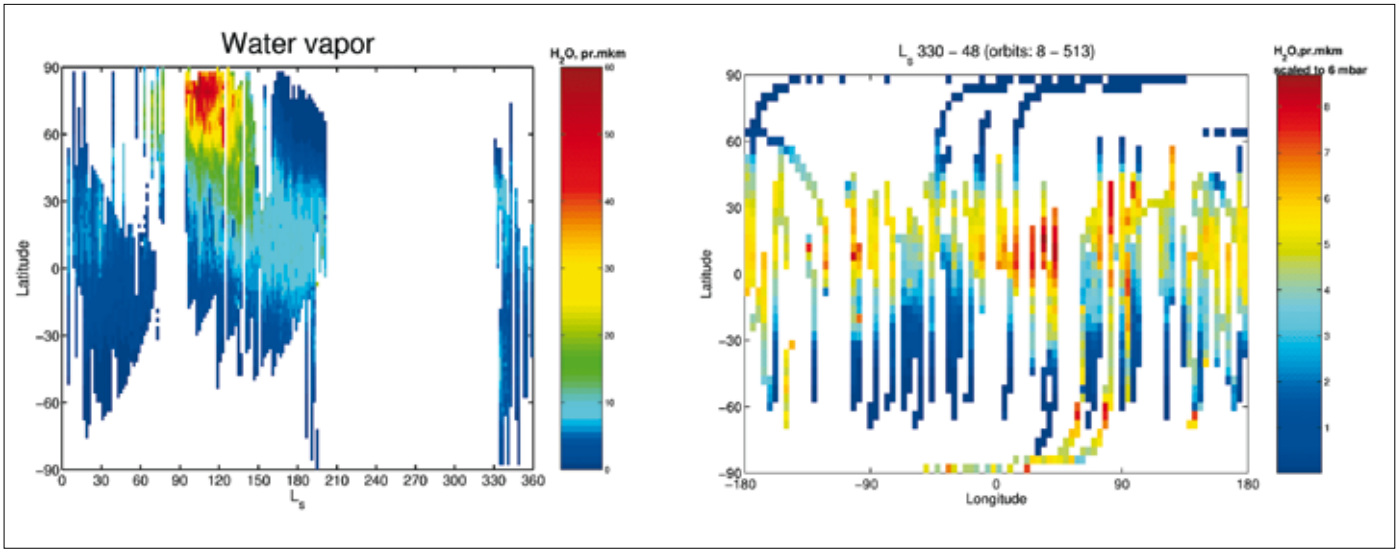

Fig. 63. *Left*: seasonal distribution of water vapour measured by SIR (orbits 8–1640) in units of precipitable microns. *Right*: geographical distribution of water during northern spring (L_s = 330–48°, orbits 8–513). All the data are scaled to a constant pressure of 6 mbar, assuming a mixing constant with altitude, in order to emphasise the geographical distribution. Some areas seem to be more humid than others.

The effect of dust/aerosols is twofold. On the one hand, some light is scattered backwards by dust before reaching the ground, decreasing the effective air mass factor. On the other hand, multiple scattering tends to increase the effective air mass factor. For the time being, these two effects are assumed to more or less compensate for each other.

A good illustration of the impact of dust on H_2O retrieval is given by emission phase function (EPF) measurements performed by Mars Express at a few locations and times. The EPF observations are intended to study the photometric and spectral behaviour of the surface, and the atmospheric aerosols by observing a given location on Mars at various phase angles. For orbit 1639, the standard routine was used to retrieve the amount of water vapour, and a strong dependence on the phase angle was found (Fig. 62). This could be interpreted as the influence of aerosols on the depth of the H_2O band. Clearly, for an air mass exceeding 3–3.5, the aerosol effect is dominant and should not be neglected. A typical air mass for nadir observationa is 2.5–4, so SPICAM data are guaranteed against large underestimates of the amount of H_2O, but the influence of aerosols should be taken in account in some cases.

The maps of seasonal and geographical distribution of water vapour measured by SIR are presented in Fig. 63.

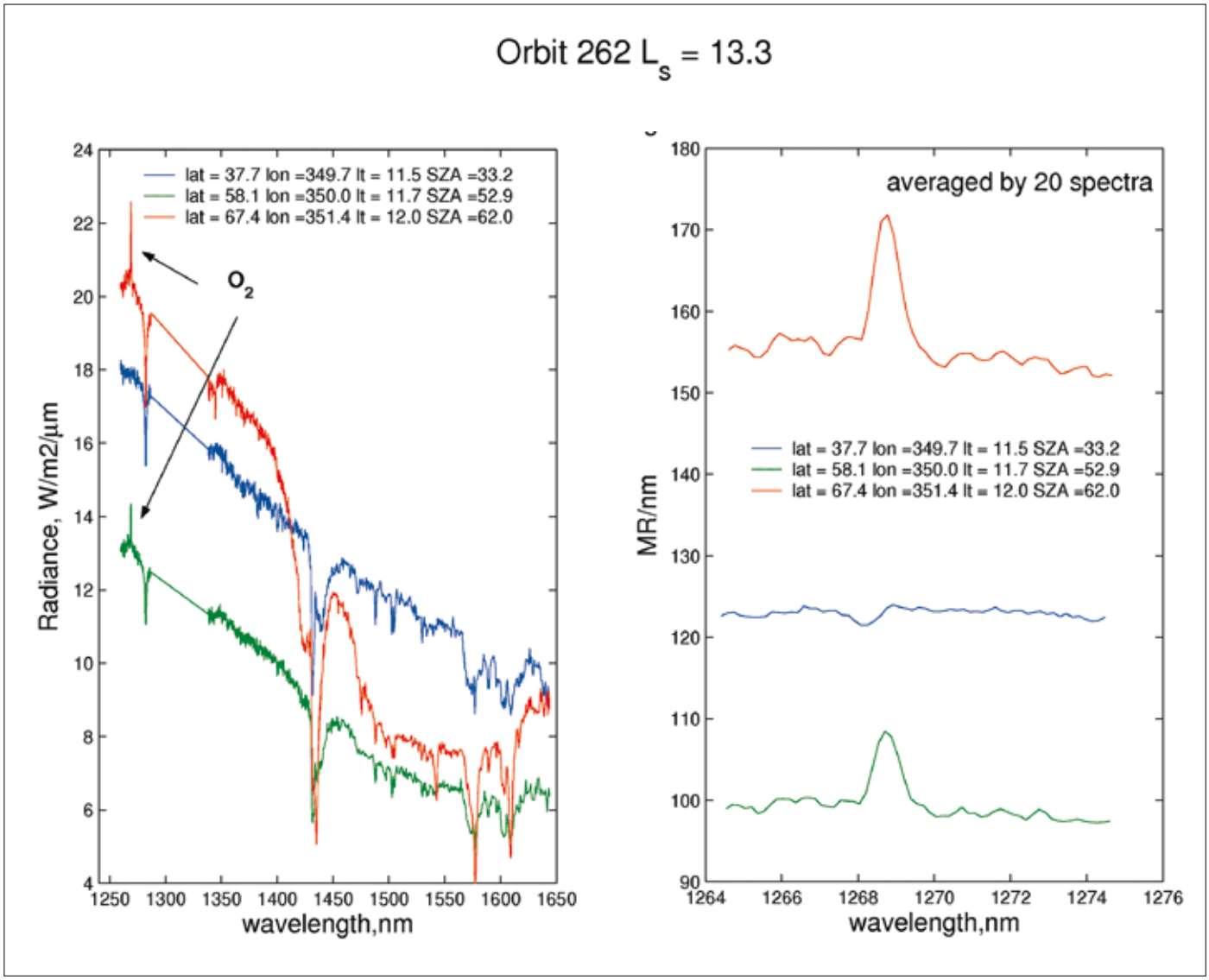

7.4 Oxygen O2($^1\Delta_g$) Emission at 1.27 µm

A dayglow 1.27 µm $O_2(^1\Delta_g)$ emission was predicted soon after the discovery of ozone on Mars by Mariner-9 (Barth & Hord, 1971). The situation is similar on Earth, where a strong airglow arises from $O_2(^1\Delta_g)$ production from ozone photolysis. This emission was first observed on Mars from the ground at high spectral resolution by Noxon et al. (1976). Latitude correlation of O_2 emission with Mariner-9 O_3 was reported by Traub et al. (1979). The mapping of this emission was reported by Krasnopolsky & Bjoracker (2000). Krasnopolsky (1997) argues that the O_2 emission provides even better insight into photochemistry than the total ozone, since it is more sensitive to the variations of the water vapour saturation level (10–35 km) than total ozone. At low altitudes, this O_2 emission is totally or partially quenched by collisions with CO_2 molecules; this emission is therefore probing altitudes above 20 km.

The band intensity observed by different authors from the ground varies from 1.5 MR to 26 MR and, indeed, SPICAM IR routinely observes the $O_2(^1\Delta_g)$ band at nadir and the limb of Mars mostly in the polar regions. Three spectra recorded along one orbit at different latitudes (Fig. 64) are different: the albedo, the shape of the spectrum, and the shape of CO_2 absorption lines of spectrum 3 differ from those of

Fig. 64. Three spectra measured by SIR along orbit 262 for latitudes of 38°N (blue: 1), 58°N (green: 2) and 67°N (red: 3). The right panel enlarges the spectral region of the 1.27 µm $O_2(^1\Delta_g)$ emission band. Spectrum 3 also contains a broad signature of H_2O ice longward of 1420 nm. In the left panel, an enlargement of the spectra over 8 nm illustrates the high variability of 1.27 µm $O_2(^1\Delta_g)$ in a single orbit.

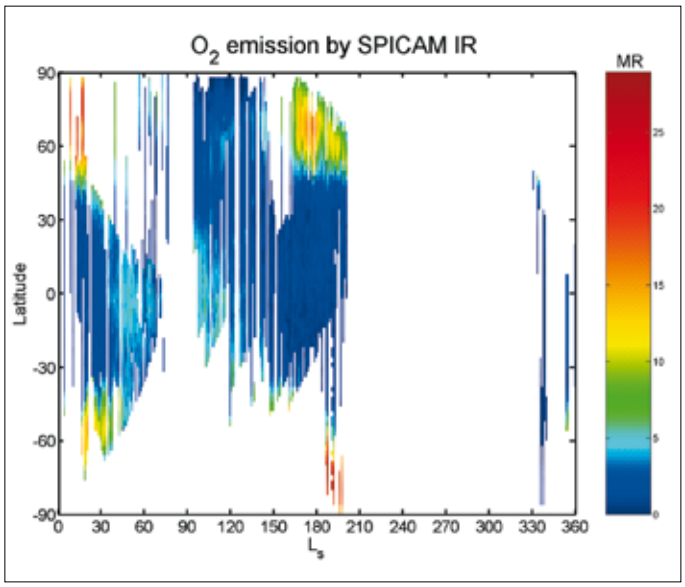

Fig. 65. Seasonal distribution of the $O_2(^1\Delta_g)$ emission in Mars' atmosphere. The colour code is in MR. This map can be compared with that showing UV-retrieved ozone in Fig. 25.

1 and 2 (see below), and an emission feature near 1.27 μm is apparent in spectra 2 and 3. This region, enlarged in the right panel of Fig. 64, reveals a clear signature of the $O_2(^1\Delta_g)$ band. A detailed discussion of the $O_2(^1\Delta_g)$ issue related to ozone in the atmosphere is presented in Federova et al. (2008). Here, a seasonal map of this emission is presented (Fig. 65).

7.5 Other Products from SIR Nadir Spectra

With the help of the synthetic model described above, and with the known solar spectrum, the reflectance of the apparent martian surface free from gaseous atmospheric absorptions can be derived (lower panel of Fig. 66). It cannot be claimed that this is the surface albedo, because some contribution can be due to atmospheric aerosols. The resulting spectrum has several distinct features: a broad absorption longward of 1450 nm attributable to water-ice, and a number of narrow absorptions, some of them coinciding with gaseous CO_2 absorption bands but with distinctly different shapes, attributable to CO_2 ice. The weak emission near 1270 nm is not the atmospheric $O_2(^1\Delta_g)$ emission, but the uncompensated neighbouring solar line, apparent in emission because of the imperfect model solar spectrum. The same features are visible in the spectrum recorded in the north polar region (curve 3 in Fig. 64).

In conclusion, the SPICAM IR AOTF channel has proved to be capable of measuring the following quantities on Mars in nadir observations: water vapour content, oxygen emission due to UV photo-dissociation of ozone, CO_2 and H_2O ice, and surface albedo (Fig. 67). These quantities have been retrieved systematically for all recorded nadir data for future synoptic analysis, and comparison with other instrument findings.

7.6 Solar Occultation

SPICAM's unique features are the stellar and solar occultation modes. The IR sensitivity is insufficient for stellar occultations, which are performed in the UV, while solar occultations are observed simultaneously in the UV and IR. Solar occultations in the IR should deliver information about aerosol vertical distribution, water vapour and CO_2 distribution. These measurements are also potentially sensitive to CO_2 ice and H_2O ice features in the atmosphere.

Solar occultations were achieved after a number of attempts to direct the 'solar' axis of SPICAM towards the Sun. At the beginning of the mission, the recorded solar spectra did not allow the retrieval of water vapour vertical profiles. The reason proved

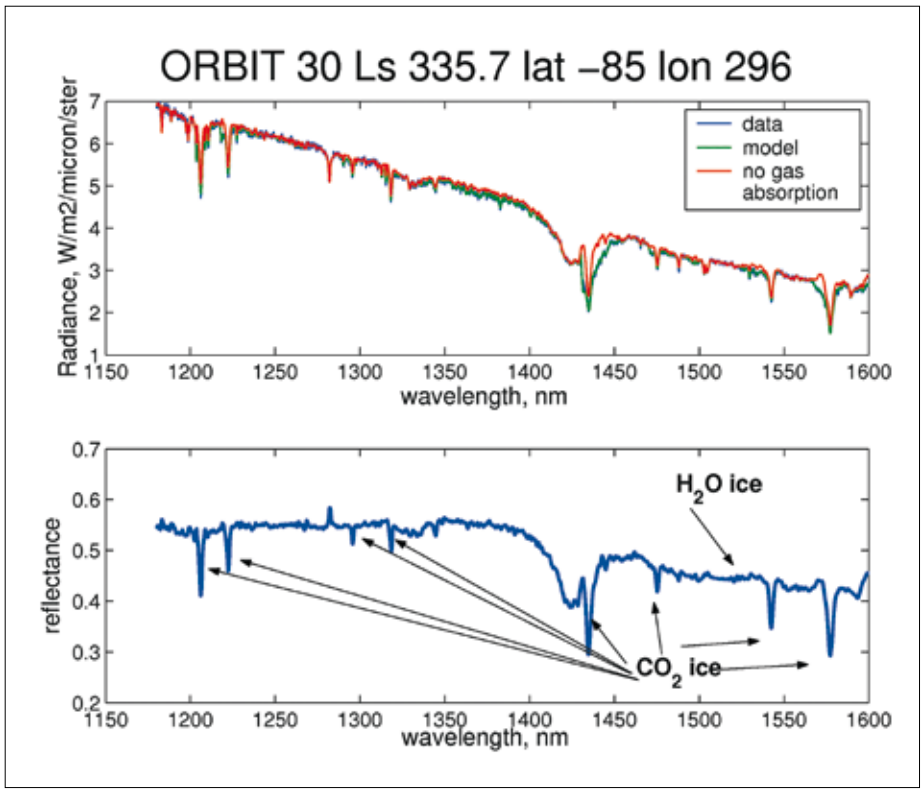

Fig. 66. Upper panel: SIR spectrum recorded during orbit 30 (L_s = 335.7°) at 85°S. Blue is the measured spectrum, green is the synthetic fit, red is the non-gaseous spectrum of Mars, needed to fit synthetic gaseous transmittance to the measured spectrum. The green curve is the product of the synthetic model with the non-gaseous spectrum. The non-gaseous albedo is plotted as reflectance in the lower panel.

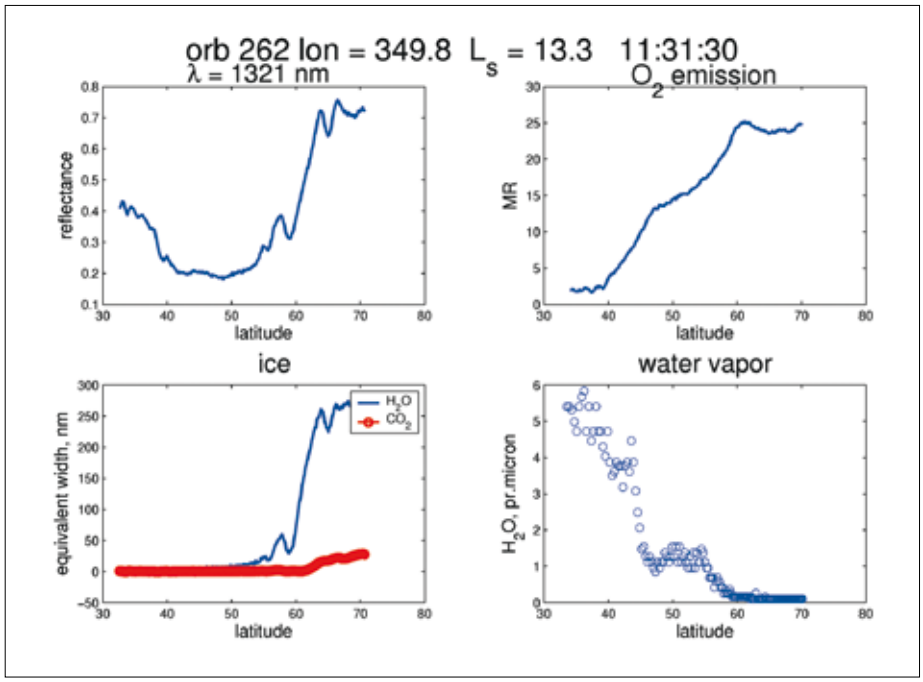

Fig. 67. Products of SIR in nadir observations: surface albedo at 1320 nm (example wavelength), the intensity of $O_2(^1\Delta_g)$ emission due to photo-dissociation of ozone, the equivalent width of carbon dioxide and water ice (on the surface or in aerosol layers), and water vapour total column amount.

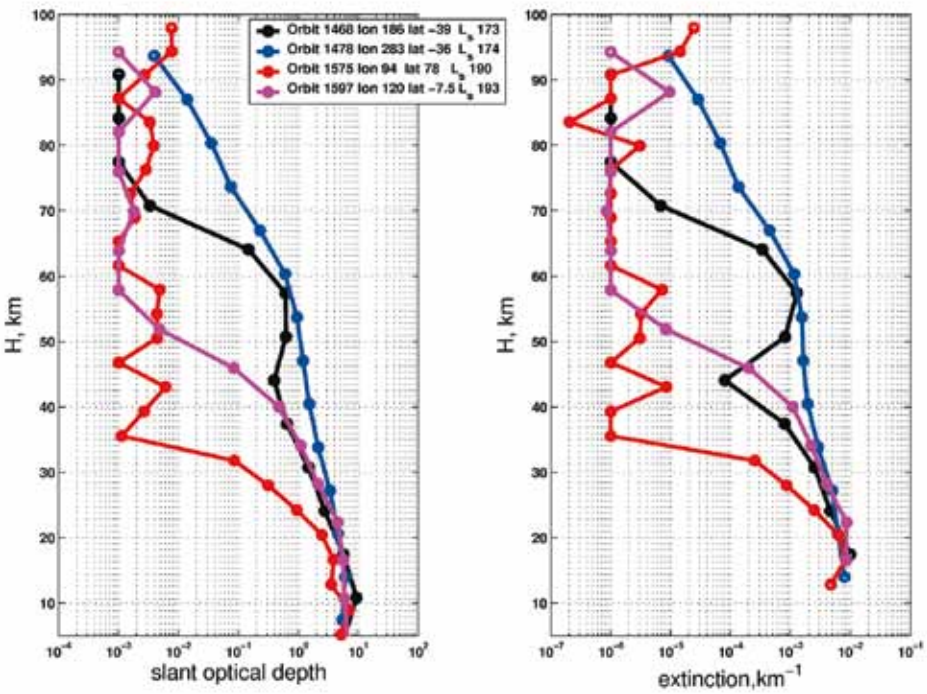

Fig. 68. Slant optical depth and extinction profiles obtained by SIR. The optical depth is taken at wavelength 1274 nm. The lower north polar profile stands out against the large extension of dust observed at mid-latitudes in the southern hemisphere.

to be that the data were obtained at L_s = 140–227° during a period when there were large quantities of dust in the atmosphere. The vertical extent of dust during this season has never been measured on any Mars mission, and appears to be as high as 50–70 km, except in the north polar area, where the expected water content is low. Typically, the slant optical opacity reaches unity at 35–50 km, and the low signal-to-noise ratio at lower altitudes prevents measurement of water vapour concentrated beneath the aerosols and dust. However, later in the mission, H_2O vertical profiles were successfully obtained many times, opening a new window on H_2O climatology on Mars.

Solar occultations give direct information about opacity in the LOS. The quality of IR photometry is good, and the vertical profiles of aerosol extinction have been retrieved for all solar occultation sequences, along with the spectral behaviour of the aerosol in the range 1–1.65 μm. Vertical extinctions were obtained with a latitude coverage ranging from high latitudes in the south hemisphere to one north polar profile. Figure 68 presents examples of a few extinction profiles for different locations on Mars. These new observations of vertical profiles of H_2O and aerosols are presented in Fedorova et al. (2008).

8. Conclusions

Several of the measurements provided by SPICAM are unique; examples are listed below:

— The (unexpected, but hoped for) discovery of two types of nightglow: aurora and NO emission, providing insights into magnetic field and upper atmosphere circulation.
— Ozone measurements are not included in any other current or planned missions. SPICAM has collected the first climatology data on ozone (both total and vertical distribution) using stellar occultations on the nightside. It is also the first time that ozone has been detected from orbit via $O_2(^1\Delta_g)$ at 1.27 μm (dayside). The first step to compare the data with a sophisticated model has been completed: the gross features of the ozone field are well-captured by the model. Remaining discrepancies are now also understood, with the role of H_2O_2 (a scavenger of

ozone) destruction on water-ice grains in the clouds or on the ground (Lefèvre et al., 2008). Once the model is tuned to reproduce the data (validated), it will offer the extraordinary possibility to calculate with confidence a large number of other species that are difficult (H_2O_2) or impossible to measure directly (i.e. HO_x radicals), for a full description of the martian environment. This is important for studies to assess the sustainability of life and human exploration.

— The density/temperature profiles obtained with SPICAM provide important constraints for building meteorological and dynamical atmospheric models, from the surface to the troposphere. SPICAM provides the only access by remote sensing to altitudes of 80–150 km, the region used for aerocapture and aerobraking. As predicted (Bertaux et al., 2004), stellar occultations gave a unique chance to detect clouds on the nightside, with the discovery of CO_2 condensation clouds at 90 km.

— Remote sensing of the ionosphere from natural emissions and interaction with the solar wind is not included in other ongoing or planned missions.

— The mapping of H_2O by the AOTF near-IR spectrometer has been fully demonstrated. With a mass of only 0.75 kg, this instrument should fly as a low-cost passenger on all future Mars missions.

SPICAM is applying to Mars the most successful methods for studying Earth's atmosphere: backscatter UV and IR spectroscopy, and solar/stellar occultation limb sounding. The most remarkable thing is that all these results have been obtained with an instrument weighing only 4.7 kg. It is fair to say that the success of SPICAM is also due to the design of the Mars Express spacecraft, which has a marvellous capability for orientation in any direction, at almost any time.

It is already clear that the atmosphere of Mars, as well as that of Earth, experiences a strong inter-annual variability and its study must be pursued at every opportunity. The approved extension of the Mars Express mission for a full second Mars year is an excellent decision; it is hoped that further extensions will be possible.

Acknowledgements

The authors express their gratitude to all ESA members who participated in the successful Mars Express mission, in particular M. Denis and his team at ESOC for their delicate control of the spacecraft, and R. Pischel and T. Zeghers at ESTEC for careful planning exercises. They also thank Astrium for the design and construction of the spacecraft, and in particular A. Clochet, responsible for the scientific payload. They thank collaborators at the three institutes for the design and fabrication of the instrument (Service d'Aéronomie/France, BIRA/Belgium and IKI/Moscow). They thank CNRS and CNES for financing SPICAM in France, the Belgian government, and NASA for supporting US co-investigators. The Russian team acknowledges support of RFFI grant 04-02-16856-a. The authors express their gratitude to F. Rocard at CNES and are grateful to M.D. Smith for the TES water vapour profiles. They are grateful to E. Villard for special measurements on the second Flight Model of SPICAM, while preparing SPICAV for Venus Express. They also have a special thought for V.I. Moroz, a co-investigator, who promoted planetary exploration so much in the Soviet Union/Russia, and who passed away in 2004.

References

Acuña, M.H., Connerney, J.E.P., Wasilewski, P., Lin, R.P., Mitchell, D., Anderson, K.A., Carlson, C.W., McFadden, J., Rème, H., Mazelle, C., Vignes, D., Bauer, S.J., Cloutier, P. & Ness, N.F. (2001). Magnetic Field of Mars: Summary of Results from the Aerobraking and Mapping Orbits, *J. Geophys. Res.* **106**, 23,403–23,417.

Anderson, D.E. & C.W. Hord (1972). Mariner 6 and 7 Ultraviolet Spectrometer Experiment: Analysis of Hydrogen Lyman-Alpha Data. *J. Geophys. Res.* **76**, 6666–6673.

Angelats i Coll, M., F. Forget, M.A. Lopez-Valverde & F. Gonzalez-Galindo (2005). The First Mars Thermospheric General Circulation Model: The Martian Atmosphere from the Ground to 240 km. *Geophys, Res. Letts.* **32**, L04201, doi:10.1029/2004GL021368.

Barth, C.A. & C.W. Hord (1971). Mariner Ultraviolet Spectrometer: Topography and Polar Cap. *Science* **173**, 197-201.

Barth, C.A, J.B. Pearce, K.K. Kelly, L. Wallace & W.G. Fastie. (1967). Ultraviolet Emissions Observed near Venus from Mariner. *Science* **158**, 1675-1678.

Barth, C.A., C.W. Hord, J.B. Pearce, K.K. Kelly, G.P. Anderson & A.I. Stewart (1971). Mariner 6 and 7 Ultraviolet Spectrometer Experiment: Upper Atmosphere Data. *J. Geophys. Res.* **76**, 2213-2227.

Barth, C.A., A.I. Stewart, C.W. Hord & A.L. Lane (1972). Mariner 9 Ultraviolet Spectrometer Experiment: Mars Airglow Spectroscopy and Variations in Lyman Alpha. *Icarus* **17**, 457-462.

Barth, C.A., C.W. Hord, A.I. Stewart, A.L. Lane, M.L. Duck & G.P. Anderson (1973). Mariner 9 Ultraviolet Spectrometer Experiment: Seasonal Variation of Ozone on Mars. *Science* **179**, 795-796.

Barth, C.A., A.I.F. Stewart, S.W. Bougher, D.M. Hunten, S.J. Bauer & A.F. Nagy (1992). Aeronomy of the Current Martian Atmosphere. In *Mars* (Eds. Kieffer et al.), Univ. of Arizona Press, USA.

Bertaux, J.L., D. Fonteyn, O. Korablev, E. Chassefière, E. Dimarellis, J.P. Dubois, A. Hauchecorne, M. Cabane, P. Ranou, A.C. Levasseur-Regourd, G. Cernogora, E. Quemerais, C. Hermans, G. Kockarts, C. Lippens, M. De Maziere, D. Moreau, C. Muller, E. Neefs, P.C. Simon, F. Forget, F. Hourdin, O. Talagrand, V.I. Moroz, A. Rodin, B. Sandel & A. Stern (2000). The Study of the Martian Atmosphere from Top to Bottom with SPICAM Light on Mars Express. *Planet. Space Sci.* **48**, 1303-1320.

Bertaux, J.L., D. Fonteyn, O. Korablev, E. Chassefiere, E. Dimarellis, J.P. Dubois, A. Hauchecorne, M. Cabane, P. Rannou, A.C. Levasseur-Regourd, G. Cernogora, E. Quemerais, C. Hermans, G. Kockarts, C. Lippens, M. De Maziere, D.Moreau, C. Muller, E. Neefs, P. Simon, F. Forget, F. Hourdin, O. Talagrand, V.I. Moroz, S. Rodin, B. Sandel & A. Stern (2004). SPICAM: Studying the Global Structure and Composition of the Martian Atmosphere. In *Mars Express: The Scientific Payload* (Ed. A. Wilson), SP-1240, ESA Publications Division, ESTEC, Noordwijk, The Netherlands, pp.95-120.

Bertaux, J.-L., F. Leblanc, S. Perrier, E. Quemerais, O. Korablev, E. Dimarellis, A. Reberac, F. Forget, P.C. Simon, A.S. Stern & B. Sandel. (2005a). First Observation of Nightglow in the Upper Atmosphere of Mars: the NO Bands in UV and Implications for Atmospheric Transport. *Science* **307**, 566-569.

Bertaux, J.-L., F. Leblanc, O. Witasse, E. Quémerais, J. Lilensten, A.S. Stern, B. Sandel & O. Korablev (2005b). Discovery of Aurora on Mars. *Nature* **435**, 790-794.

Bertaux, J-L., Korablev, O., Perrier, S., Quémerais, E., Montmessin, F., Leblanc, F., Lebonnois, S., Rannou, P., Lefèvre, F., Forget, F., Fedorova, A., Dimarellis, E., Reberac, A., Fonteyn, D., Chaufray, J-Y. & Guibert, S. (2006). SPICAM on Mars Express: Observing Modes and Overview of UV Spectrometer Data and Scientific Results. *J. Geophys. Res.* **111**, E10S90, doi: 10.1029/2006JE002690

Bibring, J.P., Langevin, Y., Poulet, F., Gendrin, A., Gondet, B., Berthé, M., Soufflot, A., Drossart, P., Combes, M., Bellucci, G., Moroz, V.I., Mangold, N., Schmitt, B. and the OMEGA team (2004). Perennial Water Ice Identified in the South Polar Cap of Mars. *Nature* **428**, 627-630.

Blamont, J.E. & E. Chassefière (1993). First Detection of Ozone in the Middle Atmosphere of Mars from Solar Occultation Measurements. *Icarus* **104**, 324-336.

Blamont, J.E., E. Chassefière, J.P. Goutail, B. Mege, M. Nunes-Pinharanda, G. Soushon, V.A. Krasnopolsky, A.A. Krysko & V.I. Moroz (1989). Vertical Structure of Dust and Ozone in the Martian Atmosphere Deduced from Solar Occultation Measurements. *Nature* **341**, 600-603.

Bougher, S.W., D.P. Hinson, J.M. Forbes & S. Engel (2001). MGS Radio Science Electron Density Profiles and Implications for the Neutral Atmosphere. *Geophys. Res. Lett.* **28**, 3091-3094.

Bougher, S.W., S. Engel, R.G. Roble & B. Foster. (2000). Comparative Terrestrial Planet Thermospheres: 3. Solar Cycle Variation of Global Structure and Winds at Solstices. *J. Geophys. Res.* **105**, 17,669-17,689.

Bougher, S.W., Roble, R.G., Ridley, E.C. & Dickinson, R.E. (1990). The Mars Thermosphere. II. General Circulation with Coupled Dynamics and Composition. *J. Geophys. Res.* **95**, 14,811-14,827.

Bougher, S.W., S. Engel, D.P. Hinson & J.R. Murphy (2004). MGS Radio Science Electron Density Profiles: Interannual Variability and Implications for the Martian Neutral Atmosphere. *J. Geophys. Res.* **109**, E03010, doi:10.1029/2003JE002154.

Chassefière, E., J.E. Blamont, V.A. Krasnopolsky, O.I. Korablev, S.K. Atreya & R.A. West (1992). Vertical Structure and Size Distributions of Martian Aerosols from Solar Occultation Measurements. *Icarus* **97**, 46-69.

Chaufray, J.-Y., Modolo, R., Leblanc, F. & G. Chanteur (2005). Non Thermal Oxygen Escape at Mars at Low and High Solar Activities. Presented at IAGA poster session.

Clancy, R.T., A.W. Grossman, M.J. Wolff, P.B. James, D.J. Rudy, Y.N. Billawala, B.J. Sandor, S.W. Lee & D.O. Muhleman (1996). Water Vapor Saturation at Low Altitudes around Mars Aphelion: A Key to Mars Climate? *Icarus* **122**, 36-62.

Conrath, B.J., J.C. Pearl, M.D. Smith & P.R. Christensen (1998). MGS TES Results: Characterization of the Martian Atmospheric Thermal Structure. DPS Meeting 30, #11.P06. *Bull. Am. Astron. Soc.* **30**, 1031.

Conrath, B. J., J.C. Pearl, M.D. Smith, P.R. Christensen, 1999. Mars Global Surveyor TES Results: Atmospheric Thermal Structure Retrieved from Limb Measurements DPS Meeting 31, #49.08

Conway, R.R. (1981). Spectroscopy of the Cameron Bands in the Mars Airglow. *J. Geophys. Res.* **86**, 4767-4775.

ESA (2001). GOMOS: An Instrument for Global Atmospheric Ozone Monitoring. ESA SP-1244, pp113.

Farmer, C.B. & D.D. LaPorte (1972). The Detection and Mapping of Water Vapor in the Martian Atmosphere. *Icarus* **16**, 34-46.

Fedorova, A.A., A.V. Rodin & I.V. Baklanova (2004). MAWD Observations Revisited: Seasonal Behavior of Water Vapor in the Martian Atmosphere. *Icarus* **171**, 54-67.

Fedorova, A., Korablev, O., Bertaux, J.-L., Rodin, A., Kiselev, A. & Perrier, S. (2006a). Mars Water Vapor Abundance from SPICAM IR Spectrometer: Seasonal and Geographic Distributions. *J. Geophys. Res.* **111**, E09S08, doi:10.1029/2006 JE002695

Fedorova, A., Korablev, O., Perrier, S., Bertaux, J.L., Lefevre, F., Rodin, A. (2006b). Observation of O2 1.27 μm Dayglow by SPICAM IR: Seasonal Distribution for the First Martian Year of Mars-Express. *J. Geophys. Rev.* **111**, E09S07, DOI: 10.1029/2006JE002694

Fedorova, A., Korablev, O.I., Bertaux, J-L., Rodin, A.V., Montmessin, F., Belyaev, D.A. & Reberac, A. (2008). Solar Infrared Occultations by SPICAM Experiment on Mars-Express: Simultaneous Observations of H_2O, CO_2 and Aerosol Vertical Distribution. Submitted to *Icarus*.

Feldman, P.D., Moos, H.W., Clarke, J.T. & Lane, L. (1979). Identification of the UV Nightglow from Venus. *Nature* **279**, 221-222.

Feldman, P.D., E.B. Burgh, S.T. Durrance & A.F. Davidsen (2000). Far-Ultraviolet Spectroscopy of Venus and Mars at 4A Resolution with the Hopkins Ultraviolet Telescope on Astro-2. *Astrophys. J.* **538**, 395-400.

Fiorenza, C. & V. Formisano (2005). A Solar Spectrum for PFS Data Analysis. *Planet. Space Sci.* **53**, 1009-1016.

Forbes, J.M., A.F.C. Bridger, M.E. Hagan, S.W. Bougher, J.L. Hollingsworth, G.M. Keating & J.R. Murphy (2002). Nonmigrating Tides in the Thermosphere of Mars. *J. Geophys. Res.* **107** (E11), 5113, doi: 10.1029/2001JE001582.

Forget, F., F. Hourdin, R. Fournier, C. Hourdin, O. Talagrand, M. Collins, S.R. Lewis, P.L. Read & J.-P. Huot (1999). Improved General Circulation Models of the Martian Atmosphere from the Surface to above 80 km. *J. Geophys. Res.* **104**(E10), 24,155-24,176.

Forget, F., F. Hourdin, and O. Talagrand, 1996, Simulation of the martian atmospheric polar warming with the LMD general circulation model, *Ann. Geophys.* **14**, C797.

Forget F., Gonzalez-Galindo, F., Lebonnois, S., Quémerais, E., Bertaux, J.L., Montmessin, F., Reberac, A., Dimarellis, E. & Lopez Valverde, M.A. (2008). The Density and Temperatures

of the Upper Martian Atmosphere Measured by Stellar Occultations with Mars Express SPICAM. *JGR Planets*, in Press.

Fox, J.L. & A. Dalgarno (1979). Ionization, Luminosity, and Heating of the Upper Atmosphere of Mars. *J. Geophys. Res.* **84**, 7315-7333.

Fox, J.L. (1986). Models for Aurora and Airglow Emissions from other Planetary Atmospheres. *Can. J. Phys.* **64**, 1631-1656.

Glenar, D.A., J.J. Hillman, B. Saiff & J. Bergstralh (1994). Acouto-optic Imaging Spectropolarimery for Remote Sensing. *Appl. Opt.* **33**, 7412-7424.

Gutchek, R.A. & E.C. Zipf (1973). Excitation of the CO Fourth Positive System by the Dissociative Recombination of CO_2^+ Ions. *J. Geophys. Res.* **78**, 5429-5436.

Haider, S.A., J. Kim, A.F. Nagy, C.N. Keller, M.I. Verigin, K.I. Gringauz, N.M. Shutte, K. Szego & P. Kiraly (1992). Calculated Ionization Rates, Ion Densities, and Airglow Emission Rates due to Precipitating Electrons in the Nightside Ionosphere of Mars. *J. Geophys. Res.* **97**, 10,637-10,641.

Hapke, B. (1981). Bidirectional Reflectance Spectroscopy. I. Theory. *J. Geophys. Res.* **86**, 3039-3054.

Hauchecorne, A., Bertaux, J.-L., Dalaudier, F., Cot, C., Lebrun, J.-C., Bekki, S., Marchand, M., Kyrölä, E., Tamminen, J., Sofieva, V., Fussen, D., Vanhellemont, F., Fanton d'Andon, O., Barrot, G., Mangin, A., Théodore, B., Guirlet, M., Snoeij, P., Koopman, R., Saavedra de Miguel, L., Fraisse, R. & Renard, J.-B. (2005). First Simultaneous Global Measurements of Nighttime Stratospheric NO_2 and NO_3 Observed by Global Ozone Monitoring by Occultation of Stars (GOMOS)/Envisat in 2003. *J. Geophys. Res.* **110**, No. D18, D18301, doi: 10.1029/2004JD005711

Hinson, D.P., R.A. Simpson, J.D. Twicken, G.L. Tyler & F.M. Flasar (1999). Initial Results from Radio Occultation Measurements from Mars Global Surveyor. *J. Geophys. Res.* **104**(E11), 26997-27012.

Keating, G.M., S.W. Bougher, R.W. Zurek, Tolson, R.H., Cancro, G.J., Noll, S.N., Parker, J.S., Schellenberg, T.J., Shane, R.W., Wilkerson, B.L., Murphy, J.R., Hollingsworth, J.L., Haberle, R.M., Joshi, M., Pearl, J.C., Conrath, B.J., Smith, M.D., Clancy, R.T., Blanchard, R.C., Wilmoth, R.G., Rault, D.F., Martin, T.Z., Lyons, D.T., Esposito, P.B., Johnston, M.D., Whetzel, C.W., Justus, C.G. & Babicke, J.M. (1998). The Structure of the Upper Atmosphere of Mars: In Situ Accelerometer Measurements from Mars Global Surveyor. *Science* **279**, 1672-1676.

Keating G.M., M. Theriot, R. Tolson, S. Bougher, F. Forget & J. Forbes (2003). Global Measurement of the Mars Upper Atmosphere: In-situ Accelerometer Measurements from Mars Odyssey 2001 and Mars Global Surveyor. In *Lunar and Planetary Science*, 34th Ann. Lun. Planet. Sci.Conf., 17-21 March 2003, League City, Texas, USA, abstract no.1142.

Kerzhanovich, V. V. (1977). Mars 6: Improved Analysis of the Descent Module Measurements. *Icarus* **30**, 1-25.

Korablev, O.I., V.A. Krasnopolsky, A.V. Rodin & E. Chassefière (1993). Vertical Structure of Martian Dust Measured by the Solar Occultation from Phobos Spacecraft. *Icarus* **102**, 76-87.

Korablev, O., Bertaux, J-L., A. Grigoriev, E. Dimarellis, Yu. Kalinnikov, A. Rodin, C. Muller & D.Fonteyn (2002a). An AOTF-Based Spectrometer For the Studies of Mars Atmosphere for Mars Express Mission. *Adv. Space Res.* **29**(2), 143-150,

Korablev, O.I., J.L. Bertaux, E. Dimarellis, A. Grigoriev, Yu. Kalinnikov, A. Stepanov, & S. Guibert (2002b). AOTF-based Spectrometer for Mars Atmosphere Sounding. In *Infrared Spaceborne Remote Sensing X. Proc. SPIE* **4818** (Eds. M. Strojnik & B.F. Andresen), SPIE, 261-271.

Korablev, O.I., Bertaux, J.L., & Dubois, J.P. (2001). Occultation of Stars in the UV: Study of the Atmosphere of Mars. *JGR Planets* **106**, 7597-7610.

Korablev, O., Bertaux, J-L., Fedorova, A., Fonteyn, D., Stepanov, A., Kalinnikov, Y., Kiselev, A., Grigoriev, A., Jegoulev, V., Perrier, S., Dimarellis, E., Dubois, J.P., Reberac, A., Van Ransbeeck, E., Gondet, B., Montmessin, F. & Rodin, A. (2006). SPICAM IR Acousto-optic Spectrometer Experiment on Mars Express. *J. Geophys. Res.* **111**, E9, E09S03, doi: 10.1029/2006JE002696

Krasnopolsky, V.A. (1997). Photochemical Mapping of Mars. *J. Geophys. Res.* **102**, 13,313-13,320.

Krasnopolsky, V.A. & G.L. Bjoracker (2000). Mapping of Mars $O_2(^1\Delta)$ Dayglow. *J. Geophys. Res.* **105**, 20,179-20,188.

Krasnopolsky, V.A. & P.D. Feldman (2001). Detection of Molecular Hydrogen in the Atmosphere of Mars. *Science* **294**, 1914-1917.

Krasnopolsky, V.A. & Feldman, P.D. (2002). Far Ultraviolet Spectrum of Mars. *Icarus* **160**, 86-94.

Krasnopolsky, V.A., O.I. Korablev, V.I. Moroz, A.A. Krysko, J.E. Blamont & E. Chassefiere (1991). Infrared Solar Occultation Sounding of the Martian Atmosphere by the Phobos Spacecraft. *Icarus* **94**, 32-44.

Krasnopolsky, V. A., S. Bowyer, S. Chakrabarti, G.R. Gladstone & J.S. McDonald (1994). First Measurement of Helium on Mars: Implications for the Problem of Radiogenic Gases on the Terrestrial Planets. *Icarus* **109**, 337-351.

Krasnopolsky, V.A., M.J. Mumma & G.R. Gladstone (1998). Detection of Atomic Deuterium in the Upper Atmosphere of Mars. *Science* **280**, 1576-1580.

Krasnopolsky, V.A., V.I. Moroz, A.A. Krysko, O.I. Korablev, V.S. Zhegulev, A.V. Grigoriev, A.Yu. Tkachuk, V.A. Parshev, J.E. Blamont & J.-P. Goutail (1989). Phobos-2: Solar Occultation Spectroscopic Measurements of the Martian Atmosphere at 1.9 and 3.7 μm. *Nature* **341**, 603-604.

Kurucz, R. (1995). The Solar Spectrum: Atlases and Line Identifications. In *Workshop on Laboratory and Astronomical High resolution Spectra, Proc. ASP Conf., Brussels, Belgium, 29 August-2 September 1994* (Eds. A.J. Saival, R. Blomme & N. Grevesse), San Francisco, ASP, **81**, p.17-51.

Leblanc, F. & R.E. Johnson (2001). Sputtering of the Martian Atmosphere by Solar Wind Pick-up Ions. *Planet. Space Sci.* **49**, 645-656.

Leblanc F., Chaufray, J.Y., Lilensten, J., Witasse, O. & Bertaux, J.-L. (2006). Martian Dayglow as Seen by the SPICAM UV Spectrograph on Mars Express. *J. Geophys. Res.* **111**, E09S11, doi: 10.1029/2005JE002664

Lebonnois, S., Quémerais, E., Montmessin, F., Lefèvre, F., Perrier, S., Bertaux, J.-L. & Forget, F. (2006), Vertical Distribution of Ozone on Mars as Measured by SPICAM/Mars Express using Stellar Occultations. *J. Geophys. Res.* **111**, E09S05, doi:10.1029/2005JE002643

Lefèvre, F., S. Lebonnois, F. Montmessin & F. Forget (2004). Three-dimensional Modelling of Ozone on Mars. *J. Geophys. Res.* **109**, E07004, doi:10.1029/2004 JE002268

Lefèvre, F., Jean-Loup Bertaux, J.L., Clancy, R.T., Encrenaz, T., Fast, K., Forget, F., Lebonnois, S., Montmessin, F. & Perrier, S. (2008). Heterogeneous Chemistry in the Atmosphere of Mars. *Nature*, in press.

Magalhães, J.A., J.T. Schofield & A. Seiff (1999). Results of the Mars Pathfinder Atmospheric Structure Investigation. *J. Geophys. Res.* **104**, 8943-8955.

Montmessin, F., Bertaux, J.L., Quémerais, E., Korablev, O., Rannou, P., Forget, F., Perrier, S., Fussen, D., Lebonnois, S., Reberac, A. & Dimarellis, E. (2006a). Sub-visible CO_2 Ice Clouds Detected in the Mesosphere of Mars. *Icarus* **183**(2), 403-410.

Montmessin, F., Quémerais, E., Bertaux, J.L., Korablev, O., Rannou, P. & Lebonnois, S. (2006b). Stellar Occultations at UV Wavelengths by the SPICAM Instrument: Retrieval and Analysis of Martian Haze Profiles. *J. Geophys. Res.* **111**, E09S09, doi:10.1029/2005JE002662

Montmessin, F., F. Forget, P. Rannou, M. Cabane & R.M. Haberle (2004). Origin and Role of Water Ice Clouds in the Martian Water Cycle as Inferred from a General Circulation Model. *J. Geophys. Res*. **109**, E10004, DOI: 10.1029/2004JE002284.

Nier, A.O. & M.B. McElroy (1977). Composition and Structure of Mars' Upper Atmosphere: Results from the Neutral Mass Spectrometers on Viking 1 and 2. *J. Geophys. Res.* **82**(28), 4341-4349.

Noxon, J.F., W.A. Traub, N.P. Carleton & P. Connes (1976). Detection of O_2 Airglow Emission from Mars and the Martian Ozone Abundance. *Astrophys. J.* **207**, 1025-1035.

Perrier, S., Bertaux, J.L., Lefèvre, F., Lebonnois, S., Korablev, O., Fedorova, A. & Montmessin, F. (2006). Global Distribution of Total Ozone on Mars from SPICAM/MEX UV Measurements. *J. Geophys. Res.* **111**, E09S06, doi: 10.1029/2006JE002681

Quémerais, E., Bertaux, J.L., Korablev, O., Dimarellis, E., Cot, C., Sandel, B.R., & Fussen, D. (2006). Stellar Occultations Observed by SPICAM on Mars Express. *J. Geophys. Rev.* **111**, E09S04, doi :10.1029/2005JE002604

Quémerais, E. & Bertaux, J.L. (2002). Radiometric Calibration of the SWAN Instrument. In *ISSI Scientific Report SR-002*, The Radiometric Calibration of SOHO (Eds. A. Pauluhn, M.C.E. Huber & R. von Steiger), pp.203-210.

Rannou, P., Perrier, S., Bertaux, J.-L., Montmessin, F., Korablev, O. & Rébérac, A. (2006). Dust and Cloud Detection at Mars Limb from UV Scattered Sunlight with SPICAM. *J. Geophys. Res.* **111**, E09S10, doi: 10.1029/2006JE002693

Richardson, M.I. & R.J. Wilson (2002). Investigation of the Nature and Stability of the Martian Seasonal Water Cycle with a General Circulation Model. *J. Geophys. Res.* **107**, 10.1029/2001JE001536.

Rodin, A.V., O.I. Korablev & V.I. Moroz (1997). Vertical Distribution of Water in Near-Equatorial Troposphere of Mars: Water Vapor and Clouds. *Icarus* **125**, 21-29.

Rodin, A.V., R.T. Clancy, R.J. Wilson, M. Richardson, M. Wolff & S. Woods (1999). Thermal Feedback between Dust and Water Ice Clouds in Mars Atmosphere: Implications for the Aphelion Climate. *Icarus*; in press.

Roscoe, H.K., R.A. Freshwater, R. Wolfenden, R.L. Jones, D.J. Fish, J.E. Harries & D.J. Oldham (1994). Using Stars for Remote Sensing of the Earth's Stratosphere. *Appl. Optics.* **33**, 7126-7131.

Rothman, L.S., Barbe, A., Benner, D., Brown, L.R., Camy-Peyret, C., Carleer, M.R., Chance, K., Clerbaux, C., Dana, V., Devi, V.M., Fayt, A., Flaud, J.-M., Gamache, R.R., Goldman, A., Jacquemart, D., Jucks, K.W., Lafferty, W.J., Mandin, J.-Y., Massie, S.T., Nemtchinov, V., Newnham, D.A., Perrin, A., Rinsland, C.P., Schroeder, J., Smith, K.M., Smith, M.A.H., Tang, K., Toth, R.A., Vander Auwera, J., Varanasi, P. & Yoshino, K. (2003). The Hitran Molecular Spectroscopic Database: Edition of 2000 including through 2001. *J. Quant. Spectrosc. Rad. Transfer* **82**, 5-44.

Sandel, B.R. & A.L. Broadfoot (1986). Statistical Performance of the Intensified Charge Coupled Device. *Appl. Optics* **25**, 4135-4140.

Santer, R., M. Deschamps, L.V. Ksanfomaliti & A. Dollfus (1985.) Photopolarimetric Analysis of the Martian Atmosphere by the Soviet MARS-5 Orbiter. I: White Clouds and Dust Veils. *Astron. Astroph.* **150**(2), 217-228.

Schofield, J.T., J.R. Barnes, D. Crisp, R.M. Haberle, S. Larsen, J.A. Magalhães, J.R. Murphy, A. Seiff & G. Wilson (1977). The Mars Pathfinder Atmospheric Structure Investigation/ Meteorology (ASI/MET) Experiment. *Science* **278**, 1752-1758.

Seiff, A. & D.B. Kirk (1977). Structure of the Atmosphere of Mars in Summer in Mid-latitudes. *J. Geophys. Res.* **82**, 4364-4378.

Smith, M.D. (2004). Interannual Variability in TES Atmospheric Observations of Mars during 1999-2003. *Icarus* **167**, 148-165.

Smith, G.R. & D.M. Hunten (1990). Study of Planetary Atmospheres by Absorptive Occultations. *Rev. Geophys.* **28**, 117-143.

Smith, D.E., M.T. Zuber, H.V. Frey, J.B. Garvin, J.W. Head, D.O. Muhleman, G.H. Pettengill, R.J. Phillips, S.C. Solomon, H.J. Zwally, W.B. Banerdt, T.C. Duxbury, M.P. Golombek, F.G. Lemoine, G.A. Neumann, D.D. Rowlands, O. Aharonson, P.G. Ford, A.B. Ivanov, P.J. McGovern, J.B.Abshire, R.S. Afzal, & X. Sun (2001). Mars Orbiter Laser Altimeter (MOLA): Experiment Summary after the First Year of Global Mapping of Mars. *J. Geophys. Res.* **106**, 23,689-23,722.

Smith, M.D., J.C. Conrath, J. Barney & P.R. Christensen (2001). Thermal Emission Spectrometer Results: Mars Atmospheric Thermal Structure and Aerosol Distribution. *J. Geophys. Res.* **106**, 23929-23945.

Stewart, A.I. (1972). Mariner 6 and 7 Ultraviolet Spectrometer Experiment: Implication of CO_2^+, CO and O airglow. *J. Geophys. Res.* **77**, 54-68.

Stewart, A.I.F. & C.A. Barth (1979). Ultraviolet Night Airglow of Venus. *Science* **205**, 59-62.

Stewart, A.I.F, C.A. Barth, C.W. Hord & A.L. Lane (1972). Mariner 9 Ultraviolet Spectrometer Experiment: Structure of Mars' Upper Atmosphere. *Icarus* **17**, 469-474.

Stewart, A.I.F., D.E. Anderson, Jr., L.W. Esposito & C.A. Barth (1979). Ultraviolet Spectroscopy of Venus: Initial Results from the Pioneer Venus Orbiter. *Science* **203**, 777-779.

Strickland, D.J., G.E. Thomas & P.R. Sparks (1972). Mariner 6 and 7 Ultraviolet Spectrometer Experiment: Analysis of the OI 1304-1356-A Emissions. *J. Geophys. Res.* **77**, 4052-4068.

Traub, W.A, N.P. Carleton, P. Connes & J.F. Noxon (1979). The Latitude Variation of O_2 Airglow and O_3 Abundance on Mars. *Astrophys. J.* **229**, 846-850.

Wang, J.-S. & E. Nielsen (2004).Evidence for Topographic Effects on the Martian Ionosphere. *Planet. Space Sci.* **52**, 881-886.

Wilson, R.J. (1997). A General Circulation Model Simulation of the Mars Polar Warming. *Geophys. Res. Lett.* **24**, 123-126.

Witasse, O. (2000). Modélisation des ionospheres planétaires et de leur rayonnement: la Terre et Mars. PhD Thesis, Université Joseph Fourier, July 2000.

Withers, P., S.W. Bougher & G.M. Keating (2004). The Effects of Topographically-Controlled Thermal Tides in the Martian Upper Atmosphere as Seen by the MGS Accelerometer. *Icarus* **164**, 14-32.

Wuttke, M.W., H.U. Keller, W.J. Markiewicz, E. Petrova, K. Richter & N. Thomas (1997). Properties of Dust in the Mars Atmosphere: A Revised Analysis of Phobos/KRFM Data. *Planet. Space Sci.* **45**, 281-288.